Fall 11-17-2020

ATOM TRAPPING AND ITS ROLE ON THE NUCLEATION & GROWTH OF PLATINUM NANOPARTICLES

Deepak Kunwar

Deepak Kunwar

Candidate

Department of Chemistry and Chemical Biology

Department

This dissertation is approved, and it is acceptable in quality and form for publication:

Approved by the Dissertation Committee:

Abhaya K. Datye, Chairperson

Hua Guo

Adrian Brearley

Eric J. Peterson

ATOM TRAPPING AND ITS ROLE ON THE NUCLEATION & GROWTH OF PLATINUM NANOPARTICLES

by

DEEPAK KUNWAR

B.Sc. Chemistry, Tribhuvan University, Nepal (2003)
M.Sc., Organic Chemistry, Tribhuvan University, Nepal (2005)

DISSERTATION

Submitted in Partial Fulfillment of the
Requirements for the Degree of

Doctor of Philosophy
Chemistry

The University of New Mexico
Albuquerque, New Mexico

December 2020

DEDICATION

To my beloved parents, Pana Devi Kunwar and Tul Bahadur Kunwar who believed throughout their life education is the ray of hope that leads from dark life to a bright future. I would also like to dedicate this work to my better half Nilam Adhikari Kunwar, sons Devansh and Devesh Kunwar, and brothers Bharat and Nirajan Kunwar for their support, encouragement, and sacrifice during this Journey. This journey wouldn't be possible without their sacrifice, unconditional love, and care. Love from me to you all so much.

Deepak

ACKNOWLEDGEMENTS

My sincere gratitude goes to my Ph.D. advisor Prof. Abhaya Datye for his advice, support, guidance, and patience throughout my graduate student life at the University of New Mexico. It has been a remarkably wonderful as well as fruitful journey with him. I feel truly blessed and grateful for having him as my Ph.D. advisor and will remain obliged to him throughout my life for enlightening me with research knowledge. I am thankful for the challenges and opportunities he provided to me during this adventurous journey. I have learned directly and indirectly so many research skills such as making presentations, delivering efficient talks, garnering useful data, putting them in a coherent, logical as well as harmonic order, and most importantly building the stories out from the data. I have not only learned the research knowledge in my formal education but also helped prepare me to tackle the different problems and situations in the course of life span. I shall always remain obliged and indebted to my guru Prof. Datye for his passion and mentoring skill, no matter how many times I repeated the same mistakes.

I would like to thank Dr. Eric Peterson, Dr. Ying Bing, and Michel Splide for helping me to learn XRD, TEM, and SEM respectively. I would like to thank Rik ter Veen and Hidde H. Brongersma for their help in Low Energy Ion Scattering. I am thankful to Hiroki Hashiguchi and Libor Kovarik for their help in AC-STEM imaging. I would also like to thank Xavier Isidro Pereira-Hernández and Stephen C. Purdy for helping me in the DRIFTS and XAS experimentation and analysis, respectively. Similarly, I am thankful to Shulan Zhou and Sen Lin for their help in the DFT part. I would also like to thank Hien Pham, Haifeng Xiong, and Andrew DeLaRiva for their help and involvement in the projects. My special thanks go to Prof. Hua Guo for serving as a Ph.D. committee

member, contributing theoretically to my research, and guiding me during this journey no less than as an advisor. I am also thankful to Prof. Adrian Brearley and Dr. Eric Peterson for being part of my Ph.D. committee. I would like to thank the AFOSR Grant 740821, the US Department of Energy (DOE) grant DE-FG02-05ER15712, US National Science Foundation grants EEC- 1647722 (CISTAR) and NSF GOALI Grant CBET-1438765 for funding my Ph.D. research. My thanks also go to General Motors Company for the internship opportunity at Warren, Michigan with catalysts and after-treatment group while I was being funded by the NSF GOALI Grant. I would like to thank Prof. Datye and Dr. Qi for this wonderful opportunity.

ATOM TRAPPING AND ITS ROLE ON THE NUCLEATION & GROWTH OF PLATINUM NANOPARTICLES

By

Deepak Kunwar

B.SC. Chemistry, Tribhuvan University, Nepal (2003)

M.SC., Tribhuvan University, Nepal (2005)

Ph.D. The University of New Mexico, USA (2020)

ABSTRACT

Diesel oxidation catalysts deactivate due to Pt sintering, a major problem in automotive industries. To make sure they operate effectively throughout the lifetime of the vehicle, automotive industries are putting an excessive amount of Pt. There is a need to develop a catalyst that serves long term performance with minimal use of Pt. Jones et al[.1] demonstrated that ceria traps Pt atoms. His work generated some logical and valid questions such as what is the mechanism for the formation of anomalously large Pt particles? What is the upper limit of Pt metal loading in the form of single atoms in ceria? What are the sites responsible for the atom trapping? Where does the Pt atom locate: the surface or subsurface of the ceria? Does a non-reducible oxide support trap Pt atom? Is it possible to modify the nucleation of Pt using atom trapped ceria as support? The fundamental understanding of these questions was the focus of this dissertation.

Energy Dispersive X-ray Spectroscopy (EDX) was used for the quantification of Pt. Multiple characterization techniques such as X-ray Diffraction (XRD), Low Energy Ion Scattering (LEIS), X-ray Photoelectron Spectroscopy (XPS), Diffuse Reflectance

Infrared Fourier Transmission Spectroscopy (DRIFTS), Aberration Corrected Scanning Transmission Electron Microscopy (AC-STEM), X-ray Absorption Spectroscopy (XAS), CO oxidation reactivity, and Density functional theory (DFT) were used to understand the state and nature of the Pt species.

The experimental evidence suggests Pt particle grow anomalously large due to vapor phase assisted catalyst sintering when subjected to accelerated aging. Ceria can trap 3wt% Pt metal in the form of single atoms which corresponds to 1atom/nm2. The trapped single-atom Pt binds to the ceria (111) step edges strongly and prevents its emission to the vapor phase. Spinel (MgAl2O4) can stabilize Pt atoms with the aid of K additive. By anchoring Pt ions on the catalyst support, the morphology of the deposited phase can be modified causing the formation of 2-D rafts instead of 3-D metal nanoparticles.

In conclusion, trapping of mobile species (PtO2) into ceria support via high-temperature vapor-phase synthesis restricts the anomalous growth of Pt, slows down the emission of Pt from the catalyst system, and allows 100% atom efficiency. Strongly bounded Pt atoms on ceria modify the morphology of the deposited phase to 2-D rafts.

Table of contents

CHAPTER 1: INTRODUCTION

1.1 Statement of the Research Problem

Platinum is an active component used for diesel oxidation catalysts, but it sinters readily at elevated temperature (800 ˚C), recommended by USDRIVE Low-Temperature after treatment (LTAT) test protocol.[2] Platinum reacts with oxygen at 800 ˚C under oxidizing conditions to form a volatile PtO_2 species which has vapor pressure 1.6×10^{-8} atm in equilibrium with Pt metal.[3] Therefore, the transport of Pt through the vapor phase is significant at this temperature for making tremendously large Pt particles[4], leading to the loss of active surface area as well as catalytically active centers. However, there is no mechanism reported in the literature for the formation of these anomalously large Pt particles. It is extremely important to understand the causes for the formation of the large Pt particles in order to design the sinter resistant, durable, and efficient diesel oxidation catalysts. The fundamental understanding of some questions such as 1) Why and how Pt escapes from the catalyst system? 2) What mechanism is responsible for the formation of anomalously large Pt particles? 3) How can we able to retain the volatile species in the catalyst system in order to increase the lifetime of catalysts? help us to design the industrially applicable sinter resistance and durable catalysts. The focus of this dissertation will revolve around addressing these questions.

The replacement of platinum metal with other earth-abundant cheap metals is impossible for the abatement of exhaust emissions and many other chemical reactions because of its unique d orbitals, high Tamman temperature, and good oxidant properties. Hence the wise and efficient use of it helps to solve the current crisis facing by the automotive and chemical industries. Small Pt particles are active for the abatement of exhaust emissions

and many reactions. Only 33% of the metal particles are exposed to the reaction making the rest unavailable for the reactions. Previously, our group demonstrated[1] that Pt nanoparticles can be dispersed and trapped into ceria support in the form of single atoms. Alternatively, can be trapped in a PDO phase.[5] However, there were still questions left behind such as 1) What are the sites responsible for atom trapping on ceria? 2) How much Pt metal can be loaded in the form of single atoms? 3) Are there another oxide supports that can trap Pt atoms? 4) Is it possible to modify the nucleation of Pt using trapped atoms as a precursor?

The insight into the deactivation mechanism and other related concerns help to foster for the development of the sinter resistant durable diesel oxidation catalyst. The focus of this dissertation will be 1) unveiling the mechanism for the anomalous growth of Pt particles. 2) understanding the sites responsible for atom trapping on ceria. 3) Ameliorating the density of the single-atom per unit area of ceria support. 4) Preventing the emission of Pt into the vapor phase. 5) Searching for nonreducible support as an alternative of ceria for atom trapping. And 6) Controlling the nucleation of Pt through the trapped atom.

1.2 Catalysis

Catalyst is a chemical substance that accelerates the rate of reaction by lowering down the energy barrier. Catalysis is broadly classified into two branches homogeneous catalysis and heterogeneous catalysis. Each of these fields has its pros and cons. In this dissertation, the laser focus will be on heterogeneous catalysis.

1.2.1 Homogeneous Catalysis

In homogeneous catalysis, the reactant, catalyst, and the product are in the same phase. i.e. liquid. The biggest advantage of homogenous catalysis is that the reactant gets access to the catalytically active center from every possible direction. Moreover, the reactions occur at low temperature and atmospheric pressure. The biggest disadvantage is that product needs to be separated from the reactant and catalyst which takes a lot of time, energy, and effort making a product pure.

1.2.2 Heterogeneous Catalysis

In heterogeneous catalysis, the reactant and the product are in different phases than the catalyst. Reactants and products are either gaseous or liquids, but the catalyst is in a solid phase. The biggest advantage of heterogeneous catalysis is that being catalyst is in a solid phase so no need to put extra effort to separate it from the gaseous product. These catalysts can be operated at a wide range of operating conditions (i.e. high temperature and high pressure) and can be regenerated for multiple uses. These catalysts have high industrial relevance (i.e. more than 85% of all catalytically relevant chemical processes are heterogeneously catalyzed).

Table 1.1 A table showing the industrial catalysts that catalyze a variety of reactions

Catalysts	Reactions
Pt, Pd	Oxidation of CO & hydrocarbons (car exhaust)
Rh, Vanadium oxide	Reduction of NOx (in the exhaust)
Hydrogenation of vegetable oils	Ni

Acrylonitrile from propylene and ammonia	Bi-Mo, Fe-Sb (oxides)
Ammonia synthesis	Fe
Water-gas shift reaction	Fe (oxide), Cu-ZnO
Methanation	Ni
Polymerization of ethylene and propylene	Cr, TiClx/$MgCl_2$
Alkylation	H_2SO_4, HF, solid acids
Catalytic cracking of crude oil	Zeolites
Reforming of naphtha (to gasoline)	Pt, Pt-Re, Pt-Ir
Hydrotreating of crude oil	Co-Mo, Ni-Mo, Ni-W (sulfidic form)
Steam reforming of methane to $CO+H_2$	Ni

1.3 Dispersion and Sintering

The catalytically active center in heterogeneous catalysts is small nanoparticles typically in the order of 0.5-2 nm in size supported on reducible or non-reducible oxides. Usually their dispersion and surface to volume ratio are very high. Unfortunately, in a real working world, the catalyst is exposed to harsh conditions i.e. elevated temperature and oxidizing and reducing environments for a reaction to occur.

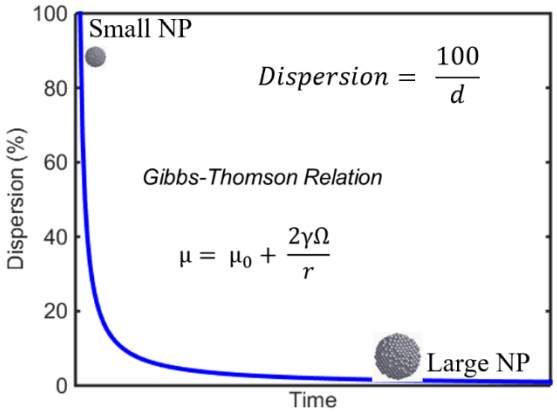

Figure 1.1 *Particle grows as a function of time*

These conditions are inclement for the catalyst. As a result, with operating time, these nanoparticles grow leading to the loss in dispersion and surface to volume ratio due to sintering. Sintering is a phenomenon in which large particles grow at the expense of smaller particles, attenuating in attendants, as a result, the catalytic activity plummets. The factor that governs the sintering is an interaction of catalytically active site to the support. If the interaction of these catalytically active center to the support is weak, then

the catalyst is more prone to sintering. On the flip side of the coin, if the interaction is strong enough, then the catalyst is less susceptible to sintering.[6] These phenomena go hand in hand. To the date, designing or engineering robust sinter resistant catalyst is the biggest challenge.

The process of sintering is mediated via Ostwald ripening in which the formation of the large particle is the reason for the disappearance of small particles. The small particles have high free energies that tend to aggregate into larger particles to reduce the free energy and to be in the thermodynamically stable form, especially at elevated temperature and reactive atmosphere. The sintering of supported nanoparticles is attributed to two transport mechanisms called particle migration and coalescence and Ostwald ripening.

Particle migration and coalescence involves the migration of small particles through the support at elevated temperature and collide with each other to form a large particle.[4] On the contrary, in Ostwald's ripening (OR) adatoms, migrate diffusing through the support or the vapor phase via molecular vapor species while the particle remains stationary.[7] We will discuss in detail about this in the later section of this dissertation where we will show our evidence that the dominant mechanism for Ostwald ripening is a vapor phase assisted transport.

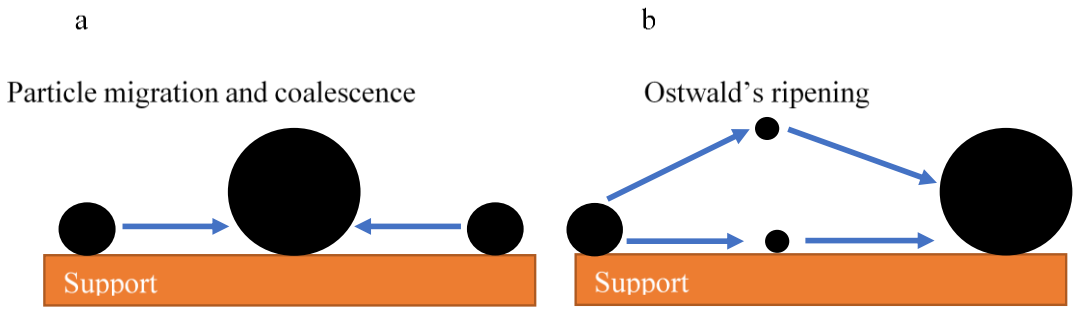

Figure 1.2 *Schematic illustration of the sintering mechanism of supported nanoparticle a) Particle migration and coalescence b) Ostwald ripening*

1.4 Ostwald Ripening

As discussed earlier in this dissertation OR is the process in which large particles form because of the migration of adatoms through support or vapor phase assisted route.[7] The thermodynamically driving force for this phenomenon is governed by Gibb's Thomson equation as shown below.

$$\mu = \mu_{\circ} + \frac{2\Upsilon\Omega}{r} \text{.....eq 1.1}$$

Where μ is a chemical potential of a small metal particle.

$\mu_{\circ}$ is the chemical potential of the bulk metal.

ϒ is the surface free energy of the particle.

Ω is the atomic volume and r is the radius of the metal particle.

If the radius of the metal particle is small, then the value of the 2ϒΩ/r will go up as a result the chemical potential of the small metal particle increase by the factor of 2ϒΩ/r. On the contrary, if the radius of the metal particle is abnormally large, then the value of 2ϒΩ/r is almost negligible. At that circumstance, essentially the chemical potential of the metal particle is equal to the chemical potential of the bulk material. This relation shows

that the chemical potential is inversely proportional to the metal particle size. The smaller metal particles have high surface free energy and these metal particles are more prone to OR. Consequently, these metal particles become smaller and smaller over time and eventually disappear. On the other hand, some particles grow and become anomalously large and reach to the thermodynamically stable form.

CHAPTER 2: MATERIALS AND CHARACTERIZATION TECHNIQUES

2.1 Characterization Techniques

It is very important to characterize the catalyst to understanding nature as well as the state of the catalyst before and after reaction conditions. Under realistic reaction conditions, many things happen to alter in catalyst state such as surface area, the oxidation state of the catalytically active phase, the particle size of the active center, its structure and composition, and beyond that change in physical and chemical properties of the support. The fundamental understanding of the change of working catalysts helps to design or engineer the robust, stable, and durable catalysts. In this study, the following techniques such as scanning electron microscopy (SEM), energy dispersive spectroscopy (EDX), transmission electron microscopy (TEM), aberration-corrected scanning transmission electron microscopy (AC-STEM), low energy ion scattering (LEIS), X-ray diffraction (XRD), X-ray photoelectron spectroscopy (XPS), X-ray absorption spectroscopy (XAS), diffuse reflectance infrared Fourier transform spectroscopy (DRIFTS) and chemisorption were incorporated to characterize the catalysts. This chapter will cover a brief overview of some of these characterization techniques.

2.2 Electron Microscopy

The word microscope was originated from the ancient Greek (mikros means small and skopien means to see or look). The small features that cannot be seen through the naked eyes can be observed under a microscope by magnifying the features to a serval order of magnitude. A common microscope is an optical microscope in which the light (photons) passes through several lenses to magnify the object. However, it has limited resolution.

The highest resolution so far in the optical microscope is 200 nm. The development of the electron microscope happened as a result of limited resolution provided by an optical microscope. Electron microscope works in the same way, but the difference is that in an electron microscope accelerated electrons are used as a source rather than light.

2.3 Transmission Electron Microscopy

When the light microscope cannot resolve the materials then transmission electron microscopy (TEM) is employed to observe the materials. In the case of a light microscope, light interacts with the materials and the wavelength of light is high, so the resolution of a light microscope is limited. On the contrary, electrons interact with materials in the electron microscope. The electron has a low wavelength as opposed to light, as a result, TEM can image at a significantly high resolution up to the atomic scale. This technique has been extensively used by different branches of science such as physics, chemistry, biology, material, medicine, semiconductor, and so on. It is a very powerful technique to study the materials. The TEM in our facility contains a field emission gun (FEG) as an accelerated electrons generator. The FEG acts as a cathode with two functioning anodes; one anode helps to generate electrons from the gun and another anode axillary to speed up the electrons through the column. These accelerated electrons pass through the series of lenses and samples and ultimately produces the image. Since my projects are mostly related to nanometer size particles and single atoms, therefore, my projects intensively needed the use of TEM at the UNM facility and the aberration-corrected transmission electron microscopy (AC-TEM) for the

characterization of single-atoms catalysts. AC-TEM was used to locate single-atom Pt and its position on the catalyst supports.

2.4 Aberration Corrected Scanning Transmission Electron Microscopy

The improvement in the resolution of the microscope involves improvement in the probe size. The probe size can be focused down to the size below 0.07 nm by improving the spherical aberrations in the microscope. This probe size in the microscope able to resolve the individual atoms. The miracle advancement in computer technology made it possible to correct the spherical aberration by improving the focus of all the rays being transmitted. The aberration-corrected STEM images were obtained using a JEOL NeoARM equipped with a cold field emitter and the UHR polepiece (resolution 0.07 nm) at the JEOL NeoARM factory, capable of resolving single atoms with the capability of obtaining both BF and HAADF images simultaneously. This microscope is equipped with an EDS detector to give compositional information of the imaged sample. This microscope allowed us to analyze the exact sites and quantify the single atom per unit area of support. The high resolution of the microscope will also give us information on the atomic scale, revealing individual atoms on the catalyst support.

2.5 Scanning Electron Microscopy

Scanning electron microscopy (SEM) is another powerful technique to study materials at the nanoscale. In this technique, the sample of interest is bombarded with electrons gun. The bombarding electrons interact with the materials to generate a variety of signals such as backscattered electrons, secondary electrons, cathodoluminescence, transmitted

electrons, and X-rays. These varieties of signal carry different information as shown in table 2.1

Table 2.1 Different signal in SEM gives different important information.

Signal	Information
Backscattered electrons	Image produced based on atomic number differences
Secondary electrons	Topographic information
Cathodoluminescence	Electronic structure and chemical composition of materials
Transmitted electrons	The inner surface and the crystal structure of the materials
X-rays	Chemical composition
Auger electrons	Chemical composition
Reflected light	Topographic and crystallographic

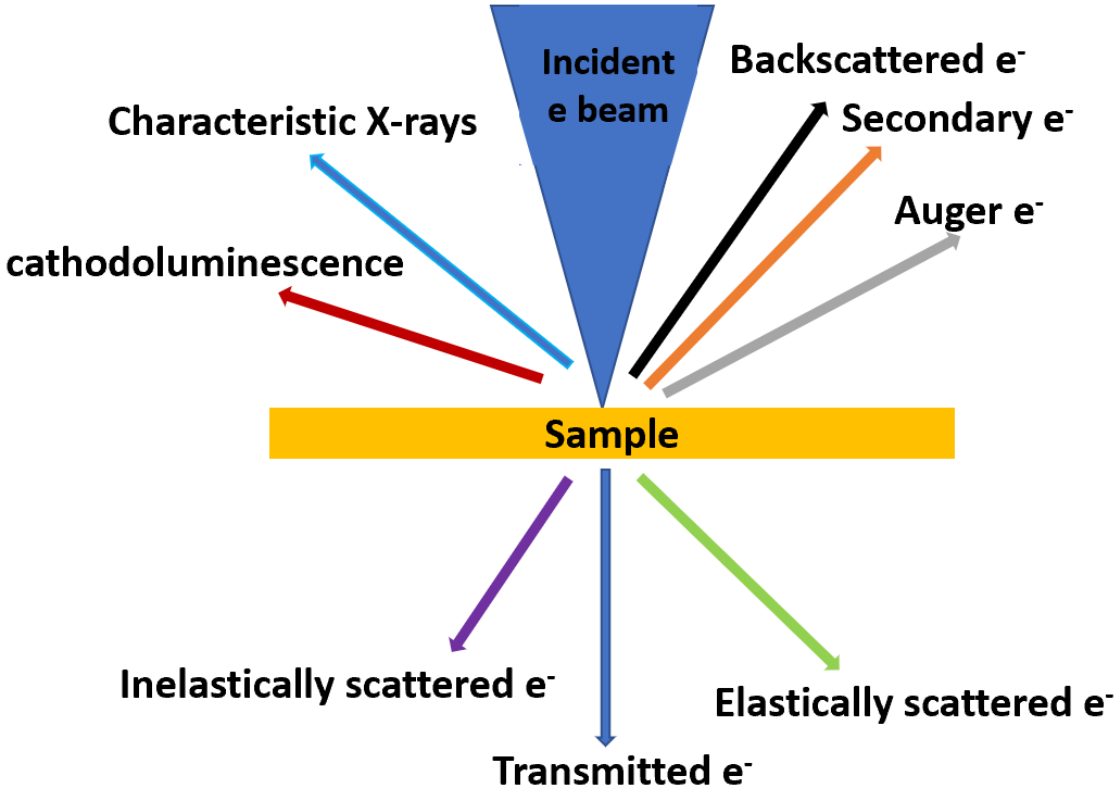

Figure 2.1. *Illustration of electron and matter interaction on SEM*

Another important feature that SEM contains is electron dispersive spectroscopy (EDX). The SEM-EDX system is extensively used and becomes popular to determine the elemental composition qualitatively as well as quantitatively of the materials. Qualitatively, it identifies the elements and quantitively, it gives the concentration of each element present in the sample in the form of atom percent or weight percent. Every element contains a unique number of electrons that reside in different orbits as shown in figure 2.2. These different orbits have discrete energies levels. When the incident electrons bombarded on the materials, the incident electron ejects the electron from the K shell and creates the hole. The electron jumps from the higher energy level to the lower energy level to fill up the hole. During this process, a characteristic X-rays are produced. These characteristic X-rays are dependent on the atomic number of elements, which is a

unique property and fingerprint of each element. These x-rays are used to identify the elements present in the material. Silicon-drifts detectors are employed to detect the X-rays in SEM. These detectors are placed very close to the sample at an angle and can measure the energy of photons that belongs to the X-rays.

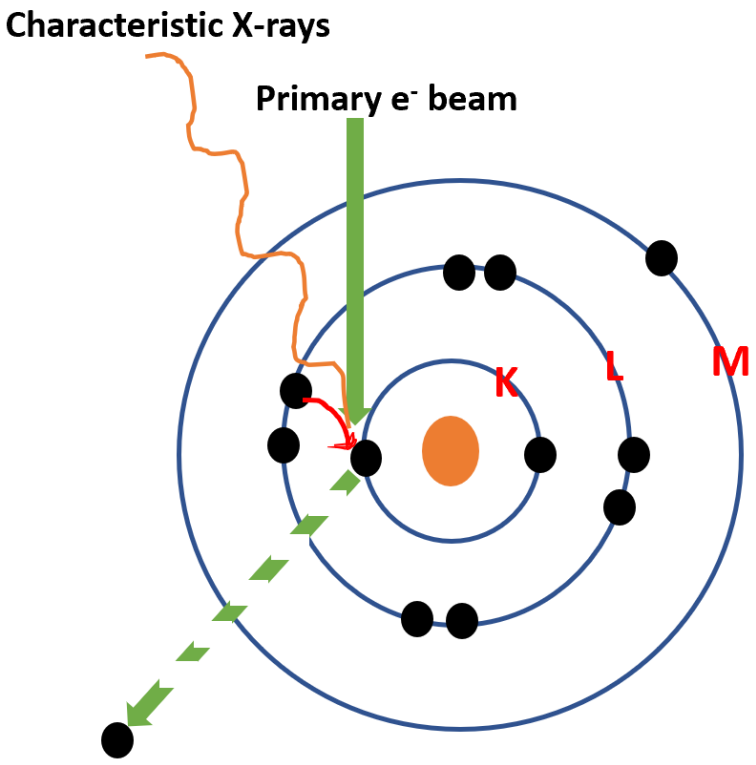

Figure 2.2: *Illustration of X-rays generation process.*

2.6 Energy Dispersive Spectroscopy

As aforementioned the X-rays are produced when the electron jumps from the higher energy level to the lower energy level to fill up the hole. X-rays are usually detected by energy dispersive spectrometer (EDX) in SEM. The SEM comes with the EDX detector system with lithium drifted silicon crystal (Si(Li)) detector that detects the X-rays of all energies. The actual charge induced in the detector is very small therefore, to mitigate the

noise to a minimum, a field-effect transistor (FET) is placed as close as to the Si(Li) detector and provides the first stage of signal amplification. The system is operated under liquid nitrogen temperature to limit the mobility of Li in Si. The required temperature is maintained by connecting the detector and FET through an efficient heat conductor to a liquid nitrogen dewar.

To distinguish most of the X-ray lines, the spectral resolution associated with EDX is usually more than 150 eV. Quantitative analysis software is used to separate severe overlaps of peaks. Many artifacts are possible in EDX, but most of them come from detector electronics and rarely seen in a properly functioning system. However, two artifacts (pileup peaks and silicon escape peaks) are common. Lowering the beam current to the lower count usually eliminates the problem. The data generated by the EDX system is presented in the form of spectra as shown in figure 2.3. Each spectrum at different energy levels corresponds to a specific element. I have used this technique extensively to quantify the loss of Pt from model thin-film catalysts which has been presented in section 2.

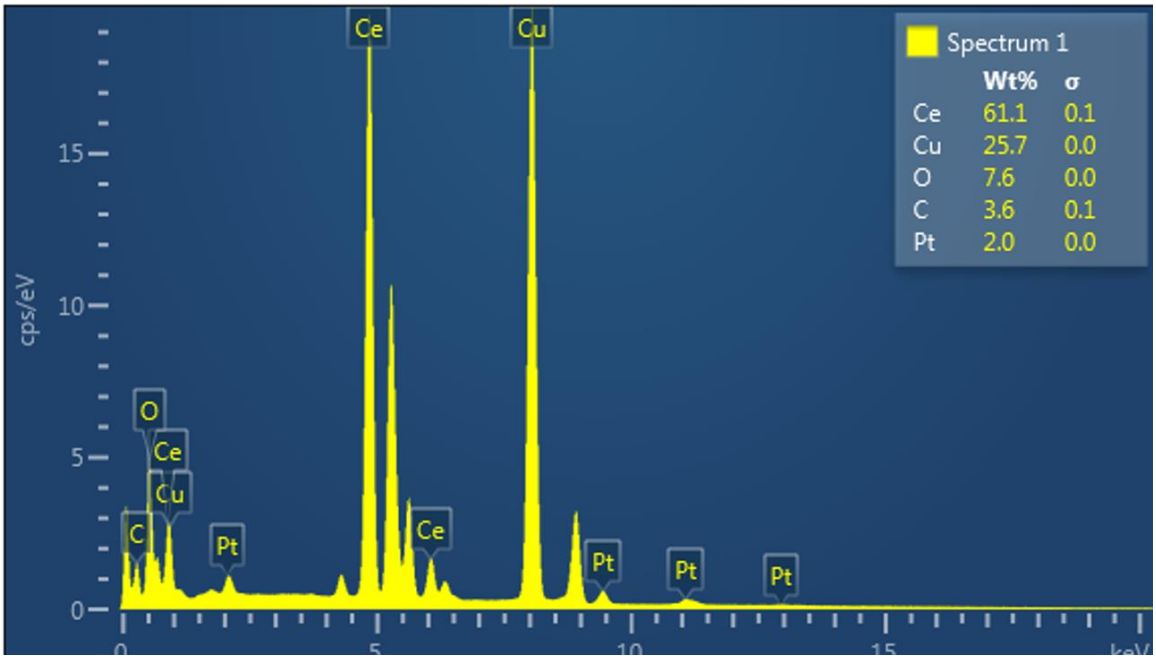

Figure 2.3: *EDX spectra for Pt/Ceria catalyst showing the presence of different elements.*

2.7 Low Energy Ion Scattering

Low energy ion scattering (LEIS) is a very surface-sensitive technique. It detects and quantifies the topmost layer of atoms of the materials. In this technique, the noble ions ($3He^+$, $4He^+$, Ne^+, Ar^+…) with the energy of certain KeV are bombarded on the surface of the sample. The ions are scattered by the topmost atoms of the surface and these scattered ions are perfectly elastic in nature. Additionally, these backscattered ions obey the laws of conservation of energy and momentum. By measuring the energy of these backscattered ions, the energy of corresponding scattering ions is determined and quantified. The principle of this technique is shown in figure 2.4.

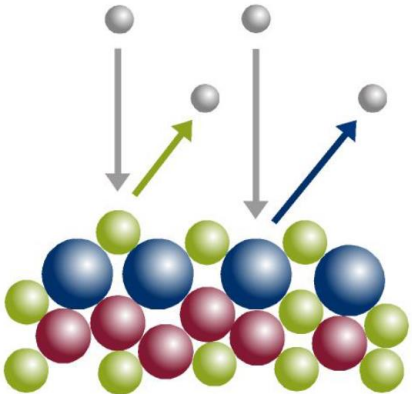

Figure 2.4: *Showing the principle of low energy ion scattering.*

In this study, we analyzed our catalysts with $Qtac_{100}$ which a highly surface sensitivity low energy ion scattering instrument. It truly provides the elemental and structural characterization of the top atomic layer of the catalysts. The key features of these techniques are as follows.

- Reliable and straightforward quantification
- Quantitative, element characterization of the topmost atomic layer
- Spectroscopy, imaging, and depth profiling capabilities
- Detection of all elements apart from H and He
- Non-destructive in-depth analysis
- Sensitive to isotopes
- Time-of-flight mass filtering for improved sensitivity
- Analysis of rough and non-conductive materials
- Detection limits Li-O ≥ 1%, F-Cl =1%-0.05% and K-U =500 ppm-10 ppm

Low energy ion scattering can be operated in three different modes. These different modes provide different information. For example, surface spectroscopy and imaging mode provide the quantitative elemental information of the topmost atomic layer for the

elements above helium in a sample. Likewise, the static depth profiling mode provides the elemental in-depth information non-destructively by measuring the energy loss of ions scattered at sub-surface layers. In LEIS, most of the ions detected are scattered at the surface. Those scattered from atoms below the surface lose additional energy proportional to the depth at which the scattering occurred. By measuring this energy loss, the elemental composition of sub-surface layers is determined non-destructively. This static depth profiling provides information down to a depth of 10 nm. This mode also allows a quantitative measurement of the thickness of organic overlayers such as Langmuir-Blodgett films of self-assembled monolayers. Similarly, sputter depth profiling provides the high-resolution chemical depth profiles by using a low-energy sputter ion source in a dual-beam mode.

2.8 Analysis of Single-Atom Pt/Ceria Catalysts

We analyzed samples from 1-4% Pt/Ceria, 0.5wt%Pt/ 2%K Spinel, 2wt%Pt@AT ceria along with ceria, and spinel as references with LEIS technique. In addition to these, a Pt reference sample was also analyzed after sputter cleaning of the sample. All the samples with ceria, spinel, and Pt reference were treated with O atoms in situ at room temperature in order to remove all the non-essential things adsorbed on the surface of these samples. Furthermore, the assumption was made that Pt on the outer surface of Pt reference as well as Pt/support catalysts had converted into PtO_2. The goal of the analysis was to determine the concentration of the single-atom Pt on Pt/Ceria samples. To achieve this, the Pt surface fractions were determined by LEIS and a theoretical surface fraction was calculated based on the single Pt atom adsorption assumption. Assuming that Pt consists

of cube shape Pt atoms, the specific surface area (A_{Pt}) for a (one-sided) single-atom layer of Pt in m^2/g is given by

$$A_{Pt} = \frac{N_{Av}\, d_{Pt}^2}{M_{Pt}} \text{.....eq 2.1}$$

Where, N_{Av} is Avogadro's constant, M_{Pt} is the atomic weight of Pt and d_{Pt} is the size of the Pt atom. PtO_2 Molecule is considered as a cube as shown in figure 2.5 and dPt can be calculated from the atomic volume.

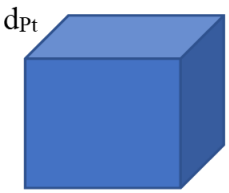

$$d_{Pt} = \sqrt[3]{\frac{M_{Pt}}{\rho_{Pt} N_{Av}}} \text{.....eq 2.2}$$

Figure 2.5. PtO_2 molecule is considered as a cube, the length of two sides of a cube is d_{Pt}.

Where ρ_{Pt} is the density for Pt. This leads to the surface area of Pt (A_{Pt}) of 189 m^2/g.

The theoretical surface fraction of Pt on a single atom catalyst (S_{theor}) can be calculated from the loading of Pt weight percent (W_{Pt}) and the catalyst's specific surface area (Acat) from BET surface area measurement.

$$s_{\text{th}\,eor} = W_{Pt} \frac{A_{Pt}}{A_{Cat}} \text{.....eq 2.3}$$

The actual Pt surface fraction can be analyzed with LEIS. This is done by a comparison of the Pt signal from the sample to that of the Pt reference. The samples and the reference need to be in the same condition, so the samples and references are compared after the O atom treatment.

$$S_{LEIS} = \frac{Y_{Pt\ Sample}}{Y_{Pt\ Reference}} \text{.....eq 2.4}$$

The surface analysis was done by bombarding two ions $4He^+$ and $20Ne^+$ with accelerated ion energy 3 KeV, 6 KeV in the case of He ion, and 5 KeV in the case of Ne ion. The analysis current was 5 nA and 2 nA respectively. And the scanned area was 2×2 mm^2. The ion dose in the case of He ion was given to 1.4×10^{14} ion/cm^2 and in the case of Ne ion was given to 2.8×10^{23} ions/cm^2. The spectra for the Pt reference were analyzed within a 1.5×1.5 mm^2 sputter crater over an area of 1×1 mm^2. The analysis time was adjusted such that the surface damage was the same as for the other spectra. Assuming a sputter coefficient of 0.1 for He and 1 for Ne, this will lead to surface damage of 1% and 2% at the end of the analysis.

The measured LEIS surface fraction and the theoretical surface fraction for single atoms as a function of Pt wt% loadings are shown in table 2.2 and figure 2.6.

Table 2.2: LEIS surface fraction for different Pt loading wt%.

Pt loading wt%	LEIS surface fraction %	Exponential fit	Frank-van-der Merwe (FM)
0.00	0.00	0.00	0.000
0.50		1.324	1.450
0.95	2.45	2.335	2.755
1.50		3.376	4.350
1.74	3.58	3.772	5.046
2.00		4.165	5.800

2.50		4.830	7.250
2.72	5.13	5.088	7.888
3.00		5.389	8.700
3.20	5.66	5.681	9.570
3.50		5.859	10.150

Frank-van-der Merwe (FM) or layer by layer growth. In this growth model, it is assumed that all the atoms of the Pt loading are in the outer atomic layer and no shielding effect is considered.

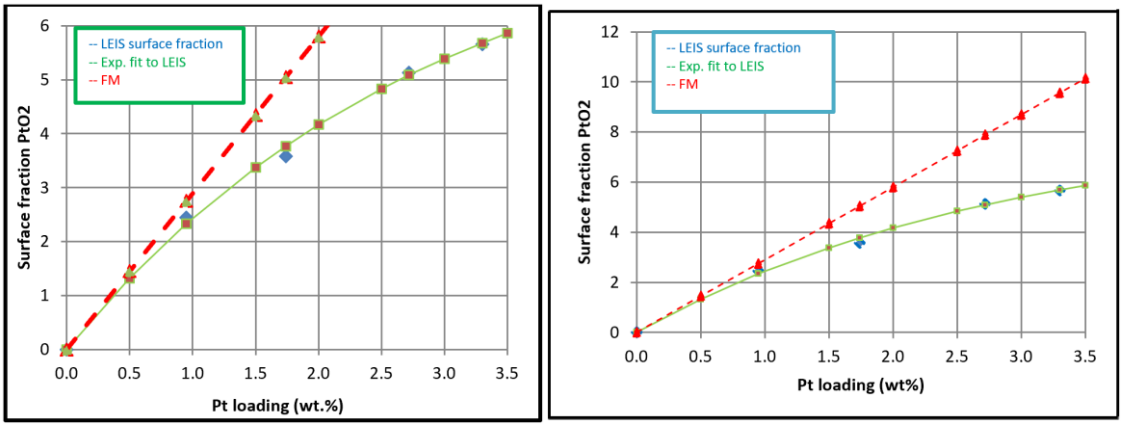

Figure 2.6 The experimentally measured single-atom Pt fractions by LEIS were compared to the theoretical surface atoms fractions.

The measured LEIS surface fraction is shown by blue and the theoretical surface fraction for single atoms as a function of Pt loading is shown by red in figure 2.6. At low loading, all the Pt is present in the form of single atoms. In 3 wt% Pt/Ceria catalyst more than 80% of the Pt is present in the outermost atomic layer but in 4 wt% Pt/Ceria catalyst 69% of the Pt atoms are in the topmost layer of the catalyst. In this technique, it is considered that any Pt on the side of the particle is also in-depth and shows the shadow effect.

Table 2.3: Concentration of Pt atoms/nm^2 calculated from the LEIS method

Pt loading wt%	Loading PtO_2/nm^2	LEIS Pt at./nm^2	Exponential Fit Pt at./nm^2	FM Pt at./nm^2
0.00	0.00	0.00	0.00	0.00
0.50			0.20	0.22
0.95	0.33	0.37	0.35	0.41
1.50			0.51	0.65
1.74	0.60	0.54	0.57	0.75
2.00			0.63	0.87
2.50			0.73	1.08
2.72	0.88	0.77	0.76	1.18
3.00			0.81	1.30
3.20	2.26	0.85	0.85	1.43
3.50			0.88	1.52

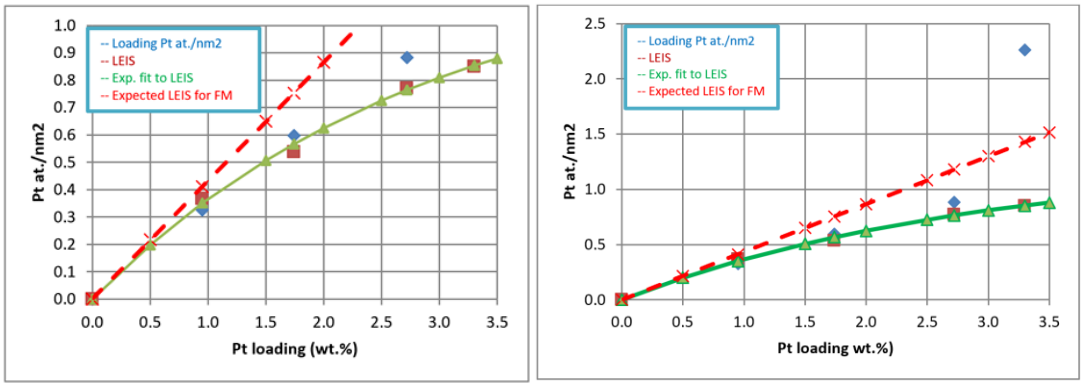

Figure 2.7: *The experimentally measured single-atom Pt atom/nm^2 by LEIS was compared to the theoretically expected Pt atom/nm^2.*

Table 2.4. Estimation of surface concentration of the Pt reference foil via LEIS

	Molecular mass (g/mol)	Density (ρ) (g/cm^3)	Volume (nm^3/mol)	Area (nm^2/mol)	PtO_2 atom/nm^2
PtO_2	277.08	10.2	$37.0E^{-2}$	$11.2E^{-1}$	9.01
Pt	195.08	21.5	$1.51E^{-2}$	$6.10E^{-2}$	16.04

Volume (nm^3/mol)= $\{(Mass/\rho)*10^{21}/6.023*10^{23}\}$=1.660*10-3*M/ρ…….eq 2.5

V=227.08 $gmol^{-1}$/10.2 gcm^{-3}=(22.26 mol^{-1} $cm^3\times10^{21}$ nm^3 cm^{-3})/6.02×10^{23} molecules mol^{-1} = $37.0E^{-2}$ nm^3/molecule ……..eq 2.6

Area (nm^2/mol) = $(Volume/mol)^{2/3}$ ……eq 2.7

Table 2.5. Calculation of surface concentration from ICP-OES, BET surface area, and LEIS.

Nominal loading	Actual loading (ICP)	Pt at./g support (10^{19})	BET (m^2/g)	PtO_2/nm^2 N_{PtO2}	LEIS Spt cts/nC	LEIS surface fraction%	LEIS Pt at./nm^2
CeO_2	0	0	130	0.00	0	0.00	0.000
1%Pt/ CeO_2	0.95	2.93	90	0.33	167	2.45	0.367
2%Pt/ CeO_2	1.74	5.37	90	0.60	244	3.58	0.537
3%Pt/ CeO_2	2.72	8.39	95	0.88	350	5.13	0.770
4%Pt/ CeO_2	3.20	10.18	101	2.26	386	5.66	0.849

Pt reference (O-atom treated) = 6820

Number of Pt atom by LEIS (N_{Pt}^{LEIS})=($S_{Pt}^{Cat}/S_{Pt}^{ref}$)×$N_{PtO2}/R_{sup}$ …….eq 2.8

Where Rsup=0.6, it is the roughness factor by which the LEIS signal is reduced, due to the roughness of the support.

Since the surface of the Pt reference and that of the catalysts has been fully oxidized (O-atoms) at room temperature. $N_{Pt} = N_{PtO2}$

The single of the reference (6820) corresponds to 9.01 PtO_2 molecule/nm^2

Pt atoms/nm^2 = S_{Pt}×9.01/(Rsup×6820) ……eq 2.9

2.9 X-ray Diffraction and Quantification of Metallic Pt

The atoms of a crystal scatter the X-rays that produces an interface effect. The diffracted X-rays obey the Bragg's law that gives rise to the information of the crystal such as the average crystallite size, the amount of the crystalline materials, and the identification of the phases of the material.

Bragg's law defines the relationship of angle, ϴ, and distance between the plane of atoms in a crystal

λ=2dsinϴ……..eq 2.10

Where,

λ= Wavelength of the X-ray

d= distance between two planes of atoms

ϴ= Angle between incident and diffracted beam

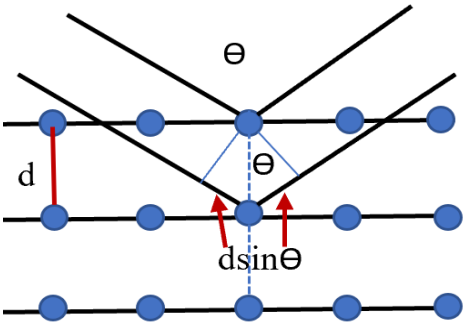

Figure 2.8. *Atoms of crystal diffracting the X-ray obeying Bragg's law.*

XRD is a powerful technique that has been extensively used in physics, chemistry, biophysics, and nanomaterials science to get the necessary information about the material qualitatively as well as quantitatively. Qualitatively, it can identify the ID phase with comparison to standards patterns. Estimates the proportions of phases by comparing peak intensities attributed to the identified phases with standard intensity ratios. Quantitatively, it determines the amounts of different phases in multi-phase samples based on the precise determination of diffraction intensity and/or determination of the fit of the pattern of each phase to the characteristics of that phase (i.e., amount, crystal structure, crystallite size, and shape). Though it is not a direct technique to quantify the atomically dispersed phase, however, indirectly it can be used to quantify the atomically dispersed phase in the sample. We used XRD as an indirect technique to quantify the atomically dispersed phase in the sample which will be discussed in detail later in the manuscript. Crystallite size information can be obtained from the widths of the Bragg diffraction peaks through the Sherrer equation: This equation is used to estimate the average particle size of the crystals from the measured width of their diffraction curves.

$$\tau = \frac{K\lambda}{\beta \cos\theta} \quad \text{.....eq 2.11}$$

Where τ is the mean crystallite dimension.

K is the shape factor (typically about 0.9)

λ is the wavelength, and

β is the FWHM width (equal to the B – b, B being the breadth of the observed diffraction line at its half-intensity maximum, and b the instrumental broadening)

θ is ½ of the diffraction angle 2θ

The Williamson-Hall Plot relies on the principle that the approximate formulae for size broadening, β_L, and strain broadening, β_e, vary quite differently with respect to Bragg angle, θ:

$$\beta_L = \frac{K\lambda}{L\cos\theta} \ldots\ldots\ldots\ldots\ldots\ldots \text{ eq 2.12}$$

$$\beta_e = C_\epsilon tan\theta \ldots\ldots\ldots\ldots\ldots \text{ eq 2.13}$$

One contribution varies as 1/cosθ and the other as tanθ. If both contributions are present, then their combined effect should be determined by convolution. The simplification of Williamson and Hall showed in figure 11 is to assume the convolution is either a simple sum or a sum of squares. Using the former of these then we get

$$\beta_{tot} = \beta_e + \beta_L \ldots\ldots\ldots\ldots\ldots\text{eq 2.14}$$

$$\beta_{tot} = C\tan\theta + \frac{K\lambda}{L\cos\theta} \ldots\ldots\ldots\ldots\text{eq 2.15}$$

If we multiply the above equation with Cosϴ, we get

$$\beta_{tot}\cos\theta = C_\epsilon \sin\theta + \frac{K\lambda}{L} \ldots\ldots\ldots \text{ eq 2.16}$$

Where

C_ϵ= microstrain

L= Crystallite size

Figure 2.9: Williamson-Hall Plot. **Figure 2.9**: *Williamson-Hall Plot.*

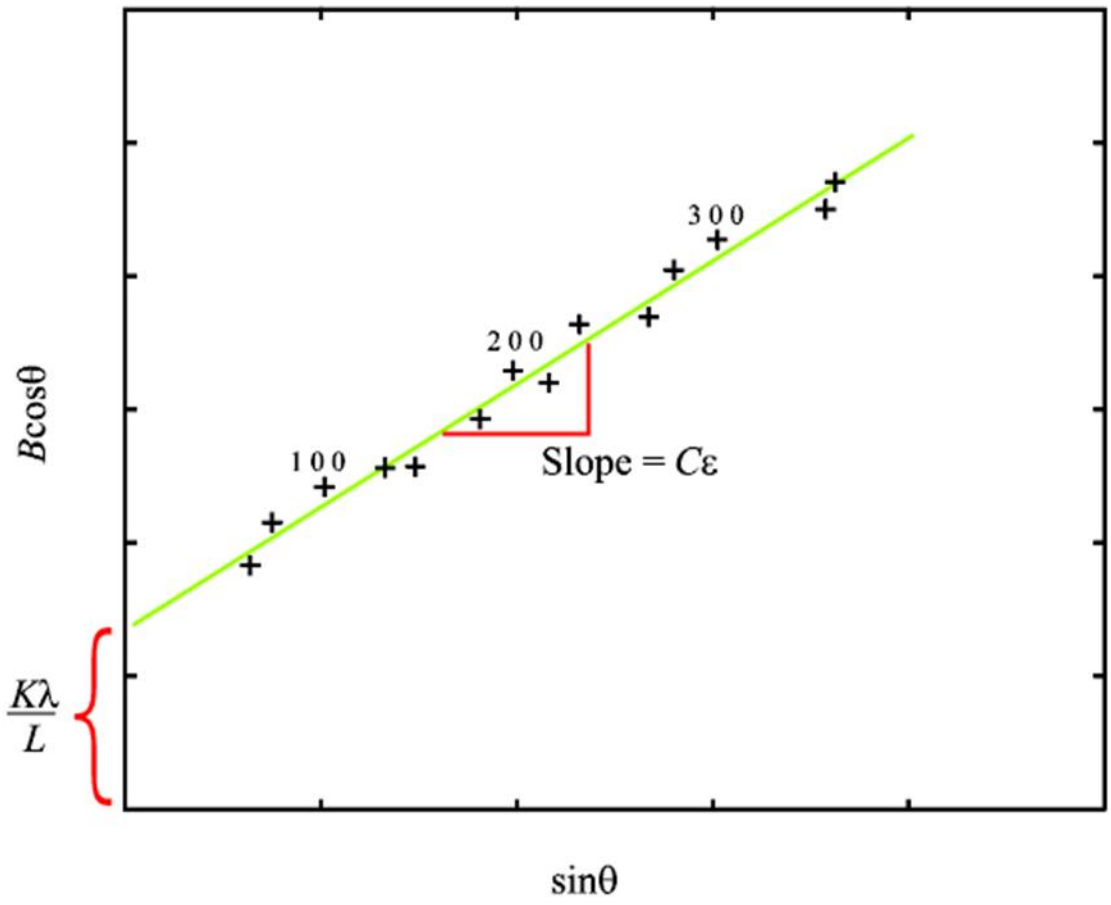

Figure 2.9: *Williamson-Hall Plot.*

CHAPTER 3: INVESTIGATING ANOMALOUS GROWTH OF PLATINUM PARTICLES DURING ACCELERATED AGING OF DIESEL OXIDATION CATALYSTS

This work has been published in the journal of applied catalysis B: Environmental

3.1 Introduction

The USDRIVE Low-Temperature after treatment (LTAT) test protocol requires the aging of diesel oxidation catalysts at 800 ˚C.[2] This high-temperature treatment for 50 hours simulates the degradation experienced by Pt catalysts after 150 K miles of driving. The catalysts lose activity due to the formation of large particles and the attendant decrease in metal surface area.[8] It is extremely important to stabilize the catalytically active Pt sites on support in order to extend the lifetime of working catalysts and to make efficient use of the limited global availability of Pt. Harris et al.[4] were among the first to recognize that 'anomalously' large Pt particles were formed on Pt/Al_2O_3 catalyst after aging in the air at 600 ˚C. Wynblatt[9] also reported the formation of 'abnormally large' Pt particles when the catalyst was aged at 20 kPa of oxygen during aging at 800 ˚C. Such large particles were not observed when the aging was performed at 2 kPa of oxygen. The mechanism for the formation of such large Pt particles is still under debate. Wynblatt[9] suggested that a morphological instability was responsible for forming large particles. Harris et al.[4] suggested that the particle growth mechanism during the first 2 hours of aging was interparticle transport, but no explanation was proposed for the 'anomalously large particles.' Graham et al.[8] reported that the anomalously large particles seen on the Pt only catalysts were not seen in any of the Pd containing catalysts.

At 800 ˚C in air Pt reacts with oxygen to form volatile PtO_2.[3] The vapor pressure in equilibrium with Pt is 1.6×10^{-8} atm which facilitates the transport of Pt[3]. In previous work[1]

we reported the transport of Pt from a Pt/La-alumina to physically mixed ceria particles leading to the formation of atomically dispersed Pt^{2+} species. A similar transport of Pt was found from Pt/$MgAl_2O_4$ to physically mixed PdO/La-alumina particles, forming Pt-Pd metallic nanoparticles.[10] The added Pd lowers the vapor pressure of Pt due to the solid solution, explaining in part the beneficial effect on particle size seen by Graham et al.[8] In previous work, we demonstrated that lowering the oxygen pressure during catalyst aging at 800 ˚C also led to the decreased particle size of Pt in the final catalyst.[5] All these observations suggest the formation and transport of PtO_2 vapor may play an important role in the formation of large Pt particles. To investigate this phenomenon further, we developed a model catalyst where the emission of Pt from catalyst powders could be quantified. We show that emission of Pt is rapid at 800 ˚C leading to loss of Pt if the catalyst is spread as a thin film on a surface over which air is allowed to flow. On the other hand, when air flows over a deep bed of catalyst, we do not see any loss of Pt. This is because the PtO_2 that would be emitted from individual catalyst grains in a thin film is trapped within the deep bed and deposits on the support forming anomalously large Pt particles. We show also how the catalyst support plays a critical role in modifying the emission of Pt and the resulting formation of large Pt particles.

In this work, we studied La-Al_2O_3, $MgAl_2O_4$, and CeO_2 support. La-Al_2O_3 is the most commonly used support in the automotive exhaust emission control catalyst. CeO_2 is commonly added to three-way catalysts to provide oxygen storage capabilities.[11] $MgAl_2O_4$ was used because it is thermally stable and has been reported to stabilize small nanoparticles of Pt ranging from 1–3nm[12] at elevated temperature. The goal of this work was to develop a method to quantify the emission of volatile Pt species from industrially

relevant catalysts. The vapor pressure of Pt is a thermodynamic quantity that can only be changed by alloying with other elements such as Pd, which have very low vapor pressure in oxygen. Since catalyst supports are known to modify the stability of Pt nanoparticles, the question remains whether the volatility of Pt can be influenced by the support. This study investigates the factors that lead to the formation of anomalously large Pt particles during the accelerated aging of diesel oxidation catalysts. Such large Pt particles represent a waste of a precious resource and understanding the origin of this phenomenon can help to avoid the formation of large Pt particles.

3.2 Experimental Details

3.2.1 Catalyst Preparation and Aging

Lanthanum stabilized alumina (La-Al_2O_3) support (MI-386) was obtained from SOLVAY Rhodia and contained ~5 wt% La_2O_3, with a BET surface area of 176 $m^2\ g^{-1}$. The particle size is 1-10 μm based on TEM images, the pore volume is 0.76 cm^3/g, and particle density 0.48 g/cm^3 as reported previously by Wang et al.[13] The BET surface area before and after 800 ˚C extended agings for the three supports is reported in Table 3.1. Magnesium aluminate ($MgAl_2O_4$), cerium nitrate hexahydrate (99.999% purity), and tetraamine platinum nitrate were purchased from Sigma Aldrich. Cerium nitrate hexahydrate was heated in a box furnace at 350 ˚C for 4 hours in order to make polyhedral ceria (CeO_2). 1wt% Pt was loaded on $MgAl_2O_4$, La-Al_2O_3, and CeO_2 using incipient wetness impregnation and evaporated to dryness at 80˚C. The dried catalysts were calcined at 500 ˚C/4 hours, 550 ˚C/4 hours, and 800 ˚C/10 hours, respectively, in flowing air in order to generate the initial catalyst. The higher temperature used for the preparation of the ceria

catalyst ensures that the Pt is atomically dispersed in the form of Pt^{2+} ions covalently bonded to the ceria support.

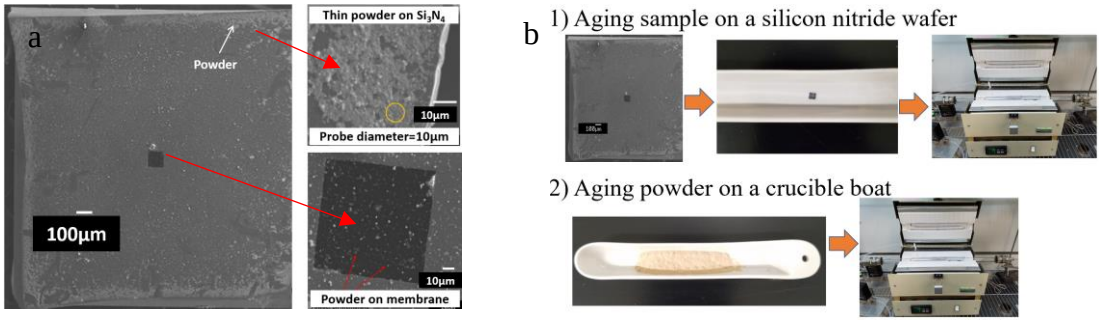

Fig. 3.1 *(a) The model catalyst consists of a silicon wafer with a silicon nitride surface layer. A square window (100×100µm) creates an electron transparent silicon nitride film which allows TEM imaging and a typical region analyzed via SEM is shown and (b) The experimental approaches for aging the catalyst powder: as a thin layer dispersed on silicon nitride film (b1) and as a powder in a deep bed in a ceramic crucible (b2).*

A small amount of the initial catalyst was dispersed in ethanol and mounted using a pipette on the TEM sample and spin-coated to make a thin film shown in Figure 3.1. We estimate that the amount of sample placed on the silicon nitride grid is 0.035 mg. This estimate assumes that ~1mg of the catalyst powder was dispersed in 1.0 ml of ethanol and 1 drop of the suspension was deposited on the TEM sample. As described later, by using such a small amount of sample we increase the sensitivity to detect the changes in Pt content due to emission to the vapor phase. The method for fabricating the TEM samples was described in detail in our previous work.[5] SEM images of the catalyst powder in the form of a thin film are shown in Figure 3.1a at differing magnifications. The square window at the center of the TEM sample allows imaging through the Si_3N_4 thin film. Two approaches were used for aging the powder catalyst. First, as a thin film on the TEM silicon nitride sample

as shown in Figure 3.1(b1) and second, using 500 mg of catalyst in a ceramic crucible boat as shown in Figure 3.1(b2). In both cases, the samples were placed in a quartz tube and treated at 800 ˚C for differing lengths of time in 100 cc/min of flowing air to generate the aged catalysts.

3.3 Characterization

After aging the powder catalysts on a silicon nitride surface at 800 ˚C, we determined the content of Pt using Scanning Electron Microscopy Energy Dispersive Spectroscopy (SEM-EDS), Wavelength Dispersive X-ray Spectroscopy (WDS) in an Electron Probe Microanalyzer (EPMA), and Transmission Electron Microscopy Energy Dispersive Spectroscopy (TEM-EDS). A typical region analyzed by SEM and TEM is shown in Fig. 3.1a. A total of 15 such regions were analyzed by SEM-EDS and TEM-EDS for Pt quantification. The average of these analyses was reported to determine the loss of Pt after each heat treatment. We also used ICP-OES to analyze the elemental composition of the crucible-aged $Pt/MgAl_2O_4$ sample. High-resolution transmission electron microscopy was carried out using a JEOL 2010F microscope. The catalyst was ground in a mortar and pestle and deposited on holey carbon support films after being dispersed in ethanol. Powder X-Ray diffraction (XRD) patterns were recorded with a Rigaku Smart Lab diffractometer using Cu Kα radiation and a Ni filter. XRD was also used to quantify the amount of crystalline Pt via Rietveld Refinement. CO oxidation was chosen as a probe reaction. Reaction rate measurements were performed using ¼ inch diameter U-tube with 20 mg of sample. The gas flow rates for CO oxidation were: CO 1.5 ml/min, O_2 1 ml/min and He 75 ml/min (space velocity 232,500 ml/g/h). The products were analyzed by a Varian CP-4900 Micro GC while the reactor temperature was ramped up at 2 °C/min. A Micromeritics

AutoChem 2920 instrument was employed for the CO chemisorption in order to determine Pt dispersion. 100 mg sample was measured and placed in a sample tube for each experiment. The sample was first treated in a mixture of 10% O_2/He for 1 hour at 350˚C, then treated with 10% H_2/Ar for half an hour at 350˚C. Helium was allowed to flow to the catalyst with the flow rate of 50 ml/min for 30 min in order to stabilize the catalyst temperature to 45 ˚C. The 10% CO/He pluses were injected into the sample tube to start the chemisorption measurement, and a TCD detector recorded the concentration signals. The CO-Pt adsorption ratio was assumed to be 1:1.

3.4 Results and Discussion

3.4.1 Aging of Pt Catalyst in the Form of a Thin Film

The thin-film geometry is designed to mimic the external surface of a wash coat in a honeycomb monolith used in a catalytic converter. We would expect that Pt emitted from the catalyst would be carried away in the flowing air and would lead to a decrease in the concentration of Pt. The initial samples, as-prepared and calcined, were found to contain ~1 wt% Pt via SEM-EDS, close to the nominal loading. STEM images of Pt/La-Al_2O_3 and Pt/$MgAl_2O_4$, Figure 3.2 (a, b), show small and well-dispersed Pt nanoparticles in the initial catalyst, with the alumina having smaller particles than the spinel. More images are shown in Appendix I (Figures I.1 and I.2). After aging the catalysts at 800 ˚C for 30 hours no Pt nanoparticles were observed, as shown in Fig. 3.2(e, f) suggesting that all the Pt evaporated from the catalysts in the form of volatile PtO_2 after 30 hours of aging. This observation of Pt loss is consistent with the observations by Porsgaard et al.[14] who heated their samples up to 600 ˚C in 0.5 Torr of oxygen and observed a 50% loss of Pt. Likewise, Fryburg and Petrus[15] measured the transport of Pt from a heated ribbon in the presence of oxygen to the

cold walls of their glass apparatus. They reported that PtO_2 emitted from the surface can collide with gas-phase molecules and return to the surface. The probability of emission decreased from one at low pressures to 0.006 at an oxygen pressure of 15×10^{-6} Torr. If we extrapolate to the pressure used in our study (21% oxygen, 630 Torr total pressure) we can see that the rate of Pt oxide emission can be significant. Once the PtO_2 is formed in our experimental set up, it is swept away by flowing air. This explains why we see the complete loss of Pt after 7 hours of aging at 800˚C. To derive the time dependence of Pt, we studied the thin film samples via SEM-EDS (Figure 3.3a). The experimental error by SEM-EDS is within ± 15%. Elemental analysis was also performed via TEM-EDS and WDS to corroborate the SEM-EDS and the agreement was excellent.

We observed rapid loss of Pt from the Pt/La-Al_2O_3 and Pt/$MgAl_2O_4$ via SEM-EDS with almost all the Pt lost after 7 hours of aging at 800 ˚C in flowing air. The linear relationship between Pt content and time of aging is consistent with a constant vapor pressure of Pt regardless of the amount of Pt remaining in the sample. The similar rate of loss for both supports suggests a similar internal pore structure causing a similar resistance to mass transfer of the Pt species from the particles to the gas phase. For each sample, 15 regions were analyzed via SEM-EDS and the average of these measurements is shown in this figure. The amount of Pt left after aging for 7 hours on the Pt/$MgAl_2O_4$ and Pt/La-Al_2O_3 is close to the detection limit of this technique. If we assume that all of this Pt was vaporized and carried by the flowing gas, we would expect a gas-phase concentration of Pt which is ~5% of saturation. The details are provided in Appendix I table I.1. In contrast, in the case of ceria, the entire amount of Pt was retained on the support without any detectable loss even after aging for 30 hours.

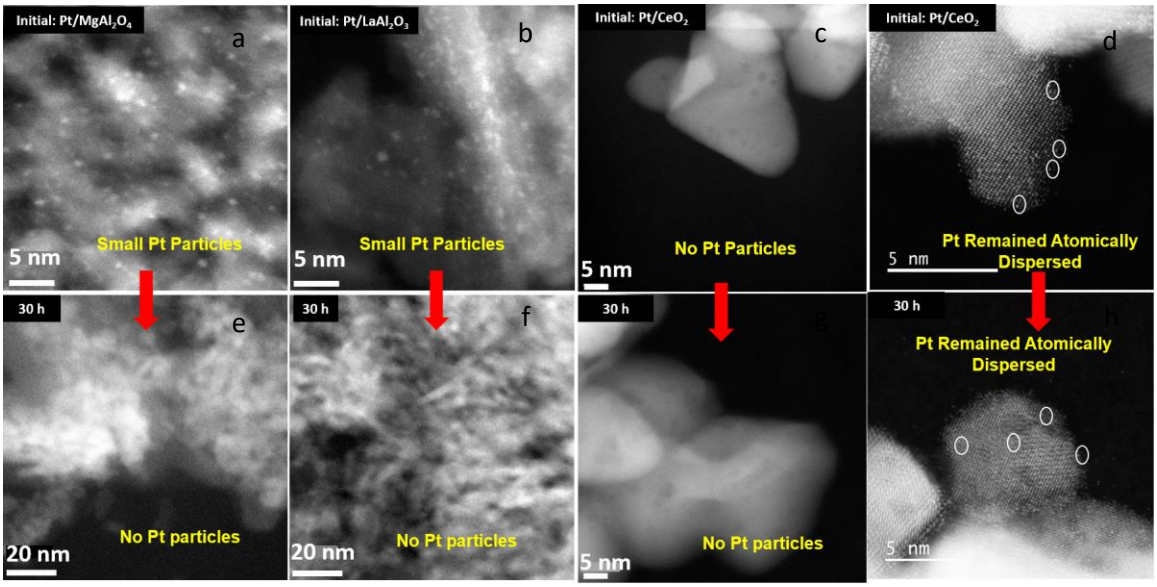

Figure 3.2. *STEM images of (a–c) initial catalyst and (e–g) after aging for 30 h at 800 °C in flowing air on a thin film. Images d and h are AC-STEM images showing Pt*

Interestingly, we did not find any Pt particles in the STEM images on the ceria support both in the initial catalyst (which was already aged at 800 °C for 10 h during catalyst preparation) as well as after additional aging for 30 hours, as shown in Figure 3.2 (c, g). However, The EDS data shows the Pt content on the ceria support is unchanged after aging for 30 hours. Aberration corrected (AC) STEM images of the initial and the 30 hours aged sample show clearly resolved white dots corresponding to Pt atoms. Similar images have been reported in our previous work on ceria.[1,16] The atomically dispersed Pt was strongly bound to the step edges of ceria (111) as first shown by Dvorak et al.[17] The strong binding of Pt to ceria apparently prevents the evaporation of Pt which explains why the Pt content remained unchanged. The schematic in Figure 3.3 shows why the behavior of the ceria support is so different since the oxidized Pt bound covalently to ceria does not further react with oxygen to form volatile species.

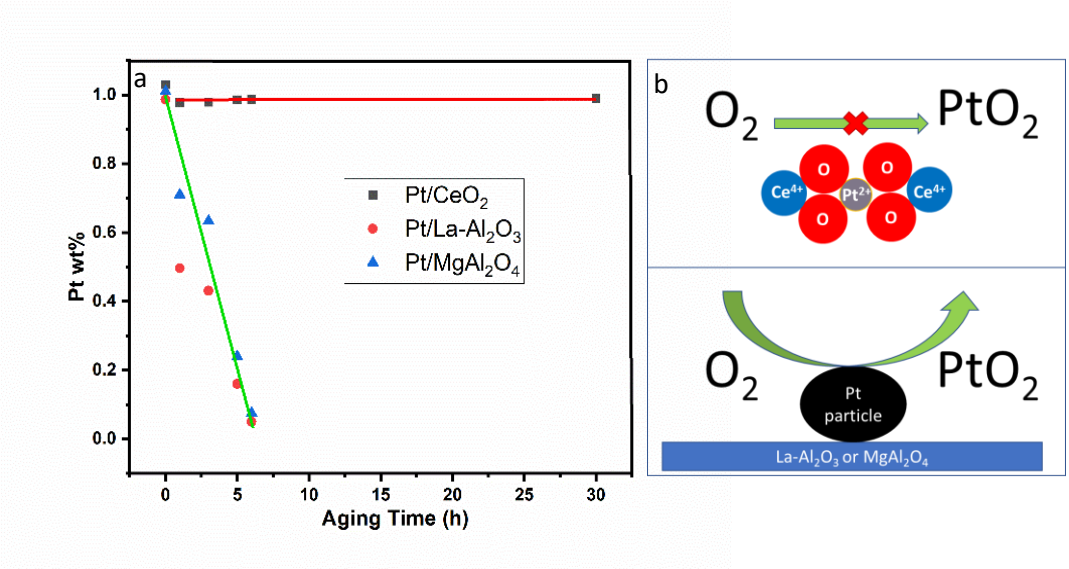

Figure 3.3 a) *Pt content (via SEM-EDS) as a function of time (hours) after aging from catalyst thin films on model TEM sample and b) Schematic showing the different states of Pt on the ceria versus the La-Al_2O_3 and the $MgAl_2O_4$ supports.*

The difference in the loss of Pt between the supports (Figure 3.3a) can be explained on the basis of the interaction chemistry between Pt and the support. Pt interacts with ceria through Pt-O-Ce bonds which cause the Pt to bind strongly to ceria.[6,17,16] While the stabilization of Pt by ceria was documented by Nagai et al[6], it was in the context of maintaining small Pt particle size. Here, we demonstrate, through the use of model catalysts, that ceria also helps to prevent the volatilization of Pt. Our work shows how the volatilization of Pt can be related to the anomalous growth of Pt particles during aging, which the ceria helps to prevent. At ceria (111) step edges, Ce^{3+} ions are under coordinated and available to bind to PtO_2 species that are delivered through the gas phase, forming covalent bonds to form Ce^{4+} as illustrated in Figure 3.3b.[16] DFT calculations showed that Pt-CeO_2 interaction at step edges is very strong, with a Pt binding energy of 7.72 eV. We refer to the platinum as ionic because EXAFS and XPS are consistent with Pt^{2+}.[16] In

analogy with the compound Platinum (II) bis (acetylacetonate) where the Pt has oxidation state +2 but the bonding to the ligand is covalent, we refer to Pt as being covalently bonded to the ceria through oxygen ligands. As shown in the schematic in Figure 3.3b, the trapped ionic Pt species do not react with oxygen and hence are stable during heating in air at 800 ˚C. However, a nanoparticle of Pt reacts with oxygen to form PtO_2, a process that is energetically uphill by 3.04 eV but is feasible at the high temperature used for the aging. The reaction of Pt to form volatile PtO_2, when supported on La-Al_2O_3 and $MgAl_2O_4$, causes the loss of Pt as shown in Figure 3.3a. The difference in emission rate on ceria and the other supports can be related to the different starting points. In the case of ceria, we start with Pt ions which were created through the method of atom trapping. These Pt ions being stable do not emit to the gas phase and we see no loss of Pt.

3.4.2 Aging of Pt Catalyst in a Ceramic Crucible Boat

Table 3.1 shows the BET surface areas of the three catalyst samples before and after 30 hours of aging in air. The spinel support lost 22% of its BET surface area after 30 hours of aging. In contrast, the La-Al_2O_3 support was more stable, losing only about 7% of the initial surface area. The presence of La is known to stabilize the alumina surface area. While ceria is known to lose surface area after aging, we have shown previously that atomically dispersed Pt helps to maintain BET surface area[1] due to the strong interaction between Pt and ceria.[16]

Table 3.1: BET surface area of initial catalysts and aged (800˚C/30 h) catalysts.

Catalysts	BET surface area of initial catalysts (m^2/g)	BET surface area of aged catalysts (800 ˚C/30 h) m^2/g	BET surface area aged in steam (800 ˚C/4 h) m^2/g
1wt% Pt/CeO_2	32	30	
1wt% $Pt/La\text{-}Al_2O_3$	190	178	160
1wt% $Pt/MgAl_2O_4$	142	110	80

The content of Pt in the initial catalysts was determined via TEM-EDS, WDS, and SEM-EDS. Since the sample size for crucible aging was 500 mg, it was possible to perform more accurate elemental analysis. The $Pt/MgAl_2O_4$ initial and 30 hours aged samples were analyzed by Galbraith laboratories using ICP-OES. The initial catalyst had 1.1wt% Pt while it was 1.13wt% Pt after aging for 30 hours, indicating there was no loss of Pt into the vapor phase from the deep bed. If flowing gas was saturated in PtO_2 vapor, we would expect to lose ~0.58% of the initial amount of Pt in the sample, more details are provided in the Appendix I Table I.1. This small decrease is below the detection limit of ICP-OES when the powder is aged in a crucible. In a honeycomb monolith, the thickness of the washcoat typically ranges from 50-200 μm while the powder in the ceramic crucible is typically 3-5 mm thick. This difference in the amount of sample per unit of the exposed area makes the total loss of Pt more difficult to measure. The surface of the sample will, however, lose Pt to the gas phase. This is why we studied thin film samples where the amount of Pt emitted is significant enough to be detected via TEM or SEM-EDS. An alternative method for quantifying the emitted Pt is by capturing it downstream and

measuring the ammonia oxidation activity as shown by Leistner et al.[18] This method is sensitive enough to detect Pt emission even when the catalyst temperature is 500˚C.[18]

Figure 3.4 shows TEM images of the initial catalyst and after aging for 30 hours in a ceramic boat. The images of the initial catalysts were presented in Figure 3.2, so these images come from other regions of the sample to provide better statistics. The average Pt particle size in the initial catalyst is less than 1 nm. The TEM particle size distributions (PSD) for Pt/La-Al_2O_3 and Pt/$MgAl_2O_4$ are included in the supporting information and show that the average Pt particle size increases from less than 1 nm in the initial catalyst (Appendix I Figures I.1-I.3) to 30 nm in the aged catalysts (Appendix I Figures I.4-I.6). However, the average diameter derived from TEM images ignores the abnormally large particles which were also seen in these samples. The origin of these abnormally large particles will be discussed in detail in the next section. The presence of a few extremely large particles makes it very difficult to derive an average particle size for Pt in the 30 h aged catalysts. In contrast, the Pt/ceria catalyst does not show any Pt particles in TEM and SEM images of the initial catalyst as well as after aging. The Pt content on this catalyst is unchanged, and the Pt is only visible in AC-STEM images in the form of single atoms (Figure 3.4 d, h).

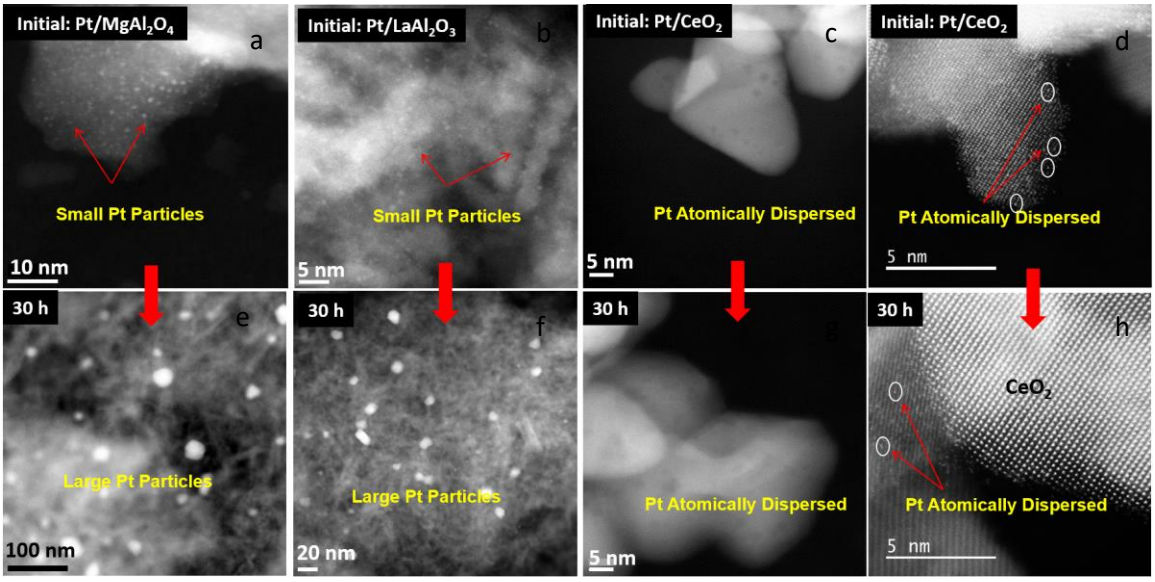

Figure 3.4. *STEM images (a, b, c) of initial catalyst before aging and (e, f, g) after aging at 800 ˚C for 30 h in a crucible boat. AC-STEM images (d, h) of initial and aged catalyst.* for Pt/CeO_2

The SEM images in Figure 3.5 show that the large particles are present after 30-hour aging on the La-Al_2O_3 and $MgAl_2O_4$ supports. These particles are located on the surface of the support, consistent with the re-deposition of Pt that was emitted from within the support pore structure. The large particles range in size from 100 nm to greater than 1000 nm (Figure 3.5 and Appendix Figure I.7), resulting in the sharp peaks seen via X-ray diffraction (Figure 3.6). Steam is present in all exhaust gases from the combustion of hydrocarbons. It is known to accelerate catalyst sintering and deactivation. We also aged our samples in the presence of 10% steam and found that particle growth rates were enhanced. Some of the Pt particles grew larger than 10 microns when the 1wt%Pt/La-Al_2O_3 catalyst was aged at 800 ˚C for 4 hours in the presence of 10% steam (Appendix I Figure I.8). XRD analysis of the same catalyst shows a prominent Pt (111) peak (Appendix I Figure I.9) which yields an average particle size from the analysis of line broadening to be 58.4 nm without steam and

65 nm with steam. As shown in Figure 3.6, no Pt peak is seen via XRD for the Pt/Ceria catalyst. The content of metallic Pt was obtained from the areas of the XRD peaks using whole pattern fitting via the JADE program from MDI. Quantitative analysis of the XRD patterns shows that 0.8 wt% crystalline Pt was present on $Pt/MgAl_2O_4$, $Pt/La\text{-}Al_2O_3$ catalysts (without steam), and $Pt/La\text{-}Al_2O_3$ catalysts (with steam), suggesting that the remaining 0.2 wt% Pt may be in the form of small Pt particles and beyond the detection limit for XRD. The crystallite sizes of Pt reported for $Pt/MgAl_2O_4$, $Pt/La\text{-}Al_2O_3$ (without steam) and $Pt/La\text{-}Al_2O_3$ (with steam) via XRD line broadening analysis were 39 nm, 58 nm, and 65 nm respectively, as shown in Table 3.2. However, since SEM & STEM images show Pt particles range from 10 nm-2 μm in size without steam and up to 10 μm in size with steam, we do not think the XRD line broadening can provide an accurate average particles size since the large particles will yield line width comparable to the instrumental line broadening.

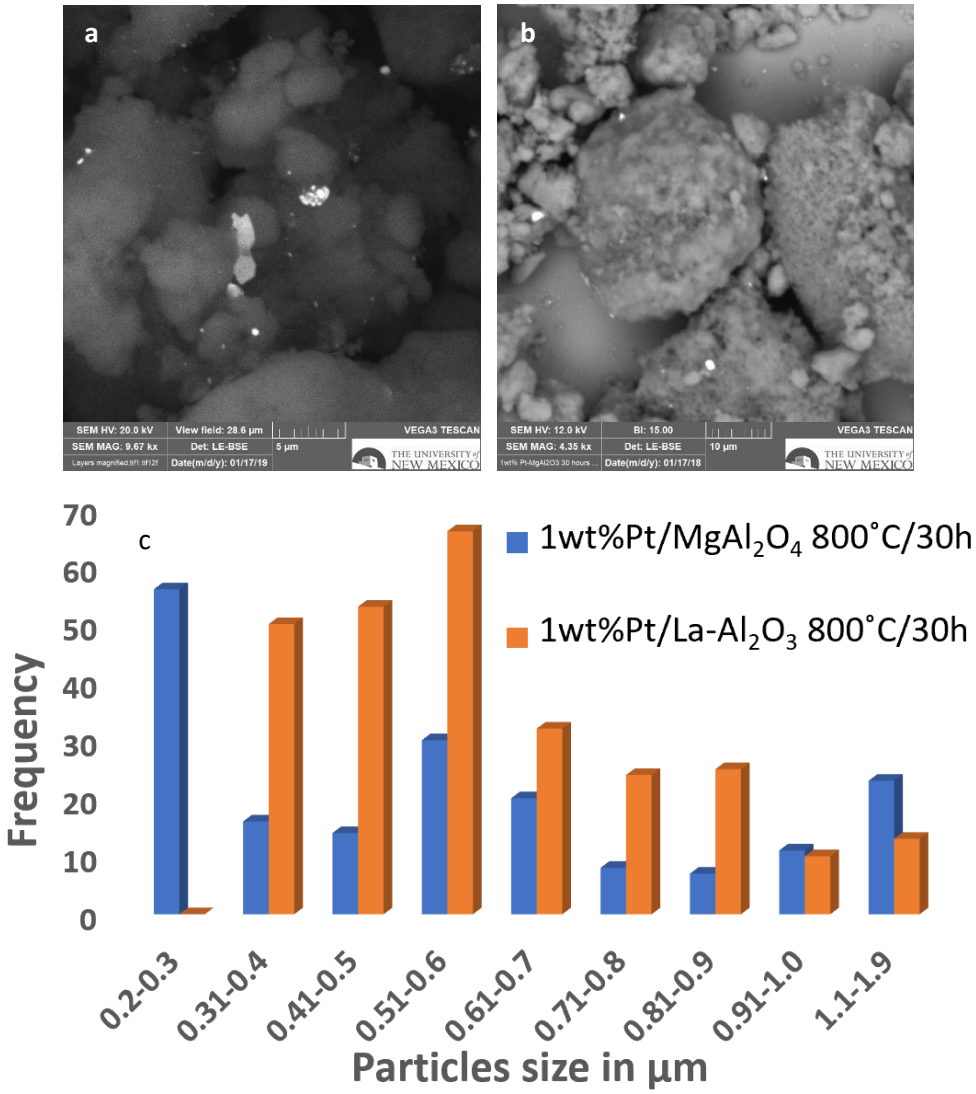

Figure 3.5. *SEM image after aging at 800˚C/30 h a) 1wt%Pt/La-Al_2O_3 b) 1wt%Pt/$MgAl_2O_4$ and c) SEM particle size distribution for 800 ˚C/30 h aged catalysts*

While XRD or TEM cannot provide an average particle size on these supports after aging, CO oxidation helps to show the impact of 800 ˚C aging on catalyst activity. The order of reactivity in the initial catalyst was Pt/La-Al_2O_3 > Pt/$MgAl_2O_4$ > Pt/CeO_2 (Figure 3.7a). Pt/CeO_2 has the lowest CO oxidation reactivity among these three catalysts because it contains ionic Pt which is not reactive for this reaction as shown in previous work.[1,16] Pt/La-

Al_2O_3 showed higher activity than $Pt/MgAl_2O_4$ because it contains smaller Pt particles in its initial state (Appendix I Figure I.3). The dispersion of Pt on La-Al_2O_3 and $MgAl_2O_4$ on the initial catalysts via CO chemisorption was 50.8% and 18.6% respectively. We have included the TOF for these catalysts in the Appendix I information (Table I.2 and Figure I.10) and find these values to be consistent with the literature.[13] We ran three cycles of CO oxidation from room temperature up to 300 ˚C. We reported the third run in the manuscript (Figure 3.7a) but in the supporting information we have included all three runs (Appendix I Figure I.11, I.12, I.13). After aging the catalysts at 800 °C for 30 hours, the order of the reactivity becomes Pt/CeO_2 > $Pt/MgAl_2O_4$ ~ Pt/La-Al_2O_3 ~Pt/ La-Al_2O_3 (10% steam, 800 ˚C/4h). The formation of the large Pt particles explains the lower activity of spinel and alumina-supported catalysts shown in Figure 3.7b and Appendix I Figure I.4, I.5, I.6, I.7, I.8 and I.9.

While there are some differences in the particle size distribution from SEM imaging (Figure 3.5), the surface area of metallic Pt after 30 hours of aging is so low that CO oxidation reactivity is comparable to that of support (Appendix I Figure I.14). In contrast, the reactivity of Pt/CeO_2 was unchanged after 30 hours of aging. There is no agglomeration of Pt atoms to form nanoparticles and a minor decrease in the BET surface area. In our DRIFTS observation performed in situ during CO oxidation, we found that the adsorbed CO was strongly bound. The adsorb CO could not be desorbed in flowing He at 125 ˚C[1] and could not be reacted with flowing oxygen at this temperature. This is the reason for the low reactivity of the as-synthesized Pt/CeO_2 catalyst. When this catalyst was reduced in CO at 275 ˚C it became remarkably active for low-temperature CO oxidation.[19]

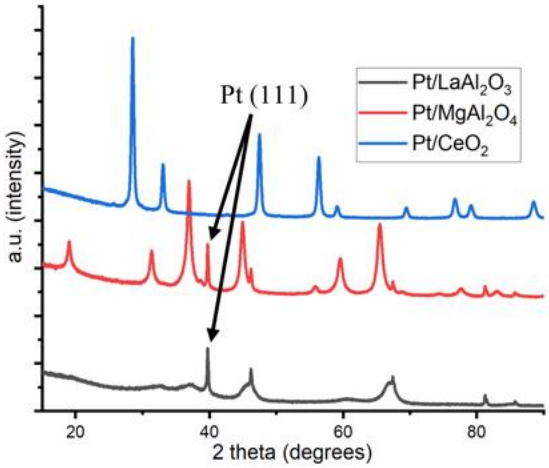

Figure 3.6. *XRD patterns for the catalysts aged at 800 ˚C in air for 30 h in a crucible boat.*

Table 3.2: XRD Characterization of catalyst-scale Pt powder catalysts after aging for 30 h at 800 ˚C. "n.d." indicates not detectable by XRD.

Pt Catalyst Support	Crystalline Pt (wt%)	Pt Crystallite Size (nm)
1 wt% Pt/CeO_2	n.d.	n.d.
1 wt% $Pt/MgAl_2O_4$	0.78	39.4
1 wt% $Pt/La\text{-}Al_2O_3$	0.76	58.4
1wt%$Pt/La\text{-}Al_2O_3$ (steam)	0.81	65

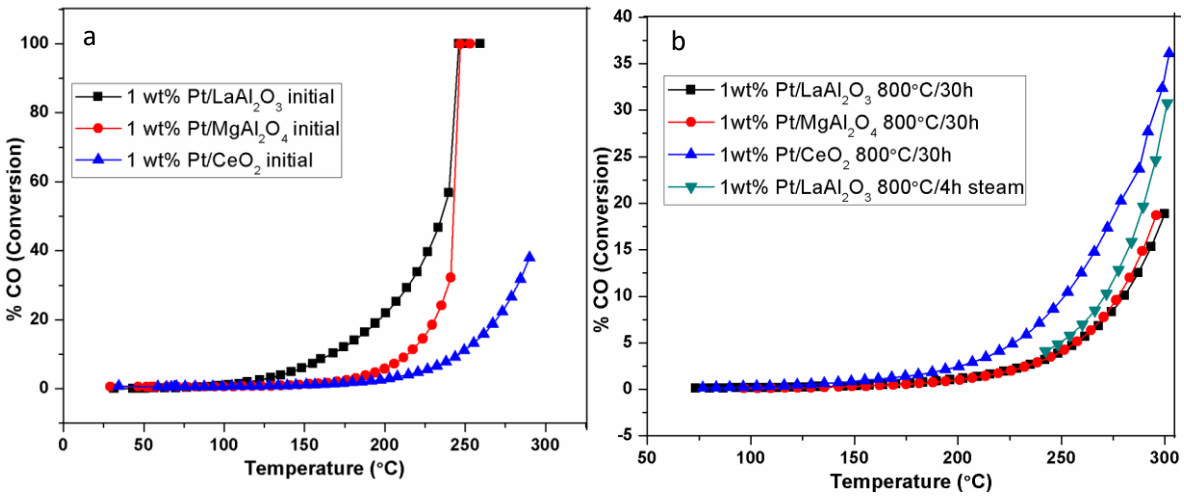

Figure 3.7. *CO oxidation activity for the initial (a) and aged (b) catalysts.*

3.4.3 Mechanism for Anomalous Growth of Pt on La-Al_2O_3 and $MgAl_2O_4$

Figure 3.8 shows a STEM image of the initial catalyst and after aging for 30 h at 800 ˚C in air. The image is consistent with our proposal that Pt present within the pore structure of the support is emitted in the form of PtO_2 vapor and it redeposits on the surface of the catalyst grains leading to the formation of large Pt particles. When the catalyst was aged in the form of a thin film, all of the Pt in the initial catalyst is lost to the vapor phase in a few hours (Figure 3.3). The gas-phase PtO_2 that escapes from the catalyst support is swept away by the flowing gas when the catalyst is present in the form of a thin film. This is confirmed by the total absence of any Pt particles in the 30 hours aged sample (Figure 3.2 e, f). In contrast, when the catalyst is present in the form of a deep bed, we do not see any loss of Pt to the vapor phase. Therefore, the PtO_2 must be redeposited on the support.

Based on DFT calculations, Plessow et al.[20] concluded that gas-phase PtO_2 does not bind to the silica support. In contrast, PtO_2 binds very strongly to step edges of ceria (111) with the heat of adsorption of 7.72 eV, which is greater than the heat of adsorption of PtO_2 on Pt (111) which has been calculated to be 7.32 eV.[21] In our previous work[16], we found that

the calculated adsorption of Pt_4O_6 and $Pt_{10}O_{20}$ was too weak on CeO_2 (111) hence these species would not be stable on the Ceria (111) surface. We concluded that the ability of cerium to change the oxidation state was critical for trapping PtO_2 on the surface. In the case of non-reducible supports such as La-Al_2O_3 and $MgAl_2O_4$, there may be no mechanism to trap PtO_2 coming from the gas phase. Therefore, the only sites that can bind the gas phase PtO_2 species are present on metallic Pt. The binding energy of PtO_2 on Pt (111) is 7.32 eV and Pt (111) step edges are 7.98 eV.[21] Therefore, we can expect that once a metallic Pt has formed it will continue to grow since the support does not provide any opportunities for binding the PtO_2.

Catalyst sintering is known to involve particle migration and coalescence or Ostwald ripening which involves surface diffusion of mobile species. Previous work suggests that these mechanisms may not be able to explain the phenomena observed in this study. For example, in situ High-Pressure X-ray Photoelectron Spectroscopy (HP-XPS) study by Porsgaard et al.[14] found no movement of Pt particles when ~4 nm Pt particles on SiO_2/Si(111) were heated up to 600 ˚C in 0.5 Torr oxygen. Instead, they observed a decrease in the number of particles and their height as measured by Atomic force microscopy (AFM). They concluded that Pt forms volatile species in oxygen at a temperature as low as 450 ˚C leading to a decrease in the amount to Pt on the surface. Simonsen et al.[22] studied a Pt/Al_2O_3 model catalyst when exposed to 10 mbar of oxygen at 650 ˚C via in situ TEM. Time-resolved images unequivocally revealed that the sintering of Pt was mediated by an Ostwald ripening process. They ruled out particle migration and coalescence as the mechanism for sintering. Due to the low pressure used in their study and the absence of a flow of gas over the surface, they did not detect any loss of Pt to the

vapor phase. On the other hand, the HP-XPS involves a jet of gas impinging on the sample which Porsgaard et al.[14] felt caused the emission of Pt species. Likewise, in our experiment, the flowing air sweeps away the PtO_2 emitted from the thin film model catalysts. When the sample is present in the form of a packed bed or loaded on to the ceramic crucible, the PtO_2 vapor cannot escape from the sample but tends to re-deposit. Oxide surfaces such as silica or ceria (111) do not bind the PtO_2 strongly as demonstrated by DFT calculations.[14,16,21] Therefore, at the aging temperature of 800˚C the PtO_2 will not adsorb on oxide surfaces. Only metallic Pt particles that are formed will serve as adsorption sites for the PtO_2 vapor leading to the growth of anomalously large particles.

The anomalous growth of Pt particles under these conditions is a result of the vapor phase transport.[20] This explains why abnormally large Pt particles are seen (Figure 3.8). Furthermore, these large particles appear to be located on the surface of the individual catalyst support particles/grains and not inside the pores, because transport of gas-phase PtO_2 would be facile in the inter-particle space between catalyst grains. In a previous study of Pd sintering where the transport was exclusively through surface diffusion, and found that anomalously large particles were only seen on the perimeter of a cluster of smaller particles.[23] We conclude that an essential ingredient for abnormal particle growth must involve facile transport to the growing particle which does not happen within the pore structure of the support.

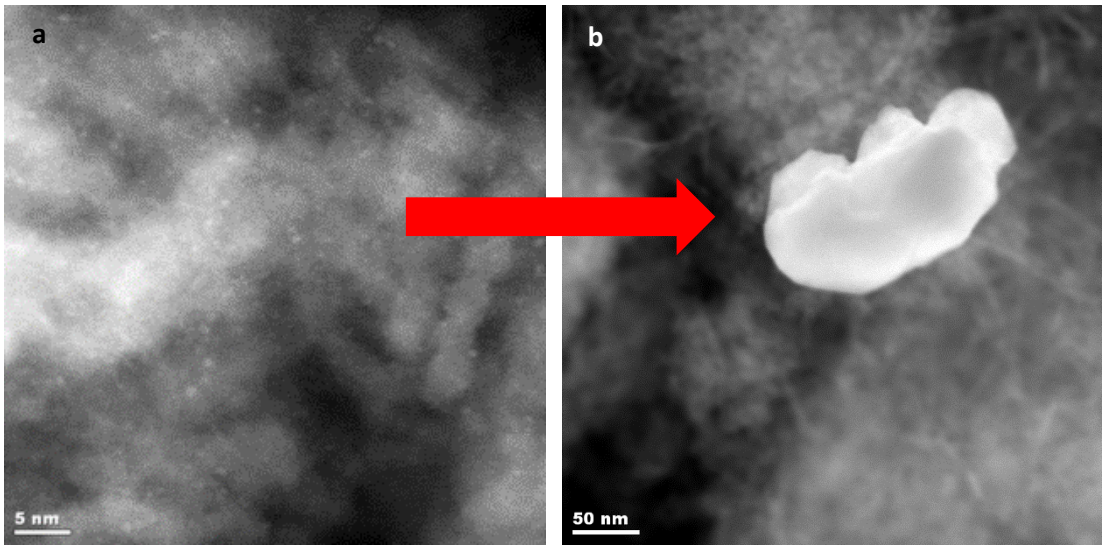

Figure 3.8. *STEM image of (a) initial Pt/La-Al_2O_3 and b) aged 800˚C/30 h. The small particles in the initial catalysts transformed into gas phase PtO_2 which condensed into abnormally large Pt particles.*

It was reported by Li et al.[12] that Pt particles are stabilized on Pt/$MgAl_2O_4$ in contrast to Pt on commercial Al_2O_3. In this work, however, we do not find any difference between these two supports. The loss of Pt to the vapor phase is equally rapid (Figure 3.3) and large particles are found after aging at 800 °C on both supports (Figure 3.5) and they show similar CO oxidation reactivity after 30 h aging at 800 °C in the air (Figure 3.7b). The reactivity of Pt/La-Al_2O_3 aged at 800 ˚C without and with steam is almost the same as shown in Figure 3.7b and Appendix I Figure I.9b, suggesting the formation of anomalously large Pt particles and their contributions to the oxidation reaction is negligible when compared to the support activity (Appendix I Figure I.14). It

is clear that the large particles were non-existent initially, and the rates of mass transfer for Pt are rapid enough for the formation of large particles seen in these catalysts. Earlier reports indicating the growth of Pt particles via vapor-phase transport of PtO_2 on supported

catalysts[4,20,24] are consistent with our observations. The stochastic nature of nucleation and the limited number of nucleation sites for Pt particles help explain why the few particles that are formed continue to grow, fed by the presence of PtO_2 vapor, leading to abnormally large Pt particles when aged at 800 °C in air.

3.5 Conclusions

We observed a loss of Pt from Pt/La-Al_2O_3 and Pt/$MgAl_2O_4$ when the catalyst was present in the form of a thin film. The loss of Pt is attributed to the formation of volatile species PtO_2 via the reaction of Pt with oxygen at elevated temperatures. STEM images of initial catalysts Pt/$MgAl_2O_4$ and Pt/La-Al_2O_3 show small and homogenously distributed nanometer Pt particles. After aging the catalyst in the form of a thin film, all the Pt is lost because it is swept away by the flowing air. No loss of Pt is seen from Pt/CeO_2 because the Pt is present as Pt^{2+} bound to four oxygen atoms. Similar measurements were carried out with the powder catalyst placed in a ceramic crucible boat. With this geometry, there was no loss of Pt because the gas-phase PtO_2 condensed within the bed to form large Pt particles. Due to the inability of PtO_2 to bind strongly to $MgAl_2O_4$ and La-Al_2O_3, metallic platinum provides the only strong binding sites to capture gas-phase PtO_2. This leads to the growth of a few particles that continue to grow, fed by the high vapor-phase concentration of PtO_2. This work shows the importance of vapor-phase transport for the observed anomalous growth patterns. Our work was directed towards understanding phenomena that occur under lean accelerated diesel catalyst aging conditions, such as those specified by the USDRIVE Low-Temperature after treatment (LTAT) test protocol.[2] We have previously demonstrated, as have other researchers, that under reducing conditions atomically dispersed Pt transforms into nanoparticles.[19] The transformation from

nanoparticles into atomically dispersed Pt is reversible on ceria support as shown by Ganzler et al.[25] Therefore, the results presented here are also relevant to Pt/CeO_2 subjected to reducing conditions.

CHAPTER 4: STABILIZING HIGH METAL LOADINGS OF THERMALLY STABLE PLATINUM SINGLE ATOMS ON AN INDUSTRIAL CATALYST SUPPORT

This work has been published in the ACS catalysis journal.

4.1 Introduction

Single-atom catalysts[26] represent a new frontier in heterogeneous catalysis because of improved atom efficiency, higher reactivity, and improved selectivity for a range of catalytic reactions.[27,28,29,30] However, isolated atoms become mobile at elevated temperatures, causing agglomeration into nanoparticles.[31] Hence, low surface concentrations are generally used since it is often energetically favorable to form dimers, trimers, or larger clusters with increasing metal loading. For example, Qiao et al.[27] observed exclusively single-atom species on a 0.17 wt % Pt/FeOx but Pt rafts and small clusters in their 2.5 wt % Pt/FeOx sample. To preserve isolated atoms, DeRita et al.[28] used only 1 Pt atom per TiO_2 support particle (0.05 wt% Pt). Two recent reviews pointed out the need to achieve high metal loadings as a significant challenge.[32,33] Recent work on non-oxide supports[34,35,36] has demonstrated the ability to generate high metal loadings of single atoms, but stabilizing single atoms of platinum group metals on oxide supports remains a challenge.

We work on ceria because this support is unique in that atomically dispersed Pt species can be formed simply by treating the catalyst at high temperatures in flowing air.[1] In our previous work, we physically mixed a Pt/alumina sample with ceria to form atomically dispersed Pt.[1] However, a similar result was also achieved by depositing the Pt precursor on the support via impregnation.[37] This method of synthesis (atom trapping) represents a facile approach to prepare single-atom catalysts.[38] The focus of this report is on

understanding how single-atom catalysts could be prepared using readily available commercial precursors and supports and exploring the upper limit for depositing stable single atoms of Pt.

When Pt metal is heated to high temperatures in the presence of oxygen, volatile PtO_2 is formed.[5] Due to the weak interaction with supports such as silica,[20] the PtO_2 condenses forming large particles. The interaction with ceria (111) terraces is also weak, but 4-fold sites on CeO_2 (100) pockets were identified by Bruix et al.[39] as strong binding sites for Pt ions. Using a model CeO_2 cluster, it was demonstrated via density functional theory (DFT) calculations that the deposited Pt atoms were oxidized to form Pt^{2+} leading to a corresponding reduction of two Ce^{4+} cations to form Ce^{3+}.[39] In our previous work,[1] we found that polyhedral ceria and nanorods were very effective at binding Pt and stopping sintering, but ceria cubes which expose (100) facets were not very stable when heated at elevated temperatures.[1] The ceria (111) facet is the dominant exposed surface in powder samples; however, this surface does not provide 4-fold sites for binding Pt. Dvorak et al.[17] used STM on model ceria CeO_2 (111) surfaces to identify sites where Pt single atoms could be strongly bound. They concluded that step sites could achieve 4-fold coordination and lead to stable Pt^{2+} species. Here we explore whether similar surface sites can also exist on high-surface-area ceria powders.

By using thermally stable commercial ceria powders, we demonstrate here that high (3 wt %) loading of Pt can be stabilized exclusively in the form of isolated single atoms without forming any clusters or aggregates. Only after exceeding the saturation capacity of this ceria support do we detect metallic Pt particles. The nature of the Pt species was studied using surface-sensitive probes such as Low Energy Ion Scattering (LEIS) and X-ray

Photoelectron Spectroscopy (XPS) and the coordination to the support was studied using Extended X-ray Absorption Fine Structure (EXAFS) measurements and Density functional theory (DFT) calculations. Aberration Corrected-Scanning Transmission Electron Microscopy (AC-STEM) provides unambiguous evidence of the exclusive presence of atomically dispersed Pt, and this is also confirmed by Diffuse Reflectance Infrared Fourier Transform Spectroscopy (DRIFTS) and CO oxidation reactivity. These results are supported by DFT calculations. We conclude that the stability of Pt single atoms is a result of a reaction between the mobile PtO_2 and under-coordinated Ce^{3+} sites on the catalyst support as shown in Scheme 4.1.

Scheme 4.1. Mobile Pt Species Provide the Oxygen Needed to Bind to Under-Coordinated Ce^{3+} Sites at Step Edges.

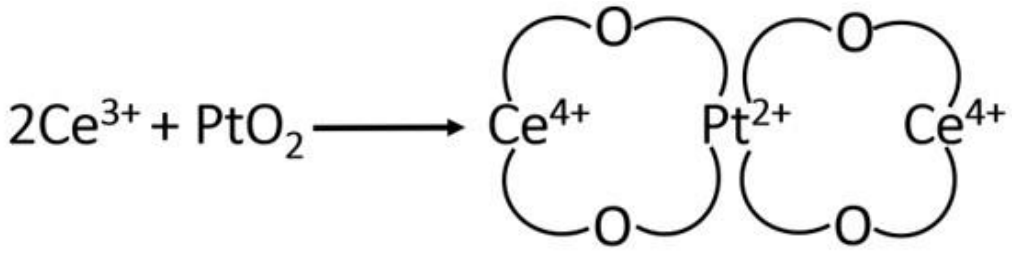

Scheme 4.1. *Mobile Pt species provide the oxygen needed to bind to under-coordinated Ce^{3+} sites at step edges. Sharing of oxygen atoms derived from PtO_2 helps to form covalent bonds with single atoms of Pt^{2+} leading to the stability of the single-atom species. The four-fold sites are provided at (111) step edges, which are plentiful on ceria powder samples. The synthesis at elevated temperatures in the air ensures that the ceria surface is free of any adsorbates, allowing the facile reaction of Pt with the support.*

The ease of reduction of Ce^{4+} to Ce^{3+} and the formation of oxygen vacancies in ceria supports is well-known[40] and utilized for automotive exhaust catalysts for oxygen storage.[11] However, our method of synthesis involves heating the sample to 800 °C in flowing air, a temperature at which we would expect to see only a low concentration of oxygen vacancies. As we show here, all polyhedral ceria particles possess surface steps, and these represent sites where we can find undercoordinated Ce^{3+} cations which are capable of reacting with the mobile PtO_2 species. In Scheme 4.1, the Pt brings with it the oxygen atoms that are shared with the Ce^{3+} transforming it to Ce^{4+} while forming a covalent bond with the support. The method of synthesis is fundamentally different from conventional aqueous impregnation,[41] where a sheath of hydroxyls prevents the formation of direct bonds to the support. Scheme 4.1 helps explain the strong binding of Pt to the support, which is essential for the formation of thermally stable single atoms.

The results presented here shed light on an important attribute of ceria supports, the ability to slow the sintering of Pt. The sinter-resistance of ceria supports has been previously explained in terms of its ability to lower the free energy of metal nanoparticles[42] and thereby lowering the driving force for sintering. Here we show that it is the trapping of mobile Pt species that might also be important for understanding why ceria is so effective at preventing catalyst sintering. Catalyst regeneration and the burning of coke deposits always involve high-temperature calcination. Hence, the insights gained from understanding surface sites that help to trap mobile Pt species on industrial catalyst support will be of broad interest to the field of heterogeneous catalysis.

4.2 Experimental Details

We used tetraamine platinum nitrate ($Pt(NH_3)_4(NO_3)_2$) obtained from Sigma Aldrich as the Pt precursor and it was deposited on high surface area ceria powder (obtained from Solvay, grade HSA 5) using incipient wet impregnation. We prepared samples containing 1, 2, 3, and 4 wt% of Pt/ceria. The pore volume of ceria (0.6 ml/g) was determined by first wetting the dry ceria powder with water. The impregnation of the platinum precursor was done to fill the pores of ceria. The tetraamine platinum nitrate solution was loaded on ceria in multiple aliquots and dried at 110 °C for 4 hours until all the water evaporated in the air after each impregnation. The samples were then calcined in a tube furnace with 100 ml/min of air for 10h in the air at 800 °C. The furnace temperature was ramped up at 1°C per minute.

The Pt loading was determined by Inductive Coupled Plasma-Optical Emission Spectroscopy (ICP-OES), via electron probe microanalysis as well as Transmission Electron Microscopy-Energy Dispersive Spectroscopy (TEM-EDS). For the TEM analysis, a small amount of the powder sample was put in an agate mortar and ground with ethanol to create a suspension. A drop of this suspension was deposited on a 3 mm holey carbon grid. Transmission electron microscopy (TEM) was performed using a JEOL 2010F microscope operated at 200 kV with a Schottky FEG emitter. The analysis was performed on 10 regions of the sample, the average composition was reported. Some of the samples were also analyzed via Scanning Electron Microscopy (SEM) using a Hitachi S-5200 operated at 2 kV. For Energy Dispersive Spectroscopic (EDS) analysis we used an Oxford Aztec system, with the microscope operated at 10 kV. AC-STEM images were obtained using a JEOL NeoARM equipped with a cold field emitter and the UHR polepiece

(resolution 0.07 nm). X-Ray Diffraction (XRD) was performed using the Rigaku Smartlab instrument operated at 40 kV and 40 mA equipped with a D/teX 1-D detector and a sealed tube Cu target X-ray source (40 kV and 40 mA). Data was collected at 6 degrees/min with a 0.02-degree step. The XRD patterns were analyzed using the whole pattern, Rietveld analysis, using the MDI Jade software package. Brunauer, Emmett, and Teller (BET) surface area measurements were performed on a Micromeritics Gemini 2360 multipoint analyzer using N_2 adsorption at -196 ˚C.

CO oxidation was chosen as a probe reaction. The reaction rate measurements were performed using ¼ inch diameter U-tube with 20 mg of sample. The gas flow rates for CO oxidation were: CO 1.5ml/min, O_2 1ml/min, and He 75ml/min, and the temperature ramp rate was at 2°C/min. The as-prepared, air-exposed catalyst was loaded into the reactor (or the DRIFTS cell) and the temperature was increased to 300°C under He. Once at 300°C, pretreatment with 10% O_2 was performed for 30 min. The gas was switched to He, the catalyst cooled to the reaction temperature and CO oxidation measurements were performed. The total pressure during CO oxidation was 83.3 kPa, the atmospheric pressure in Albuquerque. The products were analyzed by an Agilent Micro GC. For obtaining Arrhenius plots, the measurements were performed isothermally at low conversions, using a similar reaction set up. In separate experiments, the catalyst surface during CO oxidation reaction was monitored using DRIFTS and Mass Spectrometry (MS). The infrared spectrometer used was a Tensor 27 from Bruker, coupled with a Praying Mantis™ Diffuse Reflection Accessory from Harrick. The MS used was a ThermoStar GSD 320 T Quadropole Mass Spectrometer (QMS) from Pfeiffer Vacuum, using a Secondary Electron

Multiplier (SEM). DRIFTS was performed using a Harrick cell which allowed treatment of samples in-situ.

LEIS was used to quantify the concentration of Pt atoms on the surface. This technique[43] can selectively detect the topmost atoms, thus unlike XPS which probes deeper into a sample. The experiments were carried out using an IONTOF $Qtac_{100}$ instrument which is a dedicated LEIS instrument equipped with a double toroidal analyzer for the energy analysis of the backscattered ions. The analyzer has a large solid angle of acceptance (full 360˚azimuth), while the scattering angle is fixed at 145˚. This gives, in combination with parallel energy detection, a high sensitivity while maintaining the mass resolution. We used He^+ as well as Ne^+ with ion energy 3 keV and 5 keV and current 5 and 2 nA respectively to analyze the surface concentration of Pt^{2+} ions in the Pt/CeO_2 catalysts. The area scanned per sample by these two ions was 2×2 mm^2 and the ion influence given to the samples was 1.4×10^{14} ions/cm^2 and 2.8×10^{13} ions/cm^2 respectively. The spectra for the Pt reference were analyzed within a 1.5×1.5 mm^2 sputter crater over an area of 1×1 mm^2. The analysis time was adjusted such that the surface damage was the same as for the other spectra. Assuming a sputter coefficient of 0.1 for He and 1 for Ne, this will lead to surface damage of 1% and 2% at the end of the analysis. XPS was performed using a Kratos Axis Ultra photoelectron spectrometer equipped with a monochromatic Al Kα source operating at 300 W. The base pressure was 2.7×10^{-8} Pa, and the operating pressure was 2.7×10^{-7} Pa. XPS was performed in order to study the chemical state of the Pt catalyst. Analysis of the XPS spectra was performed using CASA XPS software.

X-ray absorption spectroscopy (XAS) was performed at the 10 ID beamline at the Advanced Photon Source (APS) at Argonne National Laboratory. Air exposed samples,

as-prepared after 800 ˚C calcination were used for the analysis. Samples for XAS analysis were ground into a fine powder and mixed with a 50/50 mixture of boron nitride/PVPP. The mixture was then pressed into a 7 mm pellet for analysis. Samples were measured in fluorescence mode using a Lytle detector with Soller slits and a Zn foil filter. A platinum foil was measured concurrently in transmission mode as an energy reference. Data analysis was performed using WinXAS 3.1 software.[44] Phase and amplitude functions for the fitting of Pt EXAFS data were extracted from experimental references. Pt-Pt scattering phase and amplitude were extracted from platinum foil (12 neighbors, 2.77 Å). Pt-O scattering phase and amplitude were extracted from $Na_2Pt(OH)_6$ (6 neighbors, 2.05 angstroms). Fourier transforms were taken over a k range of 3-12.5. Fits in R space for oxide only samples were done over a range of 1.0-2.0 angstroms. For samples with metallic scattering, the fit range was over 1.0-3.2 angstroms. Fits were performed on isolated first shell scattering in R space. R space fitting was accomplished by fixing the Debye-Waller factor and allowing the bond distance, coordination number, and E^0 to vary. After a satisfactory fit was obtained, the Debye-Waller factor and was adjusted while allowing the coordination number to vary to obtain the best fit on isolated first shell scattering k space data.

4.2.1 Computational Details

All spin-polarized DFT calculations were carried out with the Vienna Ab initio Simulation Package (VASP)[45,46] with the PW91 functional.[47] The electronic wave functions were expanded in plane waves up to cutoff energy of 400 eV and the ionic core electrons were approximated by the projector augmented-wave (PAW) method.[48] To describe properly the

behavior of electrons in f orbitals of Ce in CeO_2, the DFT + U method with U = 4.5 eV was used.[49]

For studying oxidized Pt clusters, an O-terminated slab of CeO_2 (111) with a six atomic layer unit cell of a=13.33 Å and b=15.39 Å including 32 Ce and 64 O atoms were employed. For studying the migration of the PtO_2 species on CeO_2 (111), a smaller six atomic-layer unit cell of 7.65×13.25 $Å^2$ with 16 Ce and 32 O atoms was adopted. The calculated CeO_2 lattice parameter of 5.44 Å was consistent with the previously reported experimental and theoretical values.[50,51] In our calculations, the top three atomic layers and the adsorbates were allowed to relax while the bottom three atomic layers were fixed. 1×1×1 and 2×1×1 k-point meshes were adopted to sample the Brillouin zone for the model of oxidized Pt clusters and PtO_2 species on CeO_2 (111), respectively, which was tested to be converged.

The step-edge model used in this work was similar to those reported in previous theoretical studies[17,52] of Pt interaction with CeO_2 surfaces, specifically the Step-II and Step-U Models used. A step was constructed by adding three additional atomic layers (2 O layers and 1 Ce layer) on the 7.65×13.25 $Å^2$ CeO_2 (111) slab with six atomic layers. Thus, the model step consists of nine atomic Ce/O layers with 20 Ce and 40 O atoms. During the structural optimization, the atomic positions of the lowest three CeO_2 atomic layers were constrained while the other layers as well as the adsorbates were fully relaxed. The k-point mesh was set to be 2×1×1. A vacuum space of 14 Å or larger was employed between the neighboring interleaved slabs for all the surface models.

The adsorption energy of a pertinent species was computed as follows: Eads = E(adsorbate + surface) – E(free molecule) – E(free surface). A transition state (TS) between an initial

state (IS) and final state (FS) was determined using the climbing image nudged elastic band (CI-NEB) method.[51] The total energy difference was less than 10^{-4} eV and the convergence of relaxation was checked with the 0.05 eV/Å criterion.

4.3 Results & Discussion

4.3.1 Upper Limit for Loading Atomically Dispersed Pt

To explore the upper limit for loading single atoms of Pt on ceria, we prepared catalysts ranging from 1 - 4 wt% Pt using a thermally stable high surface area commercial ceria (Solvay grade HS 5). After the deposition of Pt, the samples were treated in flowing air at 800 °C for 10 h. As shown in Figure 4.1a, no Pt peak is seen via X-ray diffraction (XRD) on the 3 wt% sample indicating that the Pt is atomically dispersed, but the 4 wt% Pt sample shows a well-defined Pt (111) reflection at 39.7˚. The presence of large Pt particles is also confirmed via SEM, Figure 4.1b, indicating that the saturation coverage of atomically dispersed Pt has been exceeded in the 4 wt% Pt/ceria sample. The formation of metallic Pt during 800 °C treatment in the air may seem surprising. It is known that volatile PtO_2 is formed when Pt is heated in air[3], but as we show later in section 3.3, this PtO_2 does not nucleate on ceria because small clusters of Pt oxide are not stable at this temperature. Instead, large Pt particles are formed when Pt catalysts are aged in air[8] because the PtO_2 can adsorb on the step edges of metallic Pt particles.[21] As shown in this work, ceria has the remarkable ability to trap this volatile Pt at atomic dispersion at concentrations up to 3 wt%, preventing the formation of metallic Pt particles.

The as-prepared samples were analyzed via X-ray photoelectron spectroscopy (XPS) to determine the concentration of Pt and its oxidation state. The quantification of the peaks and details of the Ce 3d and Pt 4f regions is presented in Appendix II (Figure II.1-II.2 and

Table II.1). XPS analysis of the 3 wt% Pt sample (Figure 4.1c) shows that the Pt is present in an oxidized form primarily in the Pt^{2+} oxidation state (72.5 eV) with a very small contribution from Pt^{4+} (74.5 eV). The relative contribution from the Pt^{4+} peak decreases from 12.2 % in the 1 wt% sample to 5.1 % in the 3 wt% sample (Appendix II, Figure II.1, and Table II.1). The 4 wt% Pt sample is very different (Figure 4.1d, II.2, and Table II.3) and shows a prominent metallic Pt peak at 70.6 eV. A linear relationship between the XPS determined Pt/Ce ratio and the bulk Pt loading is indicative of atomic dispersion of the Pt since the ceria particle size and the BET surface areas of these samples are very similar. Above the saturation capacity of ceria (4 wt% Pt), we see a bimodal distribution: Pt single atoms (as inferred from XPS, Figure 4.1c and 4.1d) coexisting with Pt particles that are typical ~100 nm or larger. No small Pt clusters are visible in the HRTEM image (Appendix II, Figure II.3) and via HAADF-STEM (Appendix II, Figure II.4).

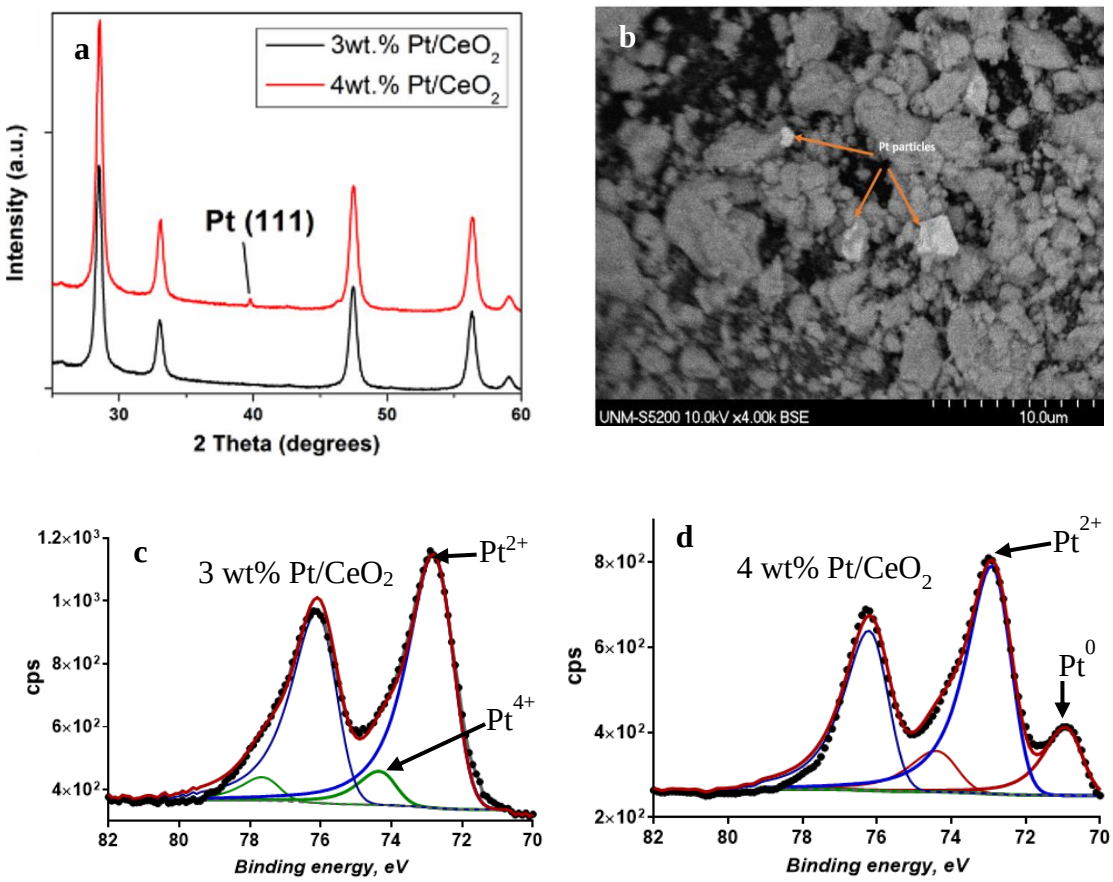

Figure 4.1. *Characterization of catalysts after aging at 800 °C in air for 10 h (a) XRD shows no metallic Pt diffraction peaks for the 3 wt% Pt sample but a well-defined metallic Pt (111) peak in the 4 wt% sample (b) SEM image showing the presence of large Pt particles in the 4 wt% Pt/CeO₂ (c) XPS analysis of the 3 wt% sample showing that the Pt is primarily in the 2+ oxidation state (d) 4 wt% Pt sample shows the presence of metallic Pt coexisting with the ionic Pt.*

4.3.2 Nature of Atomically Dispersed Pt

The nature of the Pt species on ceria was determined via electron microscopy. In the 4wt% Pt/CeO_2 sample, the large Pt particles (usually ~100 nm or larger) can be seen via SEM (Figure. 4.1b) and their presence is evident in the XRD and XPS data (Figure. 4.1a and 4.1d). The presence of atomically dispersed Pt is evident from the Pt^{2+} peak via XPS, but

it is difficult to image with a conventional TEM/STEM (JEOL 2010F) in HAADF images which are shown in Appendix II, Figure II.3. When regions that do not contain large particles are analyzed via EDS (Appendix II, Figure II.4), the amount of atomically dispersed Pt can also be quantified. The concentration of crystalline Pt (large particles) can be quantified via XRD, as shown in Appendix II, Figure II.5. The high-temperature synthesis of these samples (800 °C in the air) yields either atomically dispersed Pt or large Pt particles. There are no other species in the sample. Hence, by performing TEM-EDS analysis of regions of the sample that do not contain any metallic Pt particles (as shown in Appendix II, Figure II.3, and II.4), we obtain a direct measure of atomically dispersed Pt. The sum of Pt detected via XRD (Appendix II, Figure II.5) and via TEM-EDS adds up to the total Pt content, allowing us to complete the mass balance for Pt, as shown later in Table 4.1. Direct evidence for the presence of Pt single atoms is obtained via aberration-corrected scanning transmission electron microscopy (AC-STEM) using the JEOL NeoARM microscope.

The AC-STEM images of the 3 wt% Pt/ceria in Figure 4.2a-d are replete with white dots, most of which come from Ce atom columns. When the Ce atoms are lined up along the viewing direction (see particle A in Figure 4.2a), strong channeling contrast from Ce cations makes it very difficult to discern the isolated Pt atoms. Particle B in Figure 4.2a is oriented off the zone axis with faint lattice contrast from the ceria support. The bright dots that stand out against the background of the ceria support indicate the presence of isolated Pt atoms. The boxed region in Figure 4.2a shows bright dots corresponding to the Pt atoms lined up with the underlying ceria (200) lattice planes. In this boxed region, we counted 25 atoms (see Appendix II, Figure II.6) in an area of 25 nm^2 which indicates a surface

concentration of 1 atom Pt/nm^2 which is in excellent agreement with estimates from bulk elemental analysis and BET surface area measurement and LEIS as shown later in this manuscript. The AC-STEM images also show that these polyhedral ceria particles expose (111) facets with surface steps, indicated by arrows on Figures 4.2a, b, and c. Figure 4.2d shows that at high metal loading, the Pt atoms can exist in close proximity. The overlap between such closely spaced atoms in the viewing direction could cause shadowing and explain the lower apparent surface coverage by LEIS for the higher loading samples when compared with other techniques.

The surface concentration of Pt was independently measured using low energy ion scattering (LEIS), a technique that can selectively analyze surface atoms of the sample. In this method[43], the sample is exposed to ions of known kinetic energy. The backscattered ions result from elastic collisions with the topmost atoms on the surface. The energy of the backscattered ions, which is dependent on the mass of the scattering partner, enables the identification of the surface atoms. In this work, 3 keV $4He^+$ ions and 5 keV $20Ne^+$ ions were used (Appendix II, Figure II.7). With $4He^+$ ions, there was overlap between the Pt and Ce signals, but with the heavier $20Ne^+$ ions, the peaks of Ce and Pt were well resolved to allow quantification of the surface signal (Figure 4.3a). The method of calculation is described in Appendix II (Tables II.3 and II.4).

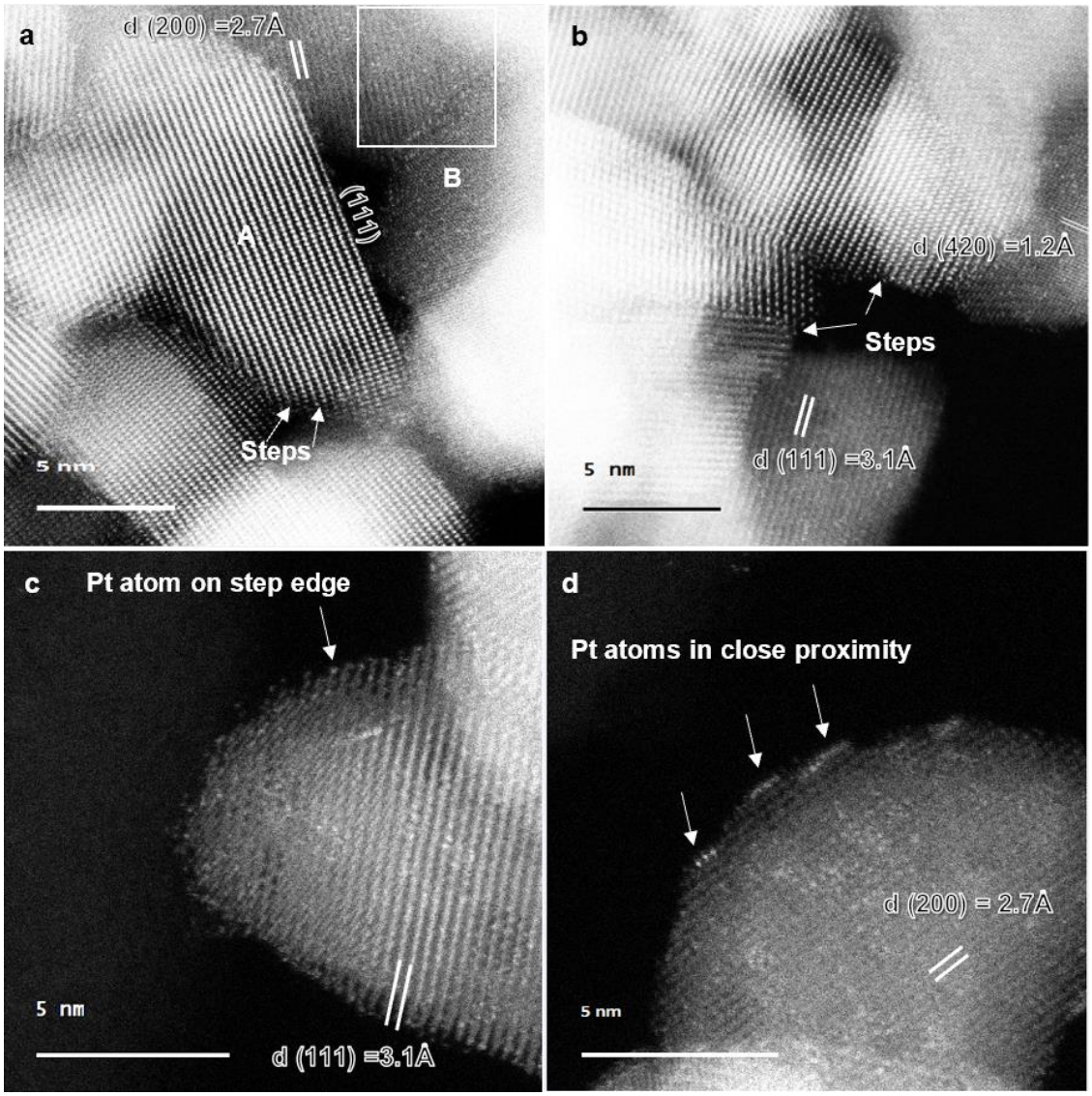

Figure 4.2. *(a-d) AC-STEM images of 3 wt% Pt/ceria. Particle A oriented along [112] with strong contrast from the Ce atom columns while particle B is oriented off the zone axis making it easier to detect the Pt single atoms. Pt atoms appear bright compared to the contrast of the support. Surface steps are a common feature and Pt can be seen to decorate the step edge in (c) and Pt atoms are found in close proximity in (d).*

Since samples containing 1 – 3 wt% Pt only show single-atom Pt species and no metallic Pt, we can calculate the surface concentration of atomically dispersed Pt from the measured BET surface areas and the bulk elemental analysis (Table 4.1). The ceria as-received has a surface area of 130 m^2/g but after heating the ceria at 800˚C for 10 hours its surface area drops to 60 m^2/g. Loading the Pt on ceria and aging at 800˚C for 10 hours under flowing air helps to maintain the high surface area. This synergistic effect of trapped Pt on preserving the surface area of ceria was also mentioned in our previous work.[1]

For the 4 wt% Pt sample, due to the co-existence of metallic Pt and single atom species, we analyzed regions devoid of metallic Pt particles via TEM-EDS and determined the saturation loading of single-atom Pt species to be ~3.2 wt% (Appendix II, Figure II.4). The amount of Pt giving rise to the XRD peaks was also quantified by whole pattern fitting (Appendix II, Figure II.5, and Table II.2) allowing us to complete the mass balance for the Pt species. This combination of XRD and TEM-EDS analysis allows the determination of the upper limit for atomically dispersed Pt in this sample to be ~1 atom/nm^2 (Table 4.1).

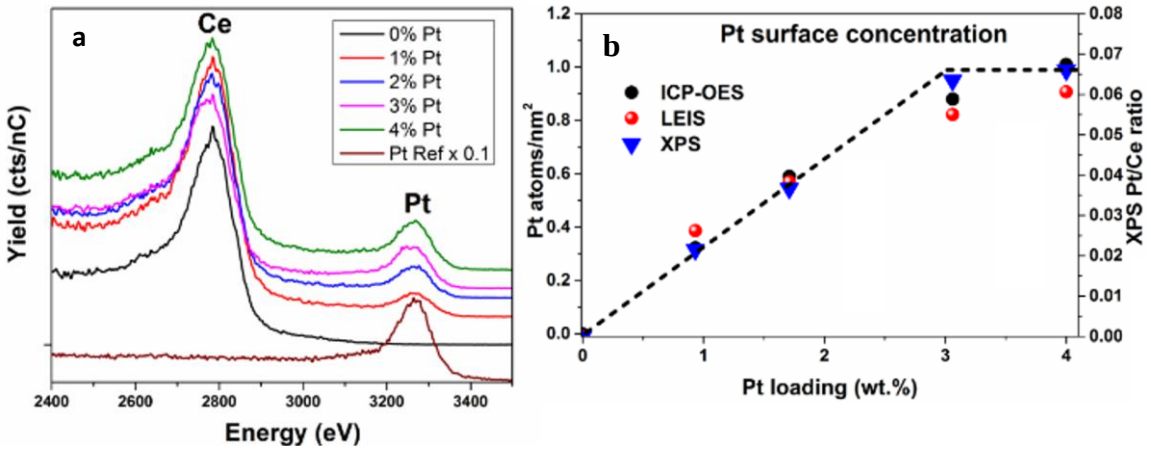

Figure 4.3 *(a) 5 keV 20Ne$^+$ LEIS spectra for the samples after O atom treatment, compared to a sputter cleaned Pt foil (scaled 0.1x) and (b) A plot showing surface concentration of*

Pt derived from bulk elemental analysis and LEIS (left axis) and XPS Pt/Ce ratio (right axis) as a function of metal loading. At 4 wt% Pt the sample shows the co-existence of metallic Pt and atomically dispersed Pt.

Table 4.1. The surface concentration of Pt determined by TEM-EDS, LEIS, and XPS

Catalyst nominal wt%	BET surface area (m^2/g)	ICP-OES analysis	Atoms of Pt/nm^2 calculated	$Atoms/nm^2$ from LEIS	Pt/Ce ratio from XPS
Blank CeO_2	130	-	-	-	-
1 wt% Pt/CeO_2	90	0.932	0.32	0.37	0.022
2 wt% Pt/CeO_2	90	1.71	0.59	0.54	0.037
3 wt% Pt/CeO_2	95	3.06	0.99	0.77	0.063
4 wt% Pt/CeO_2	101	4	1.01*	0.85	0.066

*The 4 wt% Pt/ceria sample contains 0.8 wt% of metallic Pt and 3.2 wt% of atomically dispersed Pt, the latter value was used to calculate the surface concentration of single atoms of Pt.

The agreement between the surface concentrations calculated via bulk elemental analysis and BET surface area and LEIS is remarkably good (Table 4.1), especially since LEIS provides a direct measure of surface concentration without any normalization. The surface-

sensitive detection of Pt in these samples via ion scattering confirms that it is located on the surface, and not buried, or doped into the ceria. For the 3 wt% and especially 4 wt% samples, there is a small, but clear, signal reduction (23 and 30% respectively) of the surface Pt detected via LEIS compared with the value determined by bulk elemental analysis and via XPS suggesting the beginning of clustering or some shadowing of the Pt by the support. This is consistent with the electron microscopy results (Figure. 4.2d), which indicate that Pt atoms are in close proximity at such high metal loadings.

The nature of the Pt species was studied via XAS, which provides information on the oxidation state of Pt and the bond distances to the neighboring atoms. Figure 4.4a shows the X-ray absorption near edge structure (XANES) spectra of several Pt reference compounds and the Pt/ceria samples in the as-prepared, air-exposed state. The XANES edge energy of the 2 wt% and 3 wt% Pt sample matches that of Pt^{2+} acetylacetonate (Table 4.2). The white line intensity (Figure 4.4a) of Pt/ceria is slightly higher than Pt^{2+} acetylacetonate but not as large as $Na_2Pt(OH)_6$. XPS results indicate that platinum is present in the +2 state, which rules out changes in the XANES due to the oxidation state. Thus, the higher inflection point energy and white line intensity can be attributed to platinum in the catalyst having more oxygen neighbors than $Pt(acac)_2$. The magnitude of the Fourier transform of these catalysts is exactly 16% smaller than Oh Pt^{4+} and 25% larger than square planar Pt^{2+}. In these air-exposed samples, the Pt^{2+} species could be interacting with an additional O to form the 5th Pt-O bond. XPS results demonstrating that Pt^{4+} is a minority species also rule out the possibility of a 50/50 mixture of 4 coordinate Pt^{2+} and 6 coordinate Pt^{4+} which would appear as 5 coordinates. The lack of intense second shell Pt-O-Pt scattering typical of platinum oxide clusters confirms that the platinum is present as

isolated single atoms. The Pt-O distance (2.04 Å) is also not consistent with Pt doped in the CeO_2 lattice and occupying Ce cation sites which would have 8 O neighbors at 2.34 Å.[54]

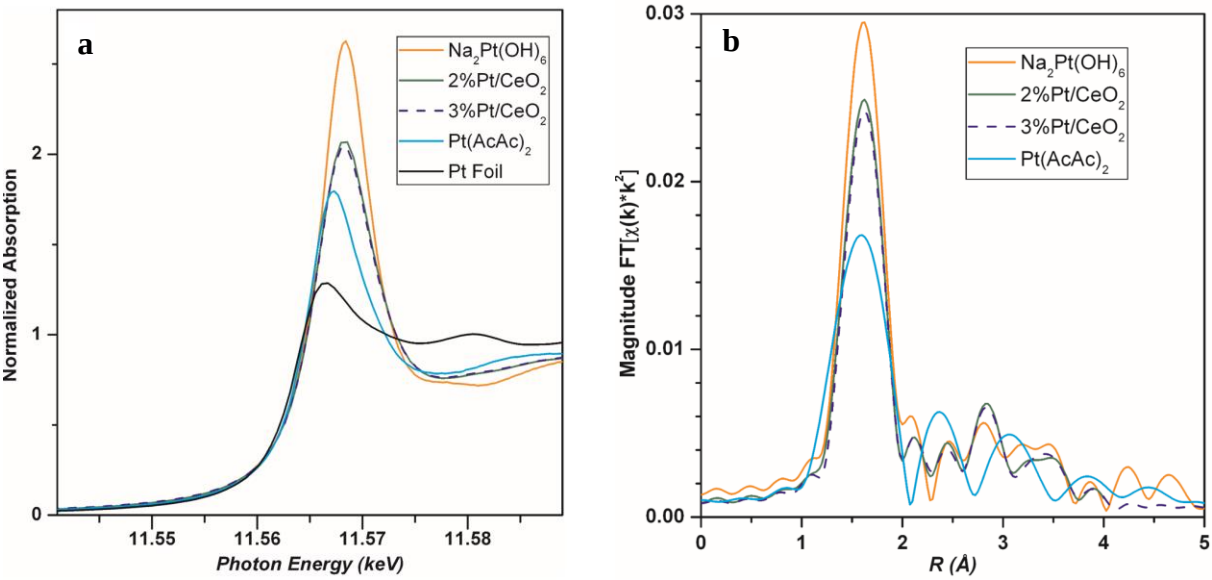

Figure 4.4. *(a) Pt L3 XANES from 11.54 – 11.59 keV of $Na_2Pt(OH)_6$, $Pt(acac)_2$, Pt foil and 2 wt% Pt/ceria, and 3 wt% Pt/ceria after heating in air at 800˚C. (b) Fourier transform magnitude of the EXAFS.*

Table 4.2 Analysis of EXAFS data on Pt/CeO_2

Samples	XANES edge energy (keV)	Scattering pair	CN	R (Å)	$\Delta\sigma^2$ ($Å^2$)	E_0 (eV)	Comment
Pt Foil	11.5640	Pt-Pt	12	2.77	0.0	-0.2	Pt^0
$Na_2Pt(OH)_6$	11.5666	Pt-O	6	2.05	0.0	-0.3	O_h Pt^{4+}

$Pt(AcAc)_2$	11.5652	Pt-O	4	2.03	0.0	-0.3	D_h Pt^{2+}
2 wt% Pt/CeO_2	11.5657	Pt-O	4.8	2.04	0.0	-0.2	Pt^{2+} single site
3 wt% Pt/CeO_2	11.5656	Pt-O	4.8	2.04	0.0	-0.1	Pt^{2+} single site

4.3.3 Exclusive Formation of Atomically Dispersed Pt

The results presented so far indicate that the catalyst as-prepared contains exclusively single-atom Pt species which are bound very strongly to the ceria, such that even after exceeding the saturation coverage, we see co-existence of large Pt particles and single-atom Pt species, but no clusters of Pt. To understand the mechanism for the formation of single Pt species we investigated theoretically the adsorption of single Pt species, particularly gaseous PtO_2, which has been identified as a possible mobile species in Ostwald ripening[8,25] to oxidized Pt clusters on CeO_2 (111). By microscopic reversibility, the detachment energy of the gas phase species from the clusters is the same as the adsorption energy with a sign change.

In these calculations, we did not explore metallic Pt clusters because metallic Pt will not be stable under the experimental conditions used for atom trapping. Ganzler et al.[25] showed that small Pt particles are readily oxidized at temperatures as low at 350 °C under oxidizing conditions. Instead, we consider the adsorption of gaseous PtO_2 onto two oxidized Pt clusters $Pt_{10}O_{20}$ and Pt_4O_6 on CeO_2 (111). Several adsorption configurations have been explored and the lowest adsorption energies are -0.88 eV and -0.80 eV, respectively. The small adsorption energies for the PtO_2 species on platinum oxide clusters suggest the facile

release of such species into the gas phase at high temperatures, because of their small detachment energies. These results are consistent with the low vapor pressure of platinum oxide solids and confirm that the PtO_2 species are likely to serve as a mobile species in the gas phase, consistent with the other DFT studies.[8,25]

To further explore the possibility of the PtO_2 species serving as the mobile species on CeO_2 (111), the energy cost for its detachment from the platinum oxide clusters $Pt_{10}O_{20}/CeO_2$ (111) and Pt_4O_6/CeO_2 (111) onto the CeO_2 (111) surface is calculated. The PtO_2 species adsorbs on CeO_2 (111) with Pt on the oxygen top site and one of its oxygens connecting to a lattice Ce (see Figure 4.5), with a small adsorption energy of -0.67 eV. The small endothermicity of 0.01 and 0.09 eV for this detachment process, respectively, suggests that the formation of adsorbed PtO_2 is possible on CeO_2 (111). To understand its migration on the ceria surface, we have investigated several diffusion pathways of PtO_2 on CeO_2 (111). As shown in Figure 4.5, they have roughly the same diffusion barrier between 0.61 and 0.71 eV, which are quite close to its adsorption energy (-0.67 eV) on CeO_2 (111). This suggests the migration is most likely through the gas phase PtO_2 species. Indeed, it can be seen from the transition state structure in Figure 4.5 that the distance between the PtO_2 species and the surface is about 2.95 Å, with the PtO_2 in collinear geometry, the same as the gaseous counterpart. These results again imply that the gaseous PtO_2, rather than surface species, is likely to be the main mobile species at high temperatures.

On the other hand, the calculated adsorption energy of PtO_2 at the step site of CeO_2 (111) is -2.94 eV, significantly larger than its adsorption energy at the CeO_2 (111) terrace (-0.67 eV). The energetics of the detachment and diffusion of PtO_2 species on CeO_2 (111) is shown in Figure 4.5. Based on the energetics, it is concluded that the formation of the

strongly bound single-atom Pt species (PtO_2) at the step site under oxidizing conditions is likely the result of the detachment of PtO_2 species from oxidized Pt clusters on ceria terraces into the gas phase and redeposition of the gaseous PtO_2 species onto step sites of ceria. Using DFT, Wang et al.[21] concluded that the adsorption of PtO_2 on step edges of metallic Pt was only slightly less favorable than the CeO_2 (111) step sites. This would explain why large metallic particles are seen only when the saturation concentration of Pt single atom species is exceeded.

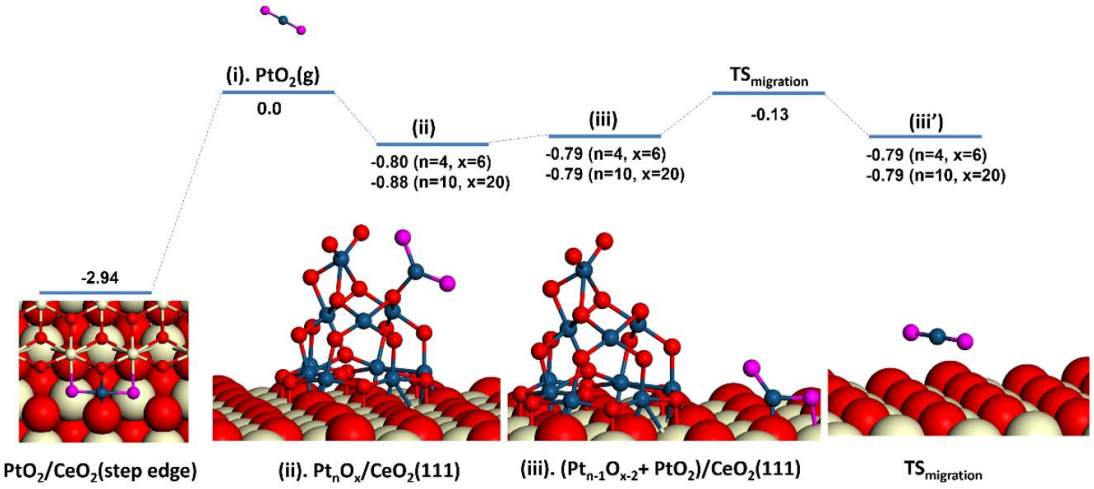

Figure 4.5. *The calculated adsorption energy of the PtO_2 species on CeO_2 step edge and on Pt_nO_x/CeO_2 (111) (n=4 and 10, x=6 and 20) as well as the energy cost for the detachment of this PtO_2 species onto the CeO_2 (111) surface. The energy barrier for PtO_2 migration on the CeO_2 (111) surface is also shown. The corresponding optimized structures along the pathways are also provided. Color: Ce, yellow; lattice O, red; O in PtO_2, purple; Pt, blue.*

To determine the preferred location of the Pt atoms at step edges, possible structures of Pt on the step sites of CeO_2 (111) were considered (Figure 4.6a-c). The adsorption geometry

of a single Pt atom at the CeO_2 step is given in Figure 4.6a. The Pt is located at a bridge site by binding to two oxygen atoms from the first and second CeO_2 (111) layers, with Pt-O bond lengths of 2.00 and 2.00 Å. Its adsorption energy is -4.98 eV, which is in good agreement with the previous value of -5.1 eV.33 The location of Pt atoms on the ceria steps are consistent with the previously reported STM images of Dvorak et.al.[17]

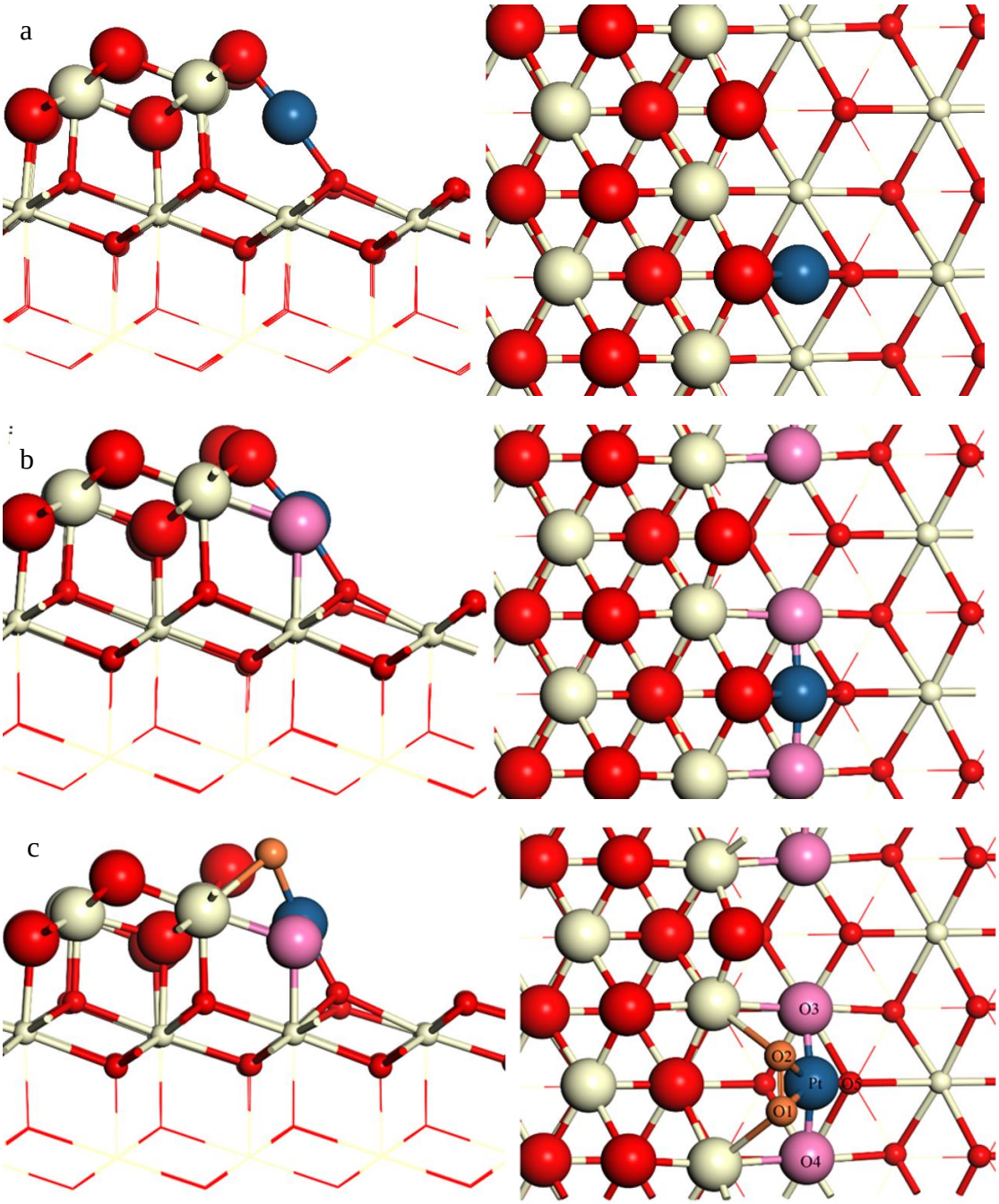

Figure 4.6. *(a) Side and top views of the geometry of Pt adsorbed on CeO_2-step, (b) Pt adsorbed on CeO_2-step with two excess Os and (c) Side and top views of O_2 adsorption on Pt@step-O with a step oxygen vacancy. Color: Ce, yellow; lattice O, red; O in PtO_2, pink; Pt, blue; O in O_2, orange.*

The geometry of a single Pt atom adsorbed on the CeO_2 step site with two excess O atoms is shown in Figure 4.6b. The two excess oxygen atoms could be due to the PtO_2 species from the gas phase, which lands on the step site. The Pt atom is bound to four O atoms, forming a square planar motif with the Pt-O distances of 1.89, 1.89, 1.99, and 2.03 Å. The adsorption energy of Pt is -7.31 eV, indicating the high stability of the structure. The Bader charge of the Pt is 1.13|e|, suggesting a Pt^{2+} character. The Pt^{4+} species in PtO_2 is presumably reduced by the under-coordinated Ce^{3+} at the step edge to Pt^{2+} (Scheme 4.1). It is clear that the square-planar geometry (Figure 4.6b) is more stable than that without the two excess oxygens (Figure 4.6a). These results are also consistent with the earlier results of Dvorak et al.[17] who noted the beneficial effect of excess oxygen for achieving high concentrations of atomically dispersed Pt. However, in that study, the authors found that exceeding the saturation limit caused the appearance of clusters of Pt, which are not seen in our work, which we suspect is due to the different synthesis conditions. In our work, the catalyst is prepared by heating in air at 800 °C, under which condition the smaller clusters of Pt oxide are not stable due to the emission of gaseous PtO_2 species.

To understand the five-coordinated species involving Pt, which is suggested by the EXAFS experiment (Table 4.2), we explored the possibility that one of the Pt-bound O is replaced by O_2. This is plausible since the Pt/CeO_2 catalyst was prepared in the air at high temperatures and the air-exposed samples were analyzed. When an oxygen vacancy is formed at the CeO_2 step site, O_2 can adsorb at the oxygen vacancy. This situation is considered in Figure 4.6c, where a step O bound to Pt is replaced by O_2 on Pt/CeO_2. The O_2 moiety has both O atoms bonded to Pt and two Ce atoms in the top layer. In this planar configuration, therefore, Pt is bonded with five O atoms with the Pt-O distances of 2.07 Å

(Pt-O1), 2.07 Å (Pt-O2), 1.96 Å (Pt-O3), 1.96 Å (Pt-O4) and 2.01 Å (Pt-O5), respectively. This configuration is consistent with the experimental EXFAS averaged bond length of 2.04 Å (see Table 4.2 and Figure 4.4). The adsorption energy for O_2 is -1.86 eV, which is comparable to the oxygen vacancy formation energy (2.12 eV). The small endothermicity of 0.26 eV makes the substitution of a step O bond to Pt by an O_2 molecule quite plausible. When the catalyst is exposed to CO, we expect this adsorbed oxygen to react readily, allowing CO to occupy the Pt^{2+} site on the ceria.

This location of the Pt in both of our DFT models also matches with the AC-STEM images. The Pt atom lies very close to the (111) ceria plane and also on the (200) plane. This explains why our results (Figure 4.2), and also those of others in the literature,[32],[33] which show the Pt atoms to be lined up with the ceria lattice planes. These Pt atoms are not actually in substitutional sites, rather they are present on surface steps. Polyhedral ceria particles heated to 800 °C in air show well defined (111) facets and a multitude of surface steps, some of which are indicated with arrows in Figure 4.2b and 4.2c. Since the TEM images are projections of a three-dimensional structure, the Pt atoms on the surface appear as if they lie on specific ceria lattice planes. Due to the atom mobility induced by the beam, it becomes very difficult to find isolated atoms at the edge of the ceria particles, but they are visible, as seen in Figure 4.2c.

4.3.4 Reactivity of Atomically Dispersed Pt/CeO_2

To assess the nature of the Pt species under reaction conditions, and their stability, we used DRIFTS while performing CO oxidation at 125 °C. The CO oxidation results reported in Figure 4.7 were performed after an oxidative pretreatment to simply clean off adsorbed impurities, no reduction was performed. By using excess oxygen in the feed, the catalyst

does not change its state or get reduced, as evident from the FTIR data. The band of adsorbed CO is similar across the entire range of metal loadings (Figure 4.7). The position of the band does not change with coverage (Figure 4.7) consistent with isolated Pt sites. The FWHM of the strongly bound CO is ~23 cm^{-1}, considerably broader than the narrow band having a FWHM < 10 cm^{-1} reported by DeRita et al.[28] These authors used a very low loading of Pt (0.05 wt%) to achieve uniform single-atom sites. The high loading (3 wt%) used in our samples and the different configurations of surface steps on ceria[17] make it likely that there is not one unique configuration for the Pt single sites. The CO adsorption band on the 4 wt% Pt sample (Figure 4.7c) is further broadened due to a contribution from metallic Pt present in this sample. This is shown more clearly in the magnified view of the CO band seen initially during CO oxidation on the 4 wt% Pt sample (Figure 4.7d). The first and second derivatives show the presence of a feature at 2091 cm^{-1} corresponding to metallic Pt. However, the contribution from the metallic Pt sites is not very significant due to the large Pt particles that are present (Figure. 4.1b) hence the dominant CO species are those on ionic Pt at ~2100 cm^{-1}. This is in contrast to the work of DeRita et al.[28] where two distinct bands for adsorbed CO were seen already at 0.15 wt% and only the metallic Pt bands were seen at 1 wt% Pt loading. The synthesis conditions used in the present study tend to favor the formation of atomically dispersed Pt even at the highest metal loading used (4 wt% Pt) where the excess Pt forms large metal particles.

On these samples, the adsorbed CO on ionic Pt is strongly bound and not easily desorbed in flowing He and neither does it react with O_2 at 125 °C (Figure 4.7). This is consistent with the low CO oxidation reactivity of these single-atom catalysts at 125 °C as we show next. The frequency of the adsorbed CO band is consistent with the recent DFT

investigation of Thang et al.[54] where CO on ionic Pt at ~2100 cm^{-1} would be expected to have strongly bound CO with binding energy larger than 2 eV. The FTIR spectra (Figure 4.7) of the single-atom catalysts prepared by high-temperature vapor-phase synthesis on ceria also show a very minor feature in the range of 2042 – 2049 cm^{-1}. A CO band in this range would normally be associated with metallic Pt, based on the literature.[54,55] However, in our case, the catalyst has been prepared by heating at 800 °C in air and then pre-oxidized prior to performing CO oxidation under lean conditions. Neither AC-STEM nor EXAFS shows any metallic Pt particles to be present on this catalyst. Furthermore, this 2042 – 2049 cm^{-1} band is not removed when CO flow is stopped and oxygen continues to flow, which is similar to the behavior of the most intense band on our single-atom catalysts (2092 - 2101 cm^{-1}). On the other hand, CO adsorbed on metallic Pt readily reacts with oxygen when CO flow is stopped.[1] Hence we associate the minor feature seen around 2042- 2049 cm^{-1} to the single-atom Pt species, which represents the only form of Pt seen via AC-STEM and via EXAFS. The catalyst that contains metallic Pt is the 4wt% Pt/ceria where the Pt particles are large and can be seen via SEM and XRD (Figure 4.1). This metallic Pt makes only a very modest contribution to CO oxidation activity (see Appendix II, Figure II.8). We examined the FTIR results on this catalyst very carefully and found that a small shoulder in Figure 4.7c might be attributed to metallic Pt. Further derivative analysis of this spectrum suggested that the feature was located at 2089 cm^{-1}. The assignment of this band to metallic Pt is consistent with CO adsorbed on well-coordinated, ie large Pt particles as reported in the literature.[55] The CO stretch frequency also happens to be very similar to the intense CO band seen in all of the catalysts reported here (Figures 4.7a and 4.7b). While the assignment of a CO stretches around ~2091 cm^{-1} to Pt nanoparticles and the 2101 cm^{-}

[1] feature to ionic Pt (Figure 4.7c) may be surprising, it is consistent with the literature[56] who report that there is considerable overlap in the observed CO stretch frequencies on metallic nanoparticles and ionic Pt. These authors have questioned whether the state of Pt can be unambiguously determined from the CO stretching frequency. Our assignments are based on the physical evidence gathered from a number of characterization techniques. In summary, the similar symmetrical CO band seen with increasing metal loading confirms that ceria provides sites for trapping atomically dispersed Pt at high concentrations (~1 atom/nm^2).

The CO oxidation reactivity measured in a flow reactor is shown in Figure 4.8. The CO oxidation was performed after an oxidative pretreatment to simply clean off adsorbed impurities, no reduction was performed. By using excess oxygen in the feed, the catalyst does not change its state or get reduced, as evident from the FTIR data in Figure 4.7. These catalysts show increased reactivity with loading, and when expressed as a TOF, the performance is very similar, confirming that the Pt sites over the range of loading (1 – 3 wt%) are very similar. The 4wt% Pt/CeO_2 sample contains both metallic Pt as well as atomically dispersed Pt. Since the Pt is present in the form of large particles, adding extra Pt makes only a modest improvement in reactivity (Appendix II, Figure II.8). The single-atom catalyst is not the most active form of Pt. The catalyst needs to be activated via high-temperature steam treatment,[57] or via a reduction in CO at 275 °C (Figure 4.8c). The former treatment creates active hydroxyl groups that enhance the reactivity of the single-atom catalyst. The reduction treatment transforms a portion of the single-atom Pt into nanoparticles, leading to an onset of CO oxidation reactivity at RT and 100% conversion by 80 °C.

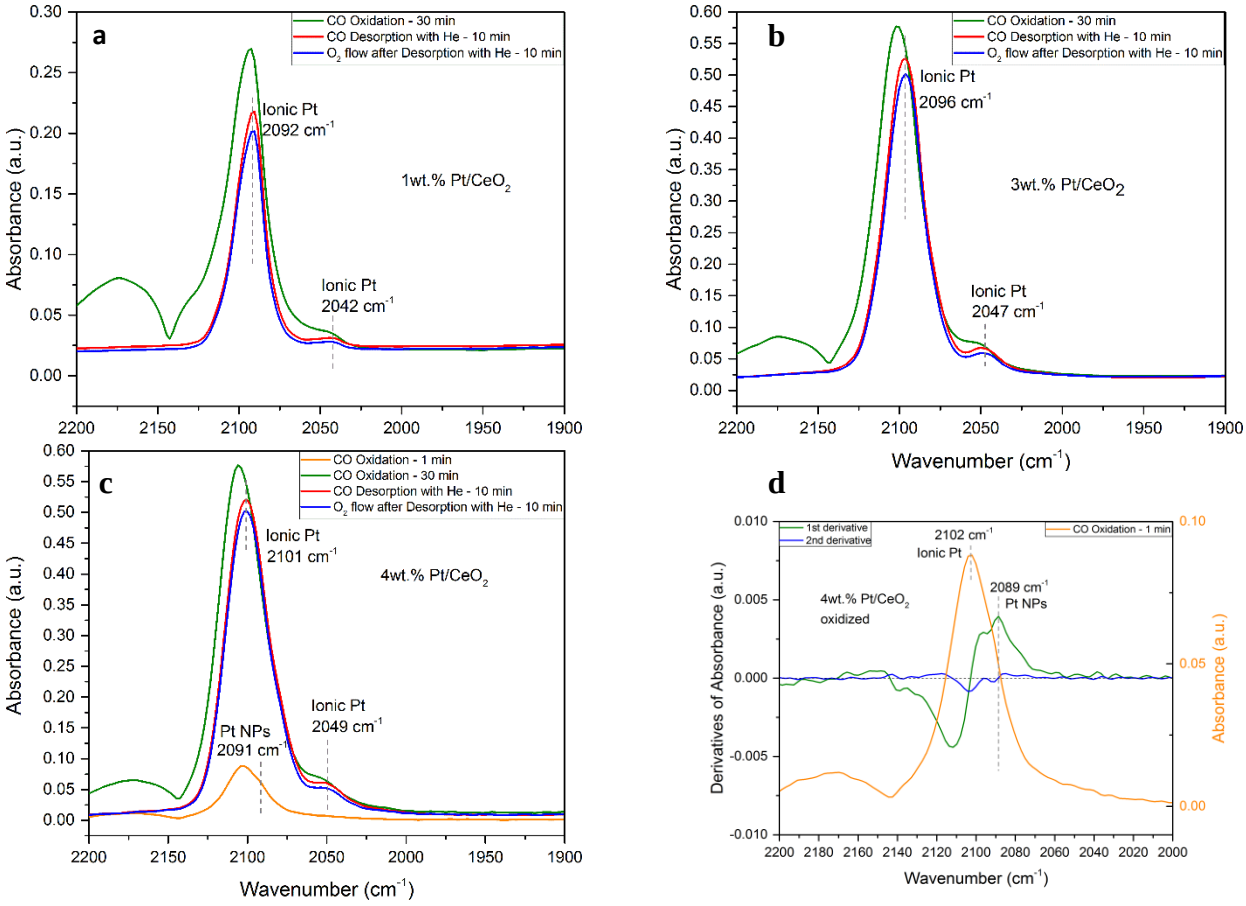

Figure 4.7. *(a) FTIR of adsorbed CO on the 1wt%Pt/CeO₂ during CO oxidation at 125 °C, and after stopping the CO flow and purging with He, and later while purging with O₂. This shows that the CO is strongly bound to the ionic Pt species. Similar experiment with the (b) 3 wt% Pt/CeO₂ and (c) 4wt% Pt/CeO₂. The CO adsorption band for the 4wt% Pt samples suggests an additional component is present, indicated by the 2091 cm^{-1} band seen most clearly in the spectrum obtained after 1 minute of reaction. (d) The 1st and 2nd derivative analysis of the 1 min spectrum shows this feature at 2091 cm^{-1}, which can be assigned to large metallic Pt particles.*

The mechanisms for the enhanced reactivity of the reduced Pt catalyst are outside the scope of this work and are presented elsewhere.[19] The single-atom catalyst can, therefore, be considered the precursor to a very active Pt/ceria CO oxidation catalyst.

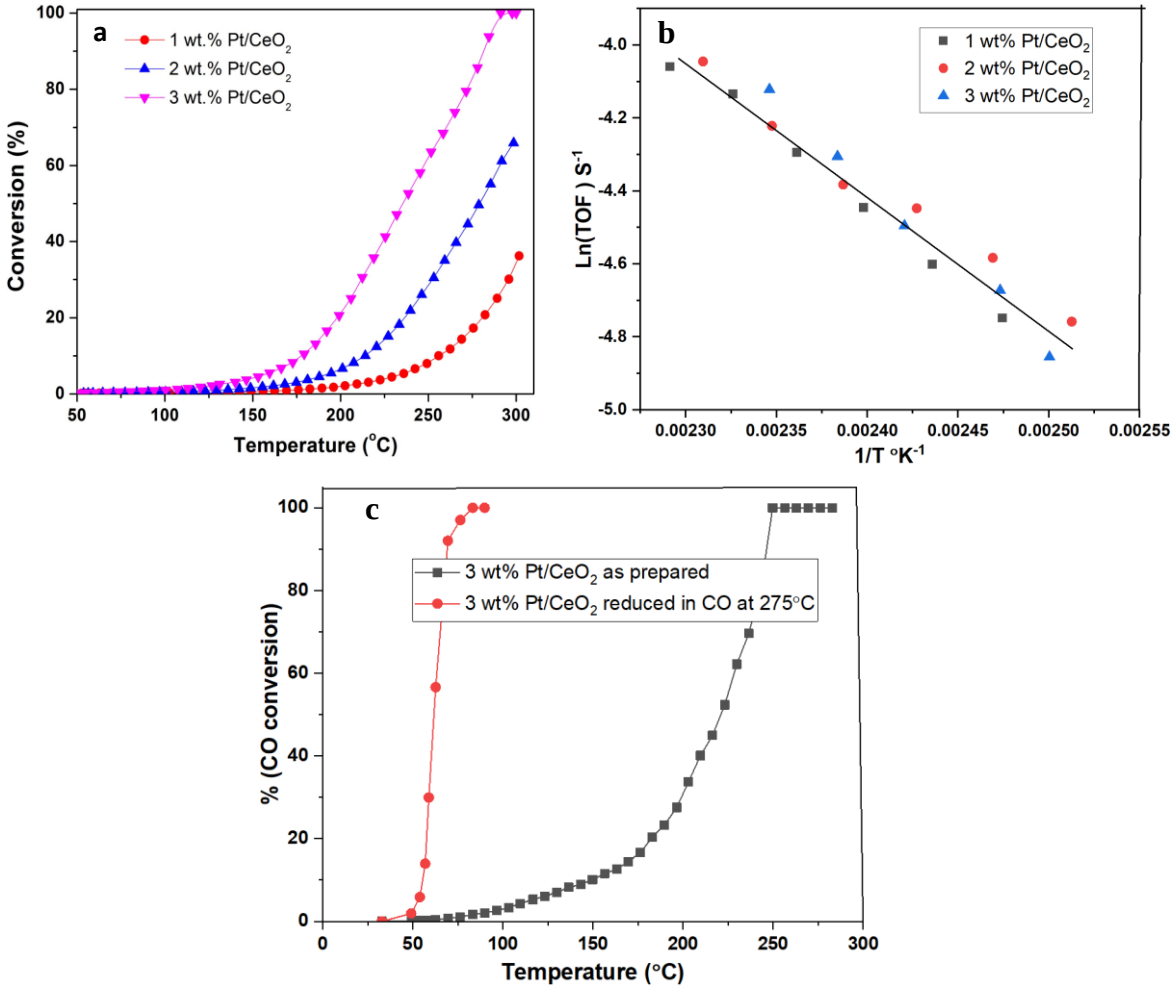

Figure 4.8. *(a) CO oxidation reactivity on the Pt/ceria catalysts, third run reported, demonstrating the stability of the single atoms when using lean conditions (1 sccm of CO, 1.5 sccm of O_2, 75 sccm of He with 20 mg of catalyst, at a total pressure of 83.3 kPa. (b) Turnover Frequency (TOF) as a function of reciprocal temperature. (c) CO oxidation reactivity of the 3 wt% Pt/CeO_2 after reduction in CO at 275 °C.*

4.4 Conclusions

The results reported here demonstrate the remarkable behavior of ceria supports that allow trapping of ionic Pt keeping it atomically dispersed. Under-coordinated Ce^{3+} cations at the ceria step edges can react with PtO_2, sharing the oxygens provided by the Pt, to form strong covalent bonds that result in the thermally stable single atoms (Scheme 4.1). The strong binding of the PtO_2 to step sites on CeO_2 (111) and the weak interaction with Pt oxide clusters leads to the exclusive formation of atomically dispersed Pt. Only when the Pt loading is in excess of the saturation capacity that metallic particles of Pt are seen. The results of bulk elemental analysis combined with the BET surface area help identify the upper limit for stabilizing atomically dispersed Pt to be 1 atom/nm^2 which yields 3 wt% of atomically dispersed Pt on the high surface area ceria support (Solvay HS 5). The combination of surface-sensitive spectroscopic techniques, LEIS, XPS, and DRIFTS, confirm that the Pt atoms are located on the surface of the ceria. The DFT computations show the stable site involves the binding of Pt to surface oxygen atoms at the ceria steps with an average distance of 2.04 Å which is confirmed by EXAFS measurements. The AC-STEM images are consistent with Pt and are bound to step edge sites on the ceria.

The results can be considered in the context of catalyst sintering, where the growth of metal nanoparticles leads to loss of catalyst activity.[42] The dominant mechanism for catalyst sintering is Ostwald Ripening[7] wherein mobile single atom species emitted from the smaller nanoparticles are captured by the larger particles. Calorimetric measurements show that small clusters (and especially single metal atoms) on ceria (111) have higher energy than the bulk metal[58] causing them to be less stable and prone to sintering. In contrast, in this work the transition metal was delivered in the form of a metal oxide, allowing covalent

bonds can be formed with the support trapping the single atoms and causing catalyst sintering to be slowed down. The process of atom trapping described here is relevant to industrial catalysts used for hydrocarbon conversions such as dehydrogenation,[59] which become poisoned due to carbon deposition and lose activity due to sintering. These industrial catalysts are regenerated via oxidative treatments at ~540 °C to burn the carbon and re-disperse the transition metal. Mobile transition metal oxides such as PtO^2 are formed under these conditions, and their trapping on ceria must be responsible for the sinter-resistance and ease of regeneration of the single atoms from nanoparticles.[37]

This work shows that the single atom, ionic Pt, is not active for CO oxidation at low temperatures. However, reduction in CO transforms the single-atom Pt on polyhedral ceria catalyst into a remarkably active low-temperature CO oxidation catalyst.[19] Since the Pt is strongly bound to the support, even after CO reduction a portion of the Pt remains in the form of single atoms. Likewise, in previous work, we found that when the catalyst was prepared via atom trapping, a significant fraction of the Pt remained as single atoms when heated to 680 °C for propane dehydrogenation.[37] In summary, using a high surface area commercial ceria and readily available Pt precursor, we have demonstrated high metal loading of thermally stable Pt single atoms in the form of Pt^{2+} ions, extending single-atom catalysis to the realm of industrial applications.

CHAPTER 5: STABILIZATION OF SINGLE ATOMS PT ON SPINEL USING K AS ADDITIVE

5.1 Abstract

Single-atom catalysis attracted a lot of attention because of 100% atom efficiency, higher selectivity, and better reactivity. However, stabilizing the single atoms Pt, especially on non-reducible oxide supports at elevated temperature under oxidizing conditions is still a challenging task due to the limited anchoring sites, defective sites, and lack of agility to change the oxidation state of the corresponding element that serves as support. Here we reported, the single-atoms Pt can be stabilized on non-reducible oxide spinel using potassium as a stabilizer. Multiple characterization techniques such as X-ray diffraction (XRD), aberration-corrected transmission electron microscopy (AC-STEM), low energy ion scattering (LEIS), extended X-ray absorption fine structure (EXAFS) were used to characterize the single atoms Pt on spinel. Density functional theory (DFT) was used to understand the role of potassium in the stabilization of single-atom Pt. DFT results suggest that single Pt atoms are embedded in stable K6Ox(OH)y clusters on the spinel surface. Such a scenario is consistent with the experimental data.

5.2 Introduction

Platinum is extensively used as an active component for a variety of reactions such as hydrogenation, water gas shift, CO oxidation, biomass conversion, and so on, since it can tolerate high temperature, pressure, and also resistant to oxidation. Additionally, it has been used as jewelry, medicine, painting, catalytic converter, etc. The price of this metal is soaring up every year because of its demand for various purposes as aforementioned. To control its demand, scientists are putting a relentless effort using it as efficiently as possible. Currently, the niche of heterogeneous catalysis has been working to downsizing

the metal particles to the limit of single atoms.[1] Single-atoms catalysis is a new avenue to explore in this field since it allows each surface-exposed atom to act as a catalytically active center.[32] However, the catalysts expose to high temperatures while in operation and sinter readily at elevated temperature under oxidizing conditions and form large Pt particles.[8] The mechanism of sintering is mediated via Ostwald ripening[7] in which large Pt particles form at the expense of smaller particles. In our previous study[60], we found the formation of anomalously large Pt particles due to the vapor phase assisted mechanism of volatile species PtO_2 as opposed to surface diffusion or particle migration and coalescences.[4]

Ceria has been well-known support in trapping single atoms Pt.[1,16] It has received a lot of attention because of its exceptional redox properties and outstanding oxygen storage capacity.[61,62] Due to the reducibility nature of cerium, it traps Pt single atoms at step edges as first shown by Dvorak et.al.[17] Bruix et. al.[39] suggested the ceria nano-pockets are responsible in trapping Pt atoms. These nano-pockets expose the ceria (100) facets that are adequately presented in ceria cubes. Jones et al.[1] reported the surface area of ceria cubes collapsed while heating to elevated temperatures. He found the large Pt particles when he added the Pt metal to the ceria cubes and heated to 800 °C, suggesting that ceria cubes do not trap Pt atoms. However, when he added the polyhedral ceria to $Pt/LaAl_2O_3$ catalysts and heated to 800°C, he found the Pt transferred from $Pt/LaAl_2O_3$ catalysts to ceria in the form of volatile species PtO_2 and get trapped in the form of single atoms.[1] The volatile species land to the step edges of ceria (111) at elevated temperature under oxidizing conditions and get strongly binds to ceria through Pt-O-Ce linkages.[16] Despite good trapping agents, its availability in the earth's crust is very low since it is a rare earth metal. Therefore, it is extremely important to find the alternative of ceria support for trapping Pt

atoms in order to make industrially relevant and sustainable Pt-based single-atoms catalysts.

Alumina is the most commonly used support in automotive exhaust control industries because of its abundance in nature. Zhang et. al.[63] reported that single-atom Pt can be stabilized in the internal surface of m-Al_2O_3 and they claimed that the sites responsible for stabilization Pt atom is unsaturated pentahedral Al^{3+} centers. Dopping of La to the alumina to make it thermally stable support. Wang et. al.[13] stabilized single-atom Pt on La-doped Al_2O_3 by using barium as an additive. However, they could not able to reveal the role of additive in trapping Pt atoms and the site responsible for atom trapping. Especially, it is challenging to locate the sites responsible for atom trapping via DFT when there are multiple elements presented in the system. $MgAl_2O_4$ is another common support that has been used in automotive industries for emissions control. It is robust and thermally stable support and it can stabilize small Pt nanoparticles ranging from 1-3 nm.[12] Besides Pt, it has the ability to stabilize Rh and Ir particles of sizes 1-3 nm at elevated temperature for an extended time.[64] However, in our previous work, we found that anomalously large Pt particles are formed in this support when aged at 800 ˚C under flowing air without potassium.[60] Luo et. al.[65] trapped single-atom Pt on $MgAl_2O_4$ support at high temperature by using K as a stabilizer and they used this system to trap NO_X. However, the role of K as a stabilizer is still unknown. The focus of this paper will be to unveil the role of K in the stabilization of single-atom Pt, based on experimental evidences as well as DFT work.

5.3 Experimental Details

5.3.1 Materials and Methods

Magnesium aluminate ($MgAl_2O_4$) and tetraamine platinum nitrate were purchased from Sigma Aldrich. The pore volume of $MgAl_2O_4$ (1.8 ml/g) was determined by first wetting the dry $MgAl_2O_4$ powder with water. The impregnation of the platinum precursor was done to fill the pores of $MgAl_2O_4$. The tetraamine platinum nitrate solution was loaded to make 0.5% and 1wt% Pt on $MgAl_2O_4$ in multiple aliquots and dried at 110 °C for 4 hours until all the water evaporated in the air after each impregnation. The samples were first calcined in a tube furnace with 100 ml/min of air for 4 hours at 500 ˚C in order to make the first set of catalysts. K_2CO_3 was used as a source of K. Then 2 wt% K solution was loaded to the second set of each catalyst by using wet impregnation and dried at 110 ˚C for 4 hours until all the water evaporated in the air. The samples were then calcined in a tube furnace with 100 ml/min of air for 1h in the air at 800 °C. The furnace temperature was ramped up at 1°C per minute.

5.4 Characterization and Experimental Details

Samples characterization were done via Brunauer Emmett Teller analysis (BET), X-ray Diffraction (XRD), Transmission Electron Spectroscopy (TEM), Aberration-Corrected Transmission Electron Microscopy (AC-STEM), X-ray Absorption Spectroscopy (XAS), Low Energy Ion Scattering (LEIS), and Fourier Transform Infrared Spectroscopy (FTIR). Micromeritics Gemini 2360 surface area analyzer instrument was employed to determine surface area. The samples were degassed with nitrogen gas overnight at 120 ˚C prior to analysis. XRD analysis was performed with a Rigaku SmartLab diffractometer equipped with a D/TeX detector using copper Kα radiation. Scans were performed at a 6.2˚/min rate

and a 0.02˚ step size. The XRD patterns were analyzed using the whole pattern fitting, Rietveld analysis, the MDI Jade software package was employed. For the TEM analysis, a small pinch of the powder sample was put in an agate mortar and ground with ethanol to create a suspension. A drop of this suspension was deposited on a 3 mm holey carbon grid. TEM was performed using a JEOL 2010F microscope operated at 200 kV with a Schottky emitter. We determined the content of Pt using transmission electron microscopy energy dispersive spectroscopy (TEM-EDS) technique. A total of 10 such regions were analyzed by TEM-EDS for Pt quantification. The average of these analyses was reported, and an Oxford Aztec system was used for the EDS analysis. High-resolution transmission electron microscopy and scanning transmission electron microscopy was carried out in a JEOL 2010F microscope. JEOL JEM ARM200CF 200 kV aberration-corrected (AC) transmission electron microscope (resolution of 0.08 nm) at the University of Illinois at Chicago was used to observe single-atoms Pt. XAS characterization was conducted at the Stanford Synchrotron Radiation Light source (SSRL). CO oxidation was chosen as a probe reaction. Reaction rate measurements were performed using ¼ inch diameter U-tube with 20 mg of sample. The gas flow rates for CO oxidation were: CO 1.5 ml/min, O2 1 ml/min and He 75 ml/min (space velocity 232,500 ml/g/h). The products were analyzed by a Varian CP-4900 Micro GC while the reactor temperature was ramped up at 2 °C/min.

LEIS was used to determine the concentration of Pt atoms on the surface. This technique[44] selectively detects the topmost atoms. The experiments were carried out using an IONTOF Qtac100 instrument which is a dedicated LEIS instrument equipped with a double toroidal analyzer for the energy analysis of the backscattered ions. The analyzer has a large solid angle of acceptance (full 360° azimuth), while the scattering angle is fixed at 145°. This

gives, in combination with parallel energy detection, a high sensitivity while maintaining the mass resolution. He+, as well as Ne+ ions, were used with ion energy 3 and 5 keV and current 5 and 2 nA, respectively, to analyze the surface Pt^{2+} ions in the 0.5wt% $Pt/MgAl_2O_4$ catalyst. The area scanned by these two ions was 2×2 mm^2 and the ion flux given to the samples was 1.4×10^{14} ions/cm^2 and 2.8×10^{13} ions/cm^2 respectively. The spectra for the Pt reference were analyzed within a 1.5×1.5 mm^2 sputter crater over an area of 1×1 mm^2. The analysis time was adjusted such that the surface damage was the same as for the other spectra. Assuming a sputter coefficient of 0.1 for He and 1 for Ne, this will lead to surface damage of 1% and 2% at the end of the analysis.

5.4.1 Computational Details

All calculations were performed using the spin-polarized density functional theory (DFT),[66] as implemented in the Vienna Ab initio Simulation Package (VASP) code.[46] The generalized gradient approximation (GGA) of Perdew and Wang in 1991 (PW91) was employed for the exchange and correlation functional.[67] While the valence electronic wavefunction is expanded in terms of plane waves with a ceiling (450 eV), the core electrons are treated within the projector augmented wave (PAW) method.[48] Monkhorst-Pack grids of 4x4x4 and 1x1x1 were used in the optimization of the bulk phase and supercell surface, respectively. The calculated bulk lattice parameter of magnesium aluminate spinel ($MgAl_2O_4$) was 8.14 Å, which agreed well with the experimental value of 8.086 Å.[68] Two facets were used to simulate the support surface, i.e. (100) and (111). Structure models of the (100) surface were simulated by a Mg-terminated surface with only half the surface Mg sites occupied (Mg 50%) and one Mg-Al antisite defect in the subsurface to obtain a nonpolar and stoichiometric surface termination.[69] On the other

hand, the surface termination for (100) surface consists of Mg, Al, and O atoms with the composition of $Mg_3Al_4O_8$. Along the [100] direction, the atomic stacking sequence of the model was $Mg_3Al_4O_8$-Al-$O_4Al_4O_4$-Mg_2-R1. R1 represents a complete -($O_4Al_4O_4$-Mg_2)- repeating unit in the [100] direction. Following the experiment and simulation by Liu et al.[70], a reconstruction model of the (111) surface was built. The topmost surface layer is made of oxygens. The second atomic layer was formed from a Mg-Al-Mg tri-layer with the composition of $Mg_{0.5}Al_{3.5}$. The distance between the $Mg_{0.5}Al_{3.5}$ sublayer and the third oxygen atomic layer was 1.70 Å. While along the [111] direction, the atomic stacking sequence of the (111) model is O_4-$Mg_{0.5}Al_{3.5}$-O_4-Al_3-O_4-Mg-Al-Mg-R2. R2 includes a complete -(O_4-Al_3-O_4-Mg-Al-Mg)- repeating unit along the [111] direction.

A (4×4) supercell with 8 atomic layers for the (100) surface and a (2×2) supercell with 9 atomic layers for the (111) surface were used to study atoms and clusters adsorption. A vacuum region of 15 Å was employed to avoid the interaction between images. Before the geometry optimization of the two surfaces, the top six atomic layers were relaxed, while the remaining layers were fixed to simulate the bulk effects. The convergence of relaxation was checked with a 0.02 eV/Å criterion. The total energy difference is less than 10-5 eV. The adsorption energy Ead was used to evaluate the interaction of atoms or clusters with spinel $MgAl_2O_4$ surfaces, and it was calculated as follows:

$$E_{ad}=(E_{adsorbate/slab}-E_{slab}-E_{adsorbate})$$

where $E_{adsorbate/slab}$ is the total energy of the adsorbate/slab system, E_{slab} is the total energy of the surface slab, and $E_{adsorbate}$ is the energy of an isolated atom or cluster.

5.5 Results and Discussion

Table 5.1. Characterization of Pt-K/spinel samples.

Samples aged at 800 ˚C ($)	Pt crystallite size (nm)	Crystalline Pt wt% Via XRD (#)	Atomically dispersed Pt wt% = ($-#)	Surface area (m^2/g)
$MgAl_2O_4$ as received	-	-	-	142
1wt%Pt-2%K/$MgAl_2O_4$	64.7	0.47	0.53	85
0.5 wt%Pt-2%K/$MgAl_2O_4$	0	0	0.5	93
0.5wt%Pt/$MgAl_2O_4$	41	0.43	0.07	110

The surface area of as received spinel from Sigma Aldrich is 142 m^2/g, after aging the spinel at 800 ˚C for 1 hour, the surface area decreases to 110 m^2/g as shown in table 5.1. 0.5 and 1wt% Pt was loaded to the spinel support and calcined to 500 ˚C/4 hours in flowing air to make 0.5% Pt/$MgAl_2O_4$ and 1 wt% Pt/$MgAl_2O_4$ initial catalysts. These initial catalysts contain sub-nanometer size particles as shown in figure 5.1. This observation is consistent with our previous findings.[60] At mild calcination temperature, small Pt particles are homogeneously distributed on $MgAl_2O_4$ support and their dispersion by chemisorption is 50, which is consistent with our previous finding.[60] However, when Pt is subjected to USDRIVE Low-Temperature after treatment (LTAT) test protocol[2] i.e. aging the diesel oxidation catalysts at 800 ˚C to simulate the 150 K miles of car driving, the Pt particles

grow anomalously large lowering to the dispersion of catalytically active species

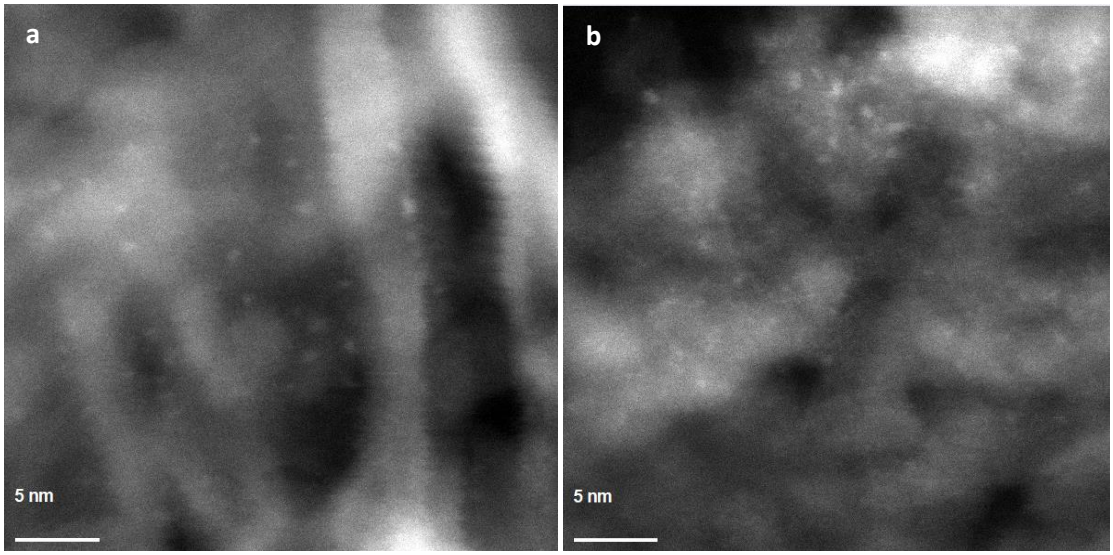

Figure 5.1 *STEM images of a) 0.5wt% and b) 1wt%Pt/$MgAl_2O_4$ calcined at 500 ˚C, show the presence of small Pt particles.*

as shown in figure 5.2a. It is known that Pt forms volatile species PtO_2 in the presence of air at elevated temperature and the vapor pressure of PtO_2 at 800 ˚C is 1.6×10^{-8} atm.[3] In our previous study,[60] the real catalyst powder was dispersed onto the silicon nitride wafer in the form of a thin layer to study the emission of Pt as opposed to model catalysts. We suggested the vapor phase transport of PtO_2 is a cause for the formation of anomalously large Pt particles.

Spinel is cheap industrial support and has high thermal stability. It has the potential to stabilize small Pt nanoparticles ranging from 1-3nm at elevated temperature.[65] Luo et al.[65] demonstrated that it can stabilize single atoms Pt with the aid of potassium additive. We added 2wt% K to the 1wt% Pt/$MgAl_2O_4$ initial catalysts then subjected to 800 ˚C treatment, we observed a strong Pt (111) peak at 2Θ 39.7˚ for this catalyst as shown in figure 5.2b. The concentration of crystalline Pt (large particles) was determined to be 0.47 wt% via

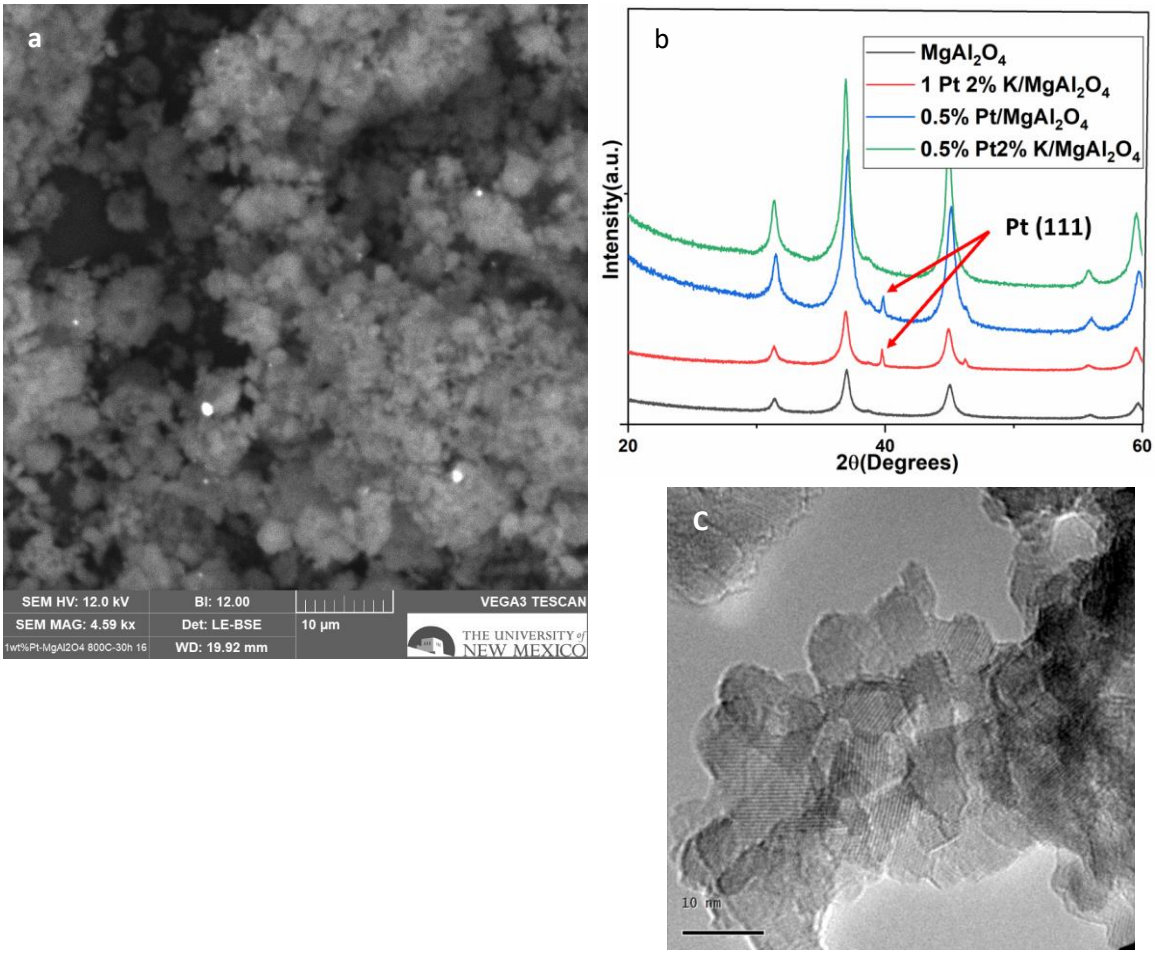

Figure 5.2 a) *SEM image of 1%Pt/$MgAl_2O_4$, b) XRD patterns c) HR-TEM image of 0.5% Pt-2K/$MaAl_2O_4$*

XRD using Rietveld refinement indicating that 0.53 wt% Pt is in atomically dispersed form as shown in table 5.1. This suggests that spinel can stabilize 0.5 wt% Pt in the form of a single atom using K as an additive. The absence of Pt (111) peak in XRD pattern for 0.5% Pt-2K/$MgAl_2O_4$ suggests the Pt may be in the atomic form as shown in fig 5.2b. For the control, we synthesized 0.5 wt% Pt/$MgAl_2O_4$ catalyst without K and aged at 800 ˚C in flowing air. We observed a strong Pt (111) peak in XRD for this catalyst as shown in fig 5.2b. The crystalline Pt content was determined using Reitveld refinement to be 0.43 wt%. These experiments indicate that potassium plays a vital role in trapping Pt atoms in spinel.

The role of potassium for trapping Pt atoms will be discussed in the section later. The surface area of 0.5% Pt/ $MgAl_2O_4$ is 110 m^2/g after 800 ˚C treatment, higher than that of K containing a sample. The reason for the drop in the surface area for 0.5%Pt-2K/$MgAl_2O_4$ sample could be the presence of K which could potentially block the pores of spinel.

The HR-TEM image of 0.5%Pt-2K/$MgAl_2O_4$ catalyst shows the absence of Pt particles as shown in figure 5.2c which is consistent with the XRD result. When we analyzed various regions of the sample via TEM-EDS we found the Pt content is 0.5wt% as shown in figure 5.3. This suggests that the Pt is present in the sample and it could be in the form of single atoms. Since the TEM at the UNM facility cannot detect the single atoms.

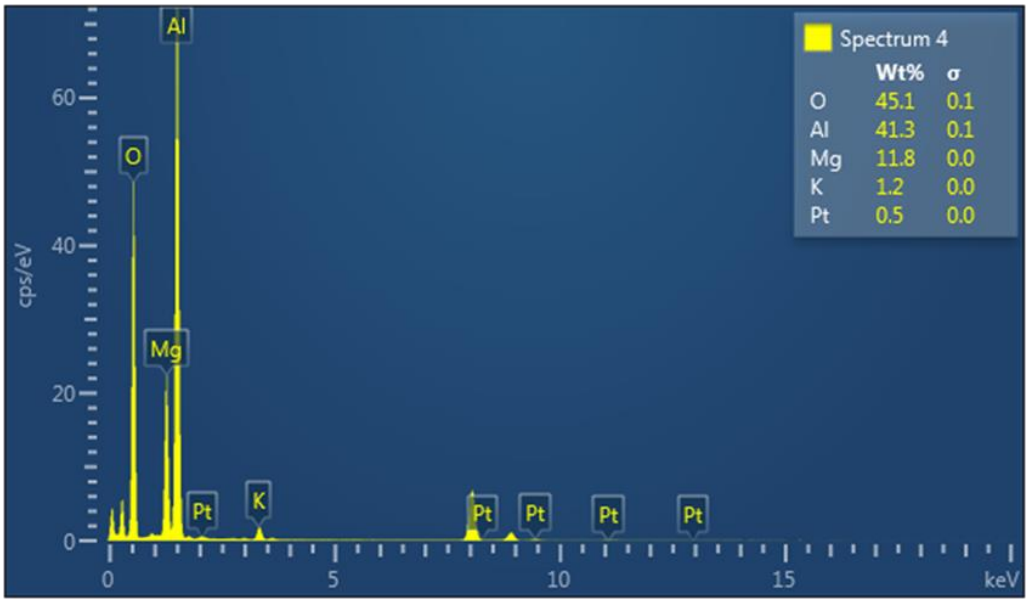

Figure 5.3 *TEM-EDS spectrum of 0.5% Pt-2K/$MgAl_2O_4$*

The direct evidence for the presence of the single-atom Pt on 0.5% Pt-2K/$MgAl_2O_4$ catalyst is observed via JEOL JEM ARM200CF 200 kV aberration-corrected (AC) transmission electron microscope (resolution of 0.08 nm) at the University of Illinois at Chicago. The AC-STEM images show the bright white dots which correspond to Pt single atoms as

shown in figure 5.4. Occasionally, Pt nanocluster is observed which co-exists with Pt single atoms. The formation of these nanoclusters could be the electron beam effect. Since a high voltage electron beam was employed to bombard the sample and the electron beam might compel to move single atoms Pt and relocate them in the form of a small cluster.

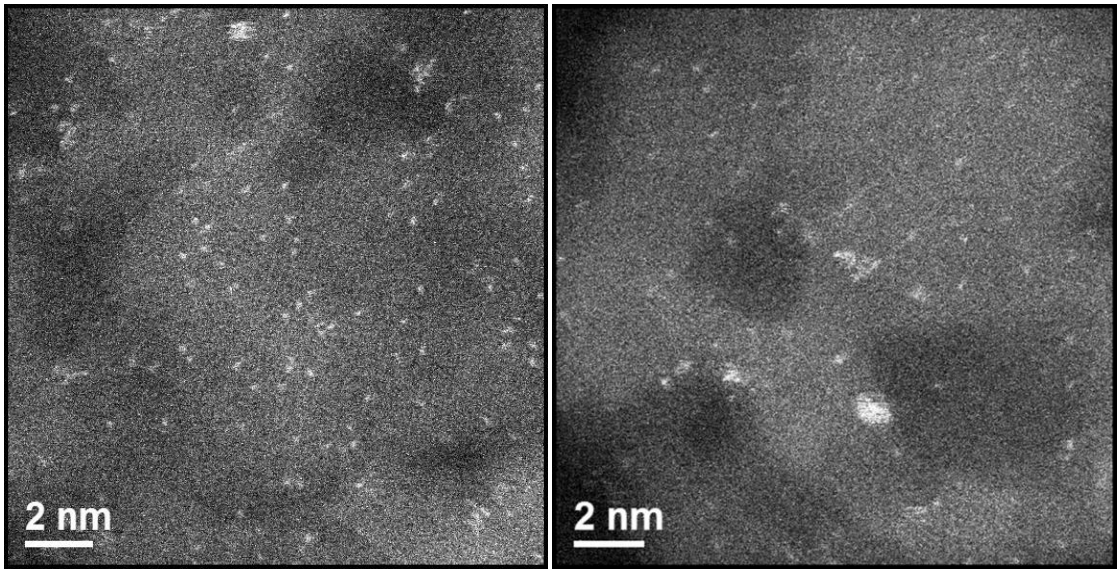

Figure 5.4 *AC-STEM image of 0.5% Pt-2K/$MgAl_2O_4$*

The single atoms Pt on spinel was also characterized by an independent true surface-sensitive technique called low energy ion scattering (LEIS), a technique that can selectively analyze surface atoms of the sample. In this method,[43] the topmost layer of the sample is bombarded with the ions of known kinetic energy. The backscattered ions which are perfectly elastic in nature are the result of the collisions with the topmost surface atoms. The energy of the backscattered ions is proportional to the mass of the scattering partner, enables the identification of the surface atoms. In this work, we used 3 keV $4He^+$ ions and 5 keV $20Ne^+$ ions. With 3 kV $4He^+$ ions the peaks signal of O, Mg, and Al were seen for $MgAl_2O_4$ without and with O treatment (Figure 5.5 a, b). Similarly, the peak signal of O,

Al, K, and Pt was seen for 0.5%Pt-2K/$MgAl_2O_4$ without and with O treatment but the peak signal for Mg is much weaker compared to bare spinel. The low peak intensity of Mg could be because of the replacement of Mg atoms by K atoms on the surface. As prepared sample has Pt signal 5 and after O atoms treatment the Pt signal went up to 5.6 which is a negligible increment of Pt signal. In figure 5.6, the Pt peak for as prepared and O atoms treatment is invisible. This is because of the Pt atoms could be surrounded by K atoms.

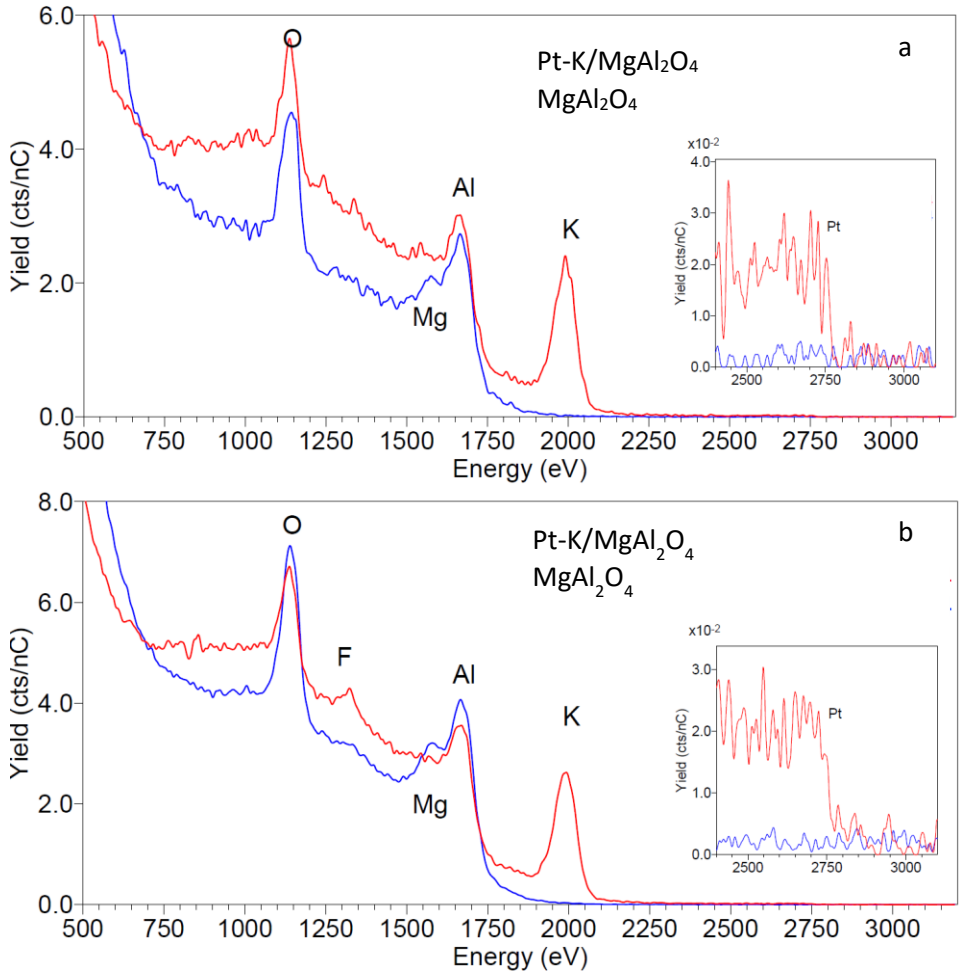

Figure 5.5 *The 3 keV 4He$^+$ spectrum for samples a) before treatment with O atoms, and b) after treatment with O atoms, showing peaks for O, F, Mg, Al, K and a small signal for Pt.*

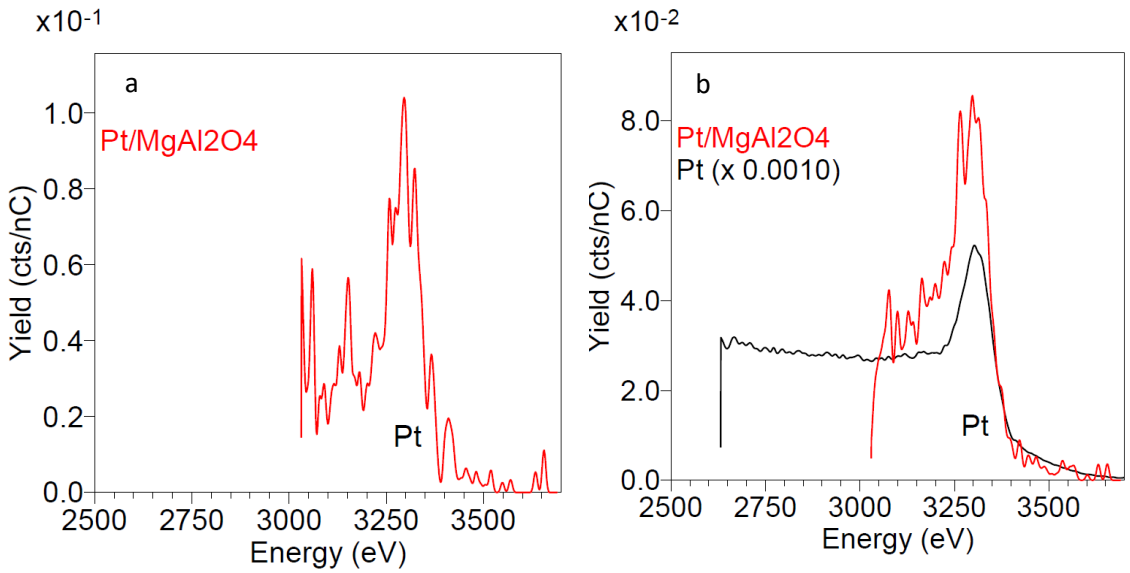

Figure 5.6 *The 5 keV 20Ne$^+$ spectrum for samples a) before treatment with O atoms, and b) after treatment with O atoms, showing peak for Pt.*

We chose the CO oxidation as a probe reaction and the CO oxidation measured in a flow reactor. Single-atom Pt catalyst is not the most active form of catalyst as shown in figure 5.7. for the CO oxidation reaction as we have shown in our previous work.[1,16] Activation by CO to the Pt/Ceria single-atom catalysts transforms it into the exceptionally active catalyst for CO oxidation.[19,25] This is because the ceria becomes highly active for the facile transfer of oxygen to CO. However, the lack of oxygen transfer from spinel lattice the single-atom Pt/spinel catalyst does not become considerably active after the CO reduction at 275 ˚C. We did not observe low-temperature performance after activation rather we observed almost the same performance as in its oxidized form. This suggests that single atoms Pt does not agglomerate into nanoparticle but stays in the form of a single atom even after reduction.

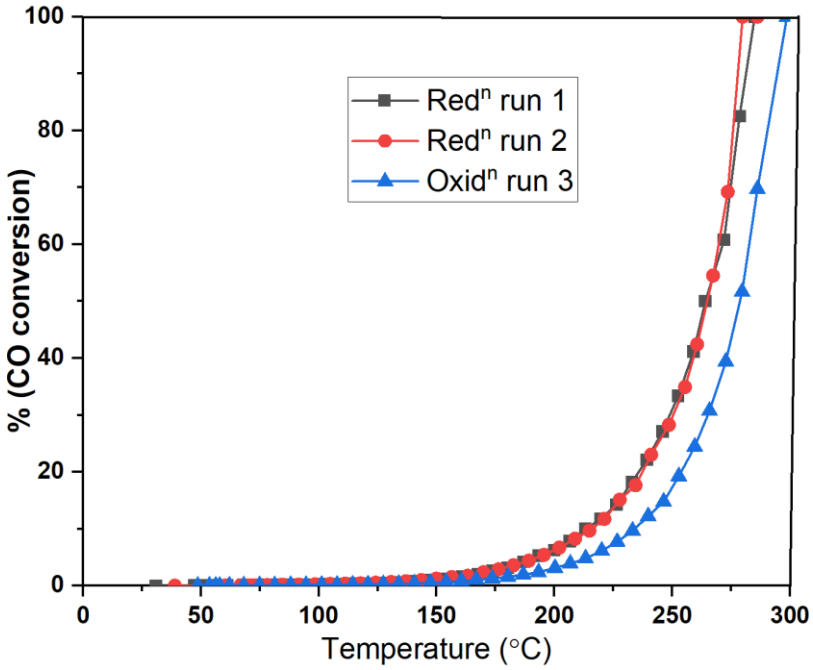

Figure 5.7 *CO oxidation activity of single atom Pt on spinel sample in reducing and oxidizing conditions*

DFT results

Spinel $MgAl_2O_4$ has a face-centered cubic (fcc) Bravias lattice with space group $Fd\bar{3}m$, where oxygen atoms form a fcc sub-lattice, with magnesium atoms occupying 1/8 tetrahedral positions and aluminum atoms occupying 1/2 octahedral positions, respectively.[71] Along the [100] direction of $MgAl_2O_4$, the repetition unit reflects a -(Mg_2-$O_4Al_4O_4$)- stacking. The stacking sequence for (111) is -(O_4-Mg-Al-Mg-O_4-Al_3)-.[72] Correspondingly, there are two terminations for the (100) surface and six terminations for the (111) surface, and all of them are polar surfaces. Previous theoretical calculations have indicated that Mg-terminated $MgAl_2O_4$ (100) surface with only half the surface Mg sites occupied (Mg 50%) is the overall most stable surface termination that complies with the polar stabilization requirements.[73] Considering some concentration of Mg-Al antisites as

reported for $MgAl_2O_4$ (100) surface,[74] 50% Mg-terminated surface with a Mg-Al antisite was used to simulate the $MgAl_2O_4$ (100) surface, shown in Fig. 1(a).

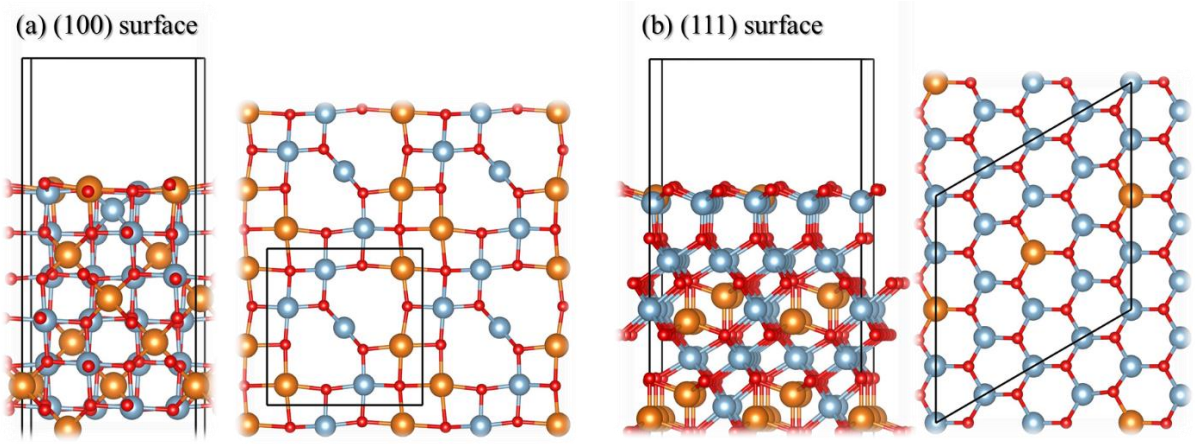

Figure 5.8 *(a) Side and top views of the stoichiometric 50 % Mg-terminated $MgAl_2O_4$ (100) surface with a Mg-Al antisite. (b) Side and top views of O-terminated $MgAl_2O_4$ (111) surface with subsurface reconstruction. Yellow atoms represent magnesium, blue is aluminum and red are oxygen.*

As illustrated in the side view ball model of Fig. 5.8(a), the top magnesium cations move into the next atomic layer and form the Mg/Al/O termination after relaxation. For an easier understanding of surface configuration, only the first and second atomic layers are shown in top view models. The number of chemical bonds of the atoms in the surface layers shows changes from the bulk. One top magnesium atom has five oxygen neighbors while magnesium atoms in the bulk have four oxygen neighbors. An aluminum atom in the top layer has five oxygen neighbors while in the bulk it has six oxygen neighbors. Fig. 5.8(b) shows a (111) surface simulations.[70] model of spinel $MgAl_2O_4$, which is consistent with previous experimental observations and in this model, it has a reconstruction that keeps the topmost oxygen atomic layer unchanged but the subsurface atoms completely rearranged.

There is a Mg-Al-Mg tri-layer between the first two oxygen layers for a bulk-truncated surface while for this model the Mg-Al-Mg tri-layer in subsurface changed into only one cation layer. As shown in Fig. 5.8(b), the cation sublayer is with the composition of $Mg_{0.5}Al_{3.5}$ which corresponds to the lowest energy composition.[70] These two special $MgAl_2O_4$ facets were used to simulate the support surface.

In order to understand the role K^+ in the formation of single-atom Pt, the adsorption behavior of Pt on $MgAl_2O_4$ (100) and (111) with and without surface K^+ was firstly studied using DFT. The corresponding geometries are given in Figure 5.9. As shown in the figure, on $MgAl_2O_4$ (100) and (111), Pt tends to adsorb on the top of O atom with the adsorption energy of -2.36 and -1.10 eV, respectively, which are significantly lower than the cohesive energy of Pt (~5.88 eV).[75] This means that single Pt atoms on bare $MgAl_2O_4$ are less stable than clusters or nanoparticles, consistent with the experimental observation.[64] With K^+ on the surface of $MgAl_2O_4$, the adsorption energy of Pt on $MgAl_2O_4$ (100) and (111) increase somewhat to -3.04 eV and -1.23 eV, respectively. However, the adsorption energy of Pt is still much lower than the cohesive energy of Pt, indicating that adsorbed Pt atoms tend to agglomerate. This is inconsistent with the high stability of Pt single atom after K^+ addition under experimental conditions. We, therefore, conclude that the Pt single atoms must exist in other forms rather than directly adsorbed on the surface of $MgAl_2O_4$.

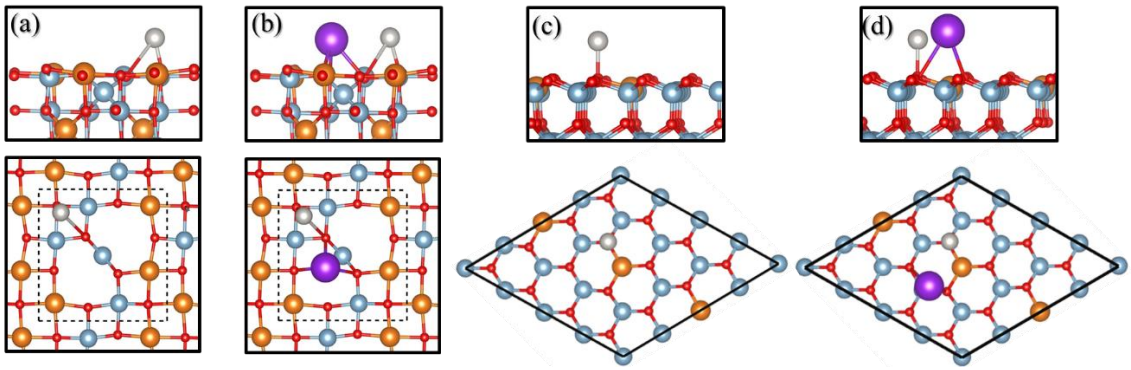

Figure 5.9 *Side and top views of adsorption configurations for Pt and K atoms on $MgAl_2O_4$ (100) and (111) surfaces. (a) and (c) represent single Pt atom adsorbed on (100) and (111) surfaces, respectively. (b) and (d) represent both Pt and K atoms adsorbed on (100) and (111) surfaces, respectively. Yellow, blue, red, purple, and silver balls represent magnesium, aluminum, oxygen, potassium, and platinum atoms, respectively*

In a recent study, it was reported that Pt can be stabilized by alkali ions (K^+ and Na^+) with OH_x species on alumina and silica. We hypothesize that the single Pt atoms on spinel surfaces are embedded in such $K_6O_y(OH)_z$ complexes on spinel surfaces. Figure 5.9 (a) illustrates the structure of one such complex ($PtK_6O_4(OH)_2$. In this structure, there are six potassium atoms binding with the central Pt atom through oxygen ligands to form single-atom-centric Pt sites. The central Pt binds with the adjacent four oxygen atoms to form a planar, making a high stable Pt single atom. The calculated binding energy of Pt on $K_6O_4(OH)_2$ cluster is -10.4 eV, which is significantly larger than the cohesive energy of Pt, thus providing a stable form of single Pt atoms on spinel.

To verify this hypothesis, the adsorption of the $PtK_6O_4(OH)_2$ cluster on $MgAl_2O_4$ (100) and (111) was investigated and the corresponding geometries are given in Figure 5.9 (b) and (c), respectively. The interaction between the complex and the surface is large via the K^+ species which interacts with surface oxygen atoms, although there is also partial bond

formation between O in the complex with Mg on the (100) surface. The calculated adsorption energies are -3.13 eV and -2.93 eV for $MgAl_2O_4$ (100) and (111), respectively, confirming the stability of the cluster on the surfaces.

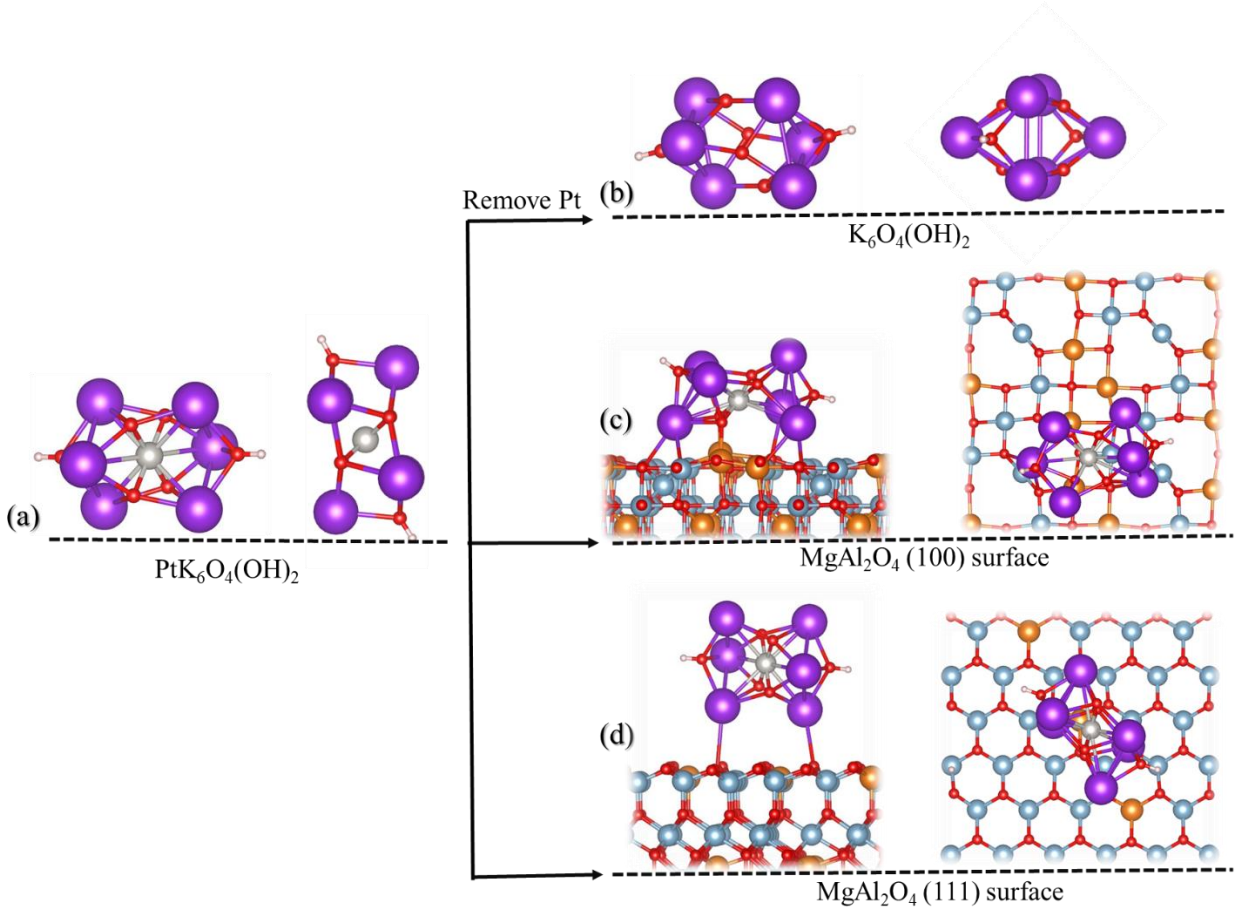

Figure 5.10 *(a) Geometric structure of $PtK_6O_4(OH)_2$ cluster. (b) represents the relaxed structure of $K_6O_4(OH)_2$ after removing the central Pt atom. Adsorption configurations of $PtK_6O_4(OH)_2$ cluster on (c) $MgAl_2O_4$ (100) and (d) (111) surfaces, respectively. Yellow atoms represent magnesium, blue is aluminum, red is oxygen, purple is potassium and silver represent platinum.*

In the configuration shown in Figure 5.10, the Pt is atomically dispersed, consistent with AC-TEM images, XRD, and LEIS data. However, these single atoms are not exposed, consistent with the failure to detect them in LEIS. On the other hand, the K atoms are exposed, hence LEIS result is consistent with the DFT calculations.

5.6 Conclusions

The spinel by itself cannot stabilize the single atoms Pt because it lacks stabilizing sites subsequently, form large Pt particles. Therefore, it needs additive such as K to stabilize the Pt atoms. AC-STEM observation suggests that spinel can stabilize Pt atoms using K as a stabilizer. However, these single atoms Pt are not exposed to truly surface-sensitive technique LEIS suggests that these atoms do not reside on the surface of the spinel but doped somewhere in the spinel or surrounded by potassium ions. DFT result suggests that the Pt atom is embedded inside six K atoms making it invisible to LEIS. In this structure, there are six potassium atoms binding with the central Pt atom through oxygen ligands to form single-atom-centric Pt sites. The central Pt binds with the adjacent four oxygen atoms and forms a square planar geometry, making the Pt atoms highly stable. The calculated binding energy of Pt on $K_6O_4(OH)_2$ cluster is -10.4 eV, which is significantly larger than the cohesive energy of Pt, thus providing a stable form of single Pt atoms on spinel.

CHAPTER 6: ENGINEERING CATALYST SUPPORTS VIA ATOM TRAPPING TO MODIFY THE NUCLEATION AND GROWTH OF METAL OXIDE CLUSTERS

6.1 Abstract

The size and morphology of the active phase (metal or metal oxide) are critical for the performance of heterogeneous catalysts. Conventional approaches for catalyst synthesis involve modification of pore size and structure, the use of ligands to anchor the metal during preparation, or the use of nanostructured oxides with well-defined facets to provide suitable sites for metal nucleation and growth. However, these approaches may not yield durable catalysts for high-temperature applications, such as the treatment of unburnt methane from natural gas-fueled engines. Here we demonstrate an approach that relies on the trapping of metal single atoms on the support surface in the thermally stable form to modify the nature of deposited metal oxide clusters. By anchoring Pt ions on the catalyst support we can modify the morphology of the deposited phase. As shown here, we can cause the formation of 2-D rafts of Pt instead of 3-D metal nanoparticles. After high-temperature treatment, the 2-D rafts transform into Pt nanowires on the engineered catalyst support due to the preferred orientation, in contrast to randomly oriented particles seen on conventional supports. Adopting this approach for the synthesis of bimetallic catalysts, we added Pd to the atom-trapped catalyst support and found that the resulting Pd/Pt@CeO_2 catalyst provides improved thermal stability and water tolerance during methane oxidation. We attribute the improved performance to the morphology of the PdO phase present on the atom-trapped catalyst support. The results show that atom trapping could represent an important addition to the toolkit of catalyst designers to engineer catalyst supports for

controlling the nucleation and growth of metal and metal oxide clusters in heterogeneous catalysts.

6.2 Introduction

The control over the size and morphology of clusters and nanoparticles is important for achieving optimum performance.[76] There are limited means available for catalyst designers to influence the nature of the active phase, especially when the catalysts are subjected to elevated temperatures. The most widely used approach for industrial catalysts involves adsorption of the metal salt precursor on an oxide support, via the methods of solubility limit or strong electrostatic adsorption (SEA).[77] Using these approaches, it is possible to achieve atomic dispersion of the deposited metal on several catalyst supports.[78,79,80] Here the interaction between the metal salt precursor and the functional groups on the surface (hydroxyls) determines the surface concentration of the dispersed phase. The nature and morphology of the dispersed phase depend on the surface structure of the oxide support[81,82], which can be manipulated by using faceted oxides as support, or by introducing ligands on the support.[83] By pre-calcining the support, the number of hydroxyls on the support can be changed, which allows some control over the metal deposition (Scheme 6.1a). However, once the catalyst is treated at high temperatures, the mobility of the deposited metal leads to thermodynamically stable structures, where the influence of the initial preparation steps is lost. Here we explore an alternate approach where we trap metal atoms on the support to modify the nucleation and morphology of the dispersed phase (Scheme 6.1b). Since the trapped metal atoms are stable at high temperatures, we can generate a catalyst suitable for high-temperature reactions such as methane oxidation.

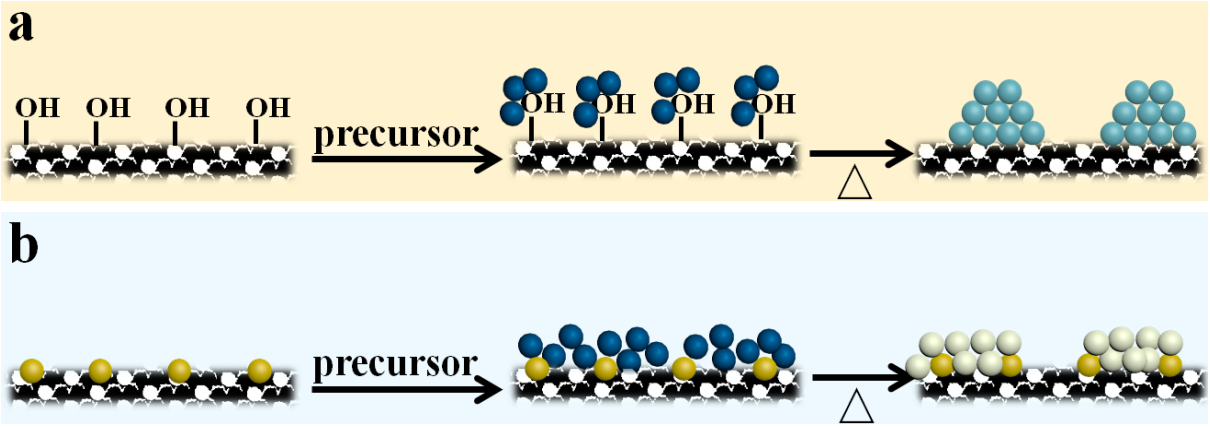

Scheme 6.1 | ***Trapping atoms on the support allows modification of the deposited metal oxide phase. A*** *conventional preparation method for heterogeneous catalysts where a metal salt adsorbs on surface functional groups and yield randomly oriented particles after calcination in air.* ***Sky blue and cyan spheres represent metal ions absorbed after drying and metal atoms after calcining, respectively. b,*** *the catalyst support prepared by atom trapping affects the nucleation of the dispersed phase leading to the formation of 2-D rafts which are stabilized by the trapped atoms in the support. Yellow, sky blue, and ivory spheres present trapped single atoms, metal ions deposited after drying, and metal atoms after calcining, respectively.*

Methane combustion catalysis is becoming increasingly important because of the widespread use of natural gas as a clean fuel for vehicles and power generation. Pd-based catalysts are the most active for methane oxidation, however, they suffer from rapid deactivation due to the presence of H_2O and due to sintering of the Pd phase.[84] Due to the excess O_2 present in the reactant stream, the stable phase of Pd under reaction is PdO. The sintering of Pd catalysts under steam is ascribed to the formation and migration of mobile Pd-OH entities in the presence of H_2O molecule[85], which are strongly adsorbed on the PdO surface. The binding of H_2O to the PdO also causes poisoning of the surface sites for

methane oxidation.[86] The surface coverage of CH_4 in the presence of water vapor is limited to only 3% of the saturation coverage of a pure CH_4 layer on PdO (101).[87] In our previous work, when Pd catalysts were reduced prior to reaction, we observed enhanced low-temperature reactivity.[88] Similar enhanced reactivity due to the pre-reduction of Pd catalysts has been reported by other workers.[89] We attribute this higher reactivity to a different form of surface Pd oxide formed on the metal core of the reduced Pd catalyst. This is consistent with DFT calculations which show that a surface oxide is more active than bulk PdO nanoparticles.[90,91] However, when Pd based catalysts are used for methane combustion, the metal Pd nanoparticle transforms to PdO with a resulting loss in catalytic activity.[92] A well-known approach for improving the stability and reactivity of Pd based catalysts is to add Pt. The addition of Pt into Pd catalysts changes the Pd species from PdO to bimetallic PtPd and keeps the Pd phase in a metallic state under oxidizing conditions[93], which is resistant to adsorption of water molecules. However, the bimetallic PtPd catalysts are not as resistant to sintering as PdO catalysts, leading to the formation of large alloy PtPd particles (> 20 nm) showing declined catalytic reactivity.[8,88] Therefore, there is an urgent need to develop methods to form an active PdO phase which is resistant to H_2O poisoning and catalyst sintering.[94]

In this work, we demonstrate the use of atom trapping[1,43,95] (high-temperature vapor-phase synthesis), to modify and engineer the catalyst support to achieve a different form of dispersed PdO which is thermally-stable and more resistant to water poisoning. Our goal is to avoid the formation of single-atom Pd on the support since this form of the catalyst is not active for methane oxidation.[96] On the other hand, we also want to prevent the formation of large PdO particles since they are poisoned by water and lead to lower activity.

6.3 Experimental Details

6.3.1 Catalyst Preparation

CeO_2 support was prepared by calcinating $Ce(NO_3)_3 \cdot 6H_2O$ at 350 ˚C for 2 h in air. For engineered CeO_2 ($Pt@CeO_2$ prepared by atom trapping with Pt loadings of 1, 2, and 3 wt.%, BET surface area: ~33 m^2/g), tetraamineplatinum nitrate solution was firstly impregnated onto CeO_2 powder by conventional wet impregnation, followed by drying at 120 ˚C for 12 h. Then, the material was calcined at 800 ˚C for 10 h in flowing air.[1,57] The obtained materials are denoted as $1Pt@CeO_2$, $2Pt@CeO_2$, and $3Pt@CeO_2$, corresponding to the Pt loading of 1, 2, and 3 wt.%, respectively.

CeO_2 and the engineered $Pt@CeO_2$ are used to load Pt and Pd catalysts. For Pt deposited on atom-trapped $1Pt@CeO_2$, an appropriate amount of tetraamine platinum nitrate ($Pt(NH_3)_4(NO_3)_2$) (2 wt.%Pt) was impregnated to the atom-trapped $Pt@CeO_2$ by wet impregnation, followed by drying at 120 ^oC for 12 h and calcining at different temperatures (500 ^oC, 600 ^oC, and 800 ^oC) in air. The total Pt loading is 3 wt.% and the obtained material was denoted as $2Pt/1Pt@CeO_2$. For Pd catalyst supported on engineered support ($Pd/Pt@CeO_2$), palladium nitrate was impregnated to the $Pt@CeO_2$ by wet impregnation, followed by drying at 120 ^oC for 12 h and calcining at 500 ^oC for 4 h in air. Reference samples of Pd/CeO_2 and $PdPt/CeO_2$ containing the same moles of metal as $Pd/Pt@CeO_2$ are prepared by conventional wet impregnation. The Pd/CeO_2 catalyst was prepared by impregnating the appropriate amount of palladium (II) nitrate solution precursor on the CeO_2 powder and drying at 120 ^oC for 10 h, followed by calcining at 500 ^oC for 4 h in flowing air. For the reference $PtPd/CeO_2$ catalyst (BET surface area: 67 m^2/g). Palladium (II) nitrate solution was impregnated onto the CeO_2 firstly and dried at 120 ^oC in the air for

12 h. After calcination at 500 ^{o}C in the air for 4 h, tetraamineplatinum nitrate (2 wt.% Pt) was impregnated onto the material progressively, followed by drying at 120 ^{o}C for 12 h in air and calcining at 500 ^{o}C for 4 h in air.

6.3.2 Catalyst Characterization

Aberration corrected scanning transmission electron microscopy (AC-STEM) was carried out using a FEI Titan Themis transmission electron microscope. AC-TEM image was recorded in a FEI Titan (300 keV), equipped with the Gatan K2-IS camera. The sample powders were deposited on holey carbon films after being dispersed in ethanol. The single Pt atoms on CeO_2 can be seen in the AC-STEM dark field images. Low energy ion scattering (LEIS) was used to quantify the concentration of Pt atoms on the catalyst surface. This technique selectively detects the topmost atoms and was carried out using an IONTOF Qtac100 instrument.[16] The dedicated LEIS instrument equipped with a double toroidal analyzer for the energy analysis of the backscattered ions and the analyzer has a large solid angle of acceptance (full 360° azimuth), while the scattering angle is fixed at 145°. In combination with parallel energy detection, this gives a high sensitivity while maintaining the mass resolution. He^+ and Ne^+ with ion energy 3 and 5 keV and current 5 and 2 nA, respectively, are used to analyze the surface concentration of Pt^{2+} ions in the catalysts. The area scanned per sample by these two ions was 2 × 2 mm^2 and the ion flux given to the samples was 1.4×10^{14} ions/cm^2 and 2.8×10^{13} ions/cm^2 respectively. The spectra for the Pt reference were analyzed within a 1.5 × 1.5 mm^2 sputter crater over an area of 1 × 1 mm^2. The analysis time was adjusted such that the surface damage was the same as for the other spectra. Assuming a sputter coefficient of 0.1 for He and 1 for Ne, this will lead to surface damage of 1% and 2% at the end of the analysis. X-ray photoelectron spectroscopy (XPS)

was performed using a Kratos Axis Ultra photoelectron spectrometer equipped with a monochromatic Al Kα source operating at 300 W. The base pressure was 2.7×10^{-8} Pa and the operating pressure was 2.7×10^{-7} Pa. Analysis of the XPS spectra was performed using CASA XPS software. X-ray Adsorption spectroscopy was performed at the materials research collaborative access team (MRCAT) bending magnet and insertion devise lines of the advanced photon source, Argonne national laboratory. Measurements at the Pd K edge were performed in transmission mode using a set of 3 ion chambers which allowed for concurrent measurement of a Pd foil energy reference. Samples for transmission mode measurement were prepared by pressing catalyst powder into a stainless-steel sample holder. The holder was placed inside a quartz tube reactor with Kapton windows and valves for gas flow. Samples were scanned at room temperature in the freshly calcined state and after reduction at 200 ^{o}C in 3.5% H_2. Measurements at the Pt L_3 edge were performed in fluorescence mode using a Lytle detector with a zinc foil filter used to reduce background fluorescence. Fluorescence samples were pressed into a stainless-steel sample holder and placed in a water-cooled in-situ cell equipped with Kapton windows, resistive heaters, and valves for gas flow. Samples at the Pt L_3 edge were measured in the freshly calcined state, at room temperature after reduction at 200 ^{o}C in 3.5% H_2, and at room temperature after reduction at 380 ^{o}C in 3.5% H_2. Data analysis was performed using WinXAS software. Experimental phase and amplitude functions for Pt-O, Pd-O, Pt-Pt, and Pd-Pd scattering were extracted from $Na_2Pt(OH)_6$, $Pd(OAc)_2$, Pt foil, and Pd foil respectively. Phase and amplitude functions for Pt-Pd and Pd-Pt scattering were constructed using FEFF with the amplitude reduction factor, Debye-Waller factor, and E_0 correction fixed to the foil value for the respective absorber so that the fit values of the Debye-Waller factor and E_0

correction are relative to the foil value. The bond distance for the Pt-Pt and Pt-Pd scattering was taken as the sum of the atomic radii of each metal. At the Pd K edge, k_2 weighted data were Fourier transformed over a k range of 2.7-11 $Å^{-1}$. The as-received samples were fit over an R range of 1-1.9 Å, and the reduced samples were fit over an R range of 1.3-2.9 Å. At the Pt L_3 edge, for the as-received samples, k_2 weighted data were Fourier transformed over a k range of 3.0-11.0 $Å^{-1}$. For the reduced Pd-Pt samples, the Fourier transform was taken from 2.7-11 $Å^{-1}$, a shorter data range was used for the Pt-Pd samples of 2.8-10 $Å^{-1}$. Reduced samples were fit from 1.2-3.2 Å. Fitting was accomplished in R space spectra on isolated first shell scattering, allowing the bond distance, coordination number, Debye-Waller factor, and E_0 correction to vary. The Debye-Waller factor was further refined on isolated first shell k space data. For bimetallic samples, the bond distance and Debye-Waller factor were constrained to be equal for the monometallic and bimetallic paths.

6.3.3 Methane Oxidation Measurement

Catalytic methane (CH_4) combustion was performed using a fixed bed flow reactor. 60 mg of catalyst powders were diluted by 600 mg SiC to guarantee the isothermal conditions. The catalyst bed was packed between two quartz wool plugs inside a ½ inch (I.D.) quartz tube. The reaction was performed at atmospheric pressure. The reaction gas consisted of 680 ppm CH_4, 14 vol % O_2 and 5 vol % CO_2 balanced with N_2 with a total flow of 300 mL/min. Different concentration of steam (H_2O) was introduced by flowing reaction gas through a temperature-controlled bubbler. The effluent gas was analyzed by an online MKS equipped with a detector. For light-off measurements, the samples were heated from room temperature to 650 ^oC with a ramp of 5 ^oC/min in reaction gas. After each light-off test, the

system was cooled down in a O_2/N_2 atmosphere. Stability under different dry/wet conditions was also evaluated by time-on-stream measurements.

6.4 Results and Discussion

6.4.1 Engineering of the Catalyst Support via Atom Trapping

In this work, we are using the approach of atom trapping to prepare the catalyst support (Fig. 6.1a). This involves the deposition of a Pt precursor (1 wt% Pt) on the ceria support firstly and heating to 800 ^oC in the air for 10 h. Since the Pt is present in atomically dispersed form, we will refer to this support as $1Pt@CeO_2$. When we deposit an additional 2 wt% Pt on this engineered support we find unusual morphologies of the Pt phase (Fig. 6.1b-d and Appendix III, Supplementary Figure III.1). The added Pt does not form atomically dispersed species as is typically seen on ceria supports.[16,19] Clearly, the method of atom trapping has eliminated the sites on which the deposited Pt could form atomically dispersed species. Instead, we see the formation of 2-D rafts as shown in Fig. 6.1b-d and Appendix III Figure III.1 (labeled by both boxes and arrows). The edge-on views confirm the 2-D nature of the deposited Pt and the top-down views show the size of the Pt domains to be ~1 nm. EXAFS measurements of this catalyst (Appendix III, Figure III.2, and Table III.1) confirm that this catalyst contains oxidized Pt but no Pt-Pt neighbors, i.e. not Pt clusters. We will refer to this as $2Pt/1Pt@CeO_2$ which, as shown next, is very different from a metal or oxide cluster.

The CO oxidation reactivity for this $2Pt/1Pt@CeO_2$ catalyst (containing a total of 3 wt% Pt) is greater than a 3Pt@ceria prepared via atom trapping and also a 3wt% Pt/CeO_2 catalyst prepared via conventional catalyst preparation (SEA) (Fig. 6.2a). This is in agreement with a recent work showing that a Pt_8O_{14} (Pt-O-Pt sites) is more active in CO oxidation.[97] Low

Energy Ion Scattering (LEIS, Appendix III, Table III.2), which is exquisitely surface sensitive, shows that the apparent Pt concentration on the 2Pt/1Pt@CeO_2 catalyst (2.2 atoms/nm^2) exceeds the surface concentration we reported previously on atom-trapped 3Pt@CeO_2 (~1 atom/nm^2).[16] The surface concentration detected by LEIS exceeds the expected surface concentration calculated based on the Pt content and the BET surface area (Appendix III, Table III.2). We attribute this higher apparent Pt concentration to the preferred orientation of the support which develops pronounced CeO_2 (111) surface facets and the presence of the Pt 2-D rafts on these surface facets. The surface concentration of Ce on the CeO_2 (111) facet is 7.9 atoms/nm^2.[17] The Pt surface concentration of an oxidized Pt foil is 9.01 atoms/nm^2. Therefore, the observed surface concentration of 2.2 atoms/nm^2 is consistent with the presence of 2-D Pt rafts on ceria (111) surface facets.

The engineered catalyst support is different from one prepared simply by heating the ceria support to 800 ^oC. As shown in Appendix III, Figure III.3, heating ceria causes a loss in surface area of the support, which is prevented by the presence of Pt during the high-temperature treatment (800 ^oC, 10 h). The Pt interacts with surface sites on the ceria and is trapped and helps to modify the nature of the additional Pt deposited on the support. This is revealed by comparisons of the 2Pt/1Pt@CeO_2 and a 3 wt% Pt/pre-sintered CeO_2. After the calcination at 800 ^oC in air, the former catalyst shows Pt forming nanorods and wires having a preferred orientation (Appendix III, Figure III.4), while the latter catalyst yields randomly oriented Pt particles (Appendix III, Figure III.5).

In summary, our results show that the engineered catalyst support prepared via atom trapping templates the deposited Pt oxide leading to the formation of 2-D rafts. As we will

show later, this catalyst support also prevents the redispersion of Pt preventing the formation of single atoms of Pt when the catalyst is heated in air at high temperatures.

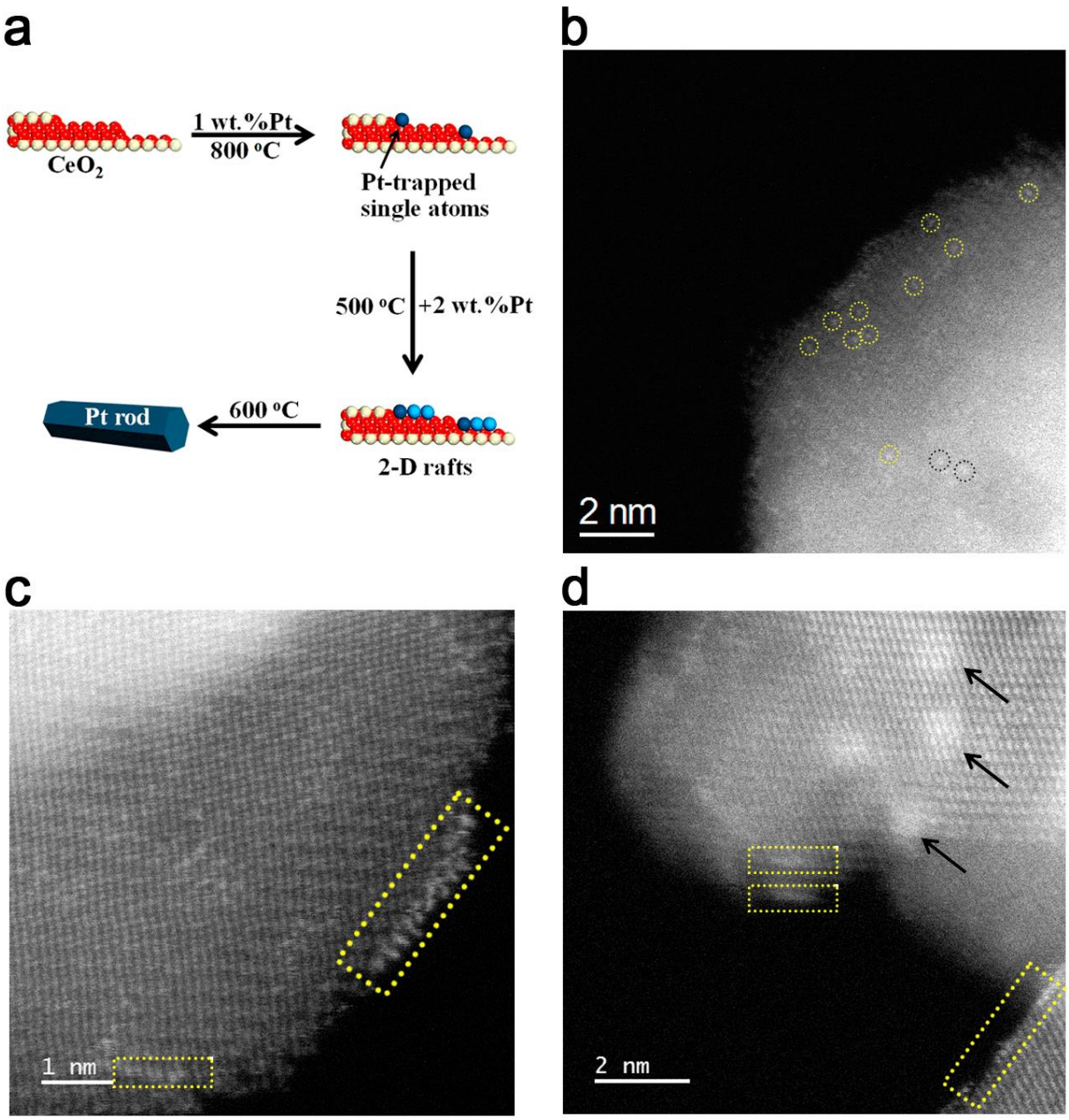

Figure 6.1 ***Electron microscope images of 2-D rafts of Pt on Pt@CeO₂. a*** *Schematic illustration showing the morphologies of Pt catalysts supported on ceria prepared by depositing Pt onto Pt-trapped ceria. The Pt atoms were labeled with different colors to*

emphasize the two steps in preparation. ***b,*** *AC-STEM image of 1 wt.%Pt@CeO_2 prepared by atom trapping showing atomically dispersed Pt indicated by circles.* ***c,d,*** *AC-STEM images of the catalyst prepared by depositing 2 wt% Pt on atom trapped 1wt% Pt@CeO_2. Edge-on views* ***(c,d)*** *indicated by squares show that Pt forms 2-D rafts which are approximately 1.5 nm in diameter as seen in top-down views indicated by arrows marked* ***(d)****. The uniform contrast of the particles in* ***(d)*** *confirms that these are not three-dimensional nanoparticles, which is a result of the modification of the catalyst support via atom trapping.*

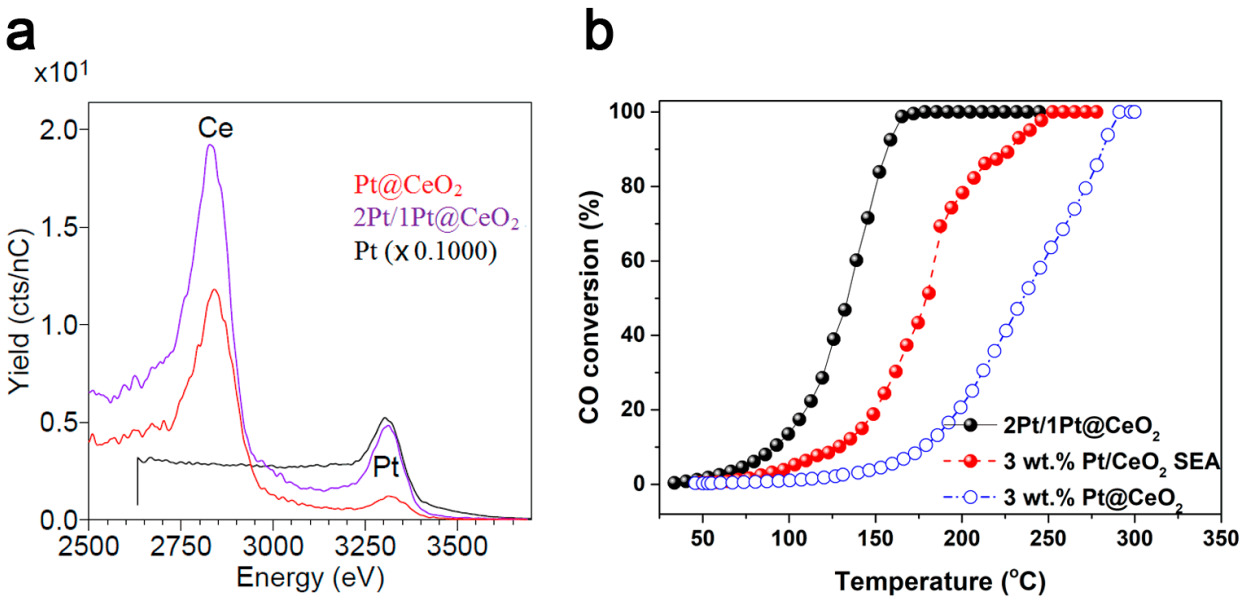

Figure 6.2 *Low Energy Ion Scattering (LEIS) and CO oxidation reactivity of Pt deposited on the engineered catalyst support. a, LEIS spectra of atomically dispersed 1Pt@CeO_2 and 2Pt/1Pt@CeO_2, the latter sample contains 2-D rafts of Pt as shown in Fig. 1. b, The CO oxidation reactivity confirms that the altered morphology of the Pt leads to enhanced CO oxidation reactivity. The 2-D Pt rafts are more active than the conventional Pt catalyst (3 wt% Pt/CeO_2 calcined at 500 °C for 4 h) prepared by impregnation and the atom trapped*

catalyst 3Pt@CeO_2. These three catalysts contain the same amount of Pt, the differences in reactivity can be attributed to different interaction with the support.

6.4.2 Methane Oxidation on Pd Deposited on the Engineered Catalyst Support

Inspired by the above observations and results, we deposited Pd on engineered Pt@CeO_2 support (Pt loading: 2 wt.%) and tested it for methane oxidation. The performance of this catalyst (Pd/Pt@CeO_2, Pd: Pt atomic ratio=1:1) was compared with other catalysts on the same ceria support containing the same amount of metal atoms (PtPd/CeO_2, Pt/CeO_2, and Pd/CeO_2). The reactivity was measured in a fixed bed reactor using a gas mixture that resembles that encountered during methane oxidation from vehicular exhaust (680 ppm CH_4, 14 vol % O_2, 5 vol % CO_2 balanced with N_2 with a total flow of 300 mL/min). For some of the experiments, we added water vapor to investigate the water tolerance of these catalysts. The light-off curves show that the Pd/Pt@CeO_2 catalyst is more active than the Pt/CeO_2 and Pd/CeO_2 catalysts containing the same amount of the metal atoms under dry methane oxidation conditions (Fig. 6.3a). To test the catalyst stability with/without steam, methane oxidation was carried out at 500 ^oC and the conversion was kept between 90-100% by varying the space velocity (Fig. 6.3b and c). The Pd/Pt@CeO_2 catalyst did not suffer a significant loss of reactivity when switching from dry to steam-containing methane feeds (4% loss in 5 v/v% water and 15% loss in 10 v/v% water, Fig. 6.3b) and the reactivity recovered to the initial value after stopping water vapor flow. This shows an improvement in water tolerance for the Pd/Pt@CeO_2 catalyst. The slight drop of the reactivity for the long term run at 500 ^oC (Fig. 6.3c) is likely caused by water molecules produced in the reaction at the high conversion[98], as compared to a sharp drop of the reactivity for both Pt/CeO_2 and Pd/CeO_2. The superior reactivity and water-tolerance of the Pd/Pt@CeO_2

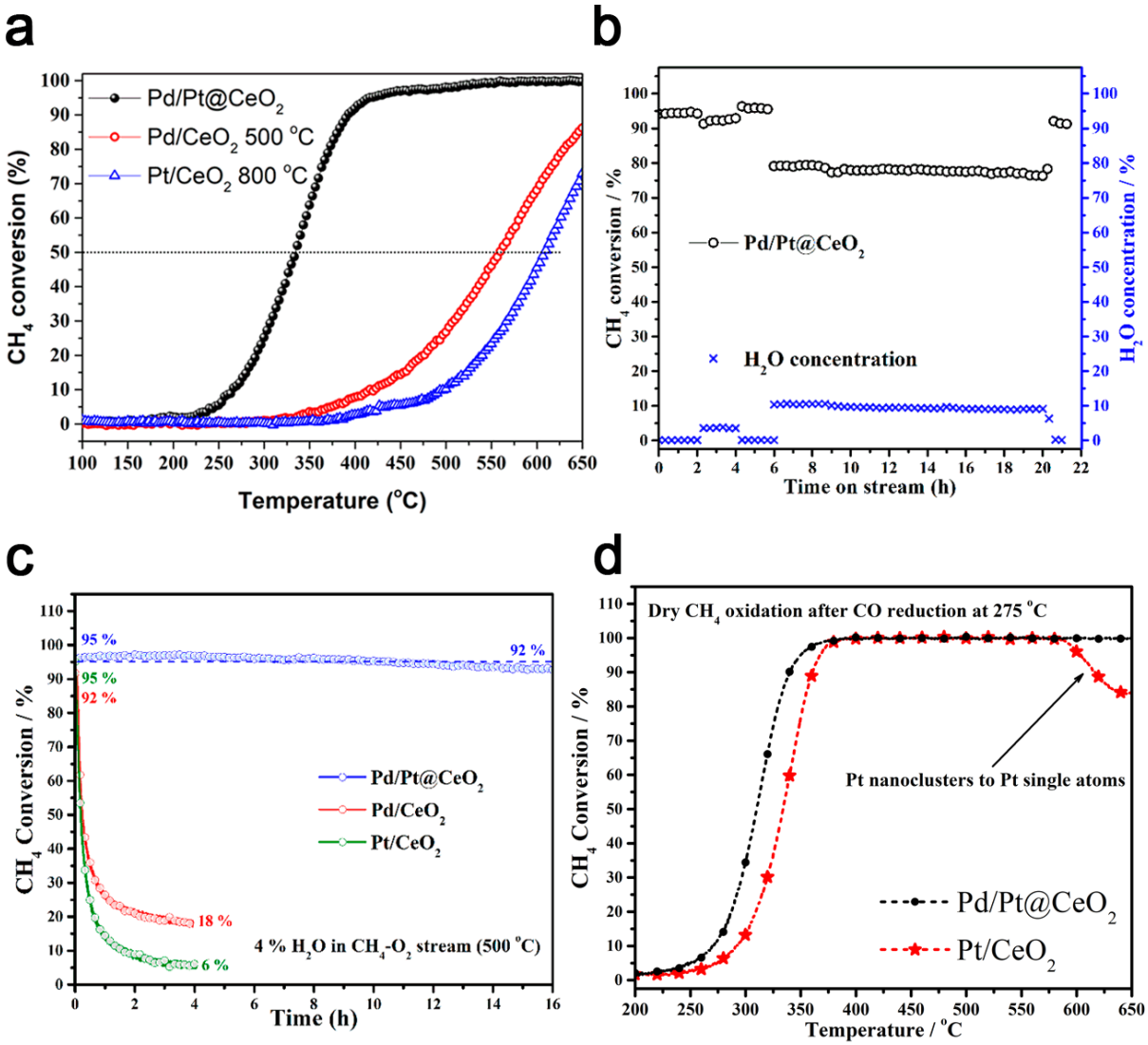

Figure 6.3 *Methane oxidation reactivity of Pd/Pt@CeO₂ and monometallic Pt and Pd/CeO₂ catalysts with/without the presence of water. The light-off curve of CH₄ oxidation under dry conditions over Pd/Pt@CeO₂, Pt/CeO₂, and Pd/CeO₂ catalysts. b, Time-on-stream measurements for CH₄ oxidation at 500 °C under different steam concentrations over Pd/Pt@CeO₂ catalyst. c, the comparison of catalyst stability for Pd/Pt@CeO₂, Pt@CeO₂, and Pd/CeO₂ catalysts in CH₄ oxidation at 500 °C in 4 % H₂O showing the excellent water-tolerance of Pd/Pt@CeO₂. d, light-off curves of CH₄ oxidation under dry*

conditions over reduced Pd/Pt@CeO_2 and Pt/CeO_2 catalysts. The reduced Pd/Pt@CeO_2 catalyst kept 100% conversion at the temperature of > 550 ^oC, while the pre-reduce Pt/CeO_2 catalyst showed decay in methane conversion when the reaction temperature is > 550 ^oC. This decay in reactivity is attributed to the transformation of Pt nanocluster on reduced Pt/CeO_2 to Pt single atoms under the oxidizing condition at elevated temperature.

catalysts were also confirmed in a different reactor setup for methane oxidation (2% CH_4, 5% O_2, and He as balance) (Appendix III, Figure III.6). As shown in Supplementary Figure 6.6, the Pd/Pt@CeO_2 catalyst showed a 2.7% loss of reactivity by switching from dry to steam methane oxidation (10 v/v% water), as compared to a 43% loss for Pd/CeO_2 at 380 ^oC. Likewise, the Pd/Pt@CeO_2 catalyst is stable at high reaction temperatures (> 550 ^oC) and no reactivity loss was present for the oxidized and reduced Pd/Pt@CeO_2 catalyst (Fig. 6.3a and Fig. 6.3d) when the methane oxidation temperature is higher than 550 ^oC, while the reduced Pt/CeO_2 sample shows the declined reactivity because the Pt nanocluster on reduced Pt/CeO_2 was transformed to Pt single atoms under the oxidizing condition at elevated temperature (Fig. 6.3d).

The AC-STEM characterization of the 2Pt@CeO_2 shows atomically dispersed Pt species are seen on the ceria support (circles in Fig. 6.3a), as also seen in both 1Pt@CeO_2 and 3Pt@CeO_2 reported in our previous study.[1,16] After depositing Pd species on the Pt@CeO_2 material, as shown in Fig. 6.3b, both single atoms, and rafts with an average diameter of ca. 0.8 nm are present (Fig. 6.3b and Appendix III, Figure III.7). We note that the single atoms seen in these images come from Pt and not Pd because the contrast of single-atom Pd on ceria is not sufficient to make them visible in AC-STEM images (atomic number of

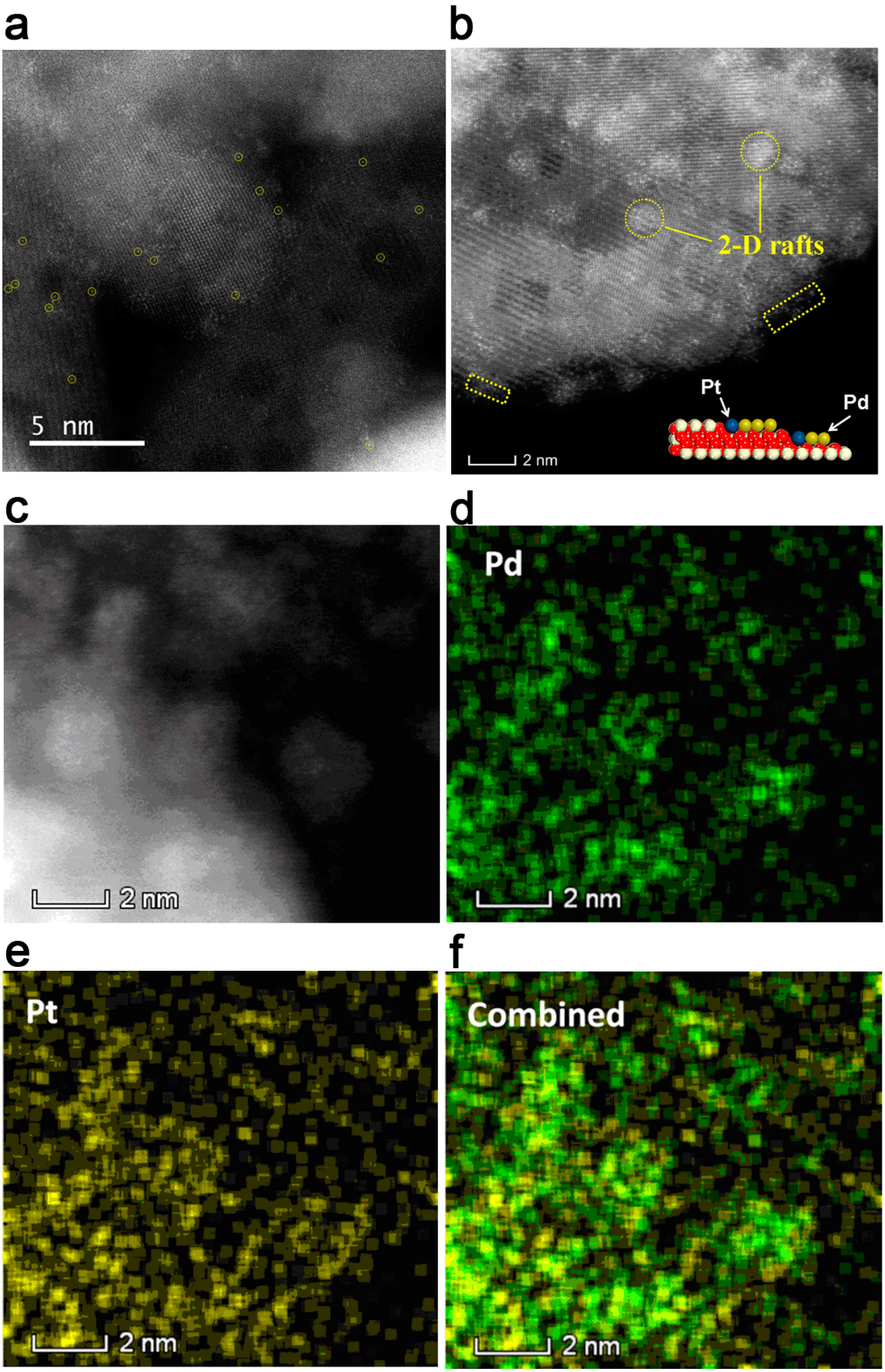
a
5 nm
b
2-D rafts
Pt
Pd
2 nm
c
2 nm
d
Pd
2 nm
e
Pt
2 nm
f
Combined
2 nm

Figure 6.4 ***AC-STEM images of 2wt% Pd deposited on atom trapped 1 wt% Pt/CeO_2. A,*** *AC-STEM image of 2 wt% Pt@CeO_2 prepared via atom trapping showing single atoms of Pt.* ***b,c,*** *AC-STEM image of 2wt% Pd deposited on the catalyst shown in* ***(a)****. 2-D rafts are visible which look similar to the 2-D rafts shown in* ***Fig. 1c****.* ***d,e,f,*** *STEM-EDS maps of this catalyst showing the Pd* ***(d)*** *and Pt* ***(e)*** *and the combined map indicating a uniform distribution of Pd and Pt in the rafts.*

Pd is lower than that of Ce, 46 vs 58). However, the Pd oxide clusters with weak contrast can be imaged on the ceria support. The high magnification STEM-EDS mapping (Fig. 6.3c-f) shows that both Pt and Pd are well dispersed on this catalyst and the homogeneous contrast in a domain indicated that the Pd domains are not 3D clusters, which generally show a brighter center. A schematic view of the morphology of the Pd oxide on Pt@CeO_2 is shown in the inset of Fig. 6.3b. The similarity in the image contrast of these Pd oxide domains to the Pt clusters shown in Fig. 6.1 allows us to assign these as PdO 2-D rafts which are present on the atomically dispersed Pt.

The atomic environment of the Pt and Pd atoms in the PdO 2-D rafts of the Pd/Pt@CeO_2 catalyst was examined by XAS measurements performed after oxidation and reduction (Fig. 6.5). The XANES spectrum of Pt edge of Pd/Pt@CeO_2 clearly shows that the Pt remains in the form of ionic Pt, which is similar to that on the Pt@CeO_2 catalyst (Fig. 6.5a).[57] The XANES spectrum of the Pd K edge of the fresh Pd/Pt@CeO_2 (Fig. 6.5b) revealed that the Pd phase is PdO, while it is slightly different from that of a reference PtPd/CeO_2 catalyst prepared by impregnation that the white line of Pd/Pt@CeO_2 is closer to that of Pd foil (Fig. 6.5b) than that of the reference PtPd/CeO_2, indicating the Pd species

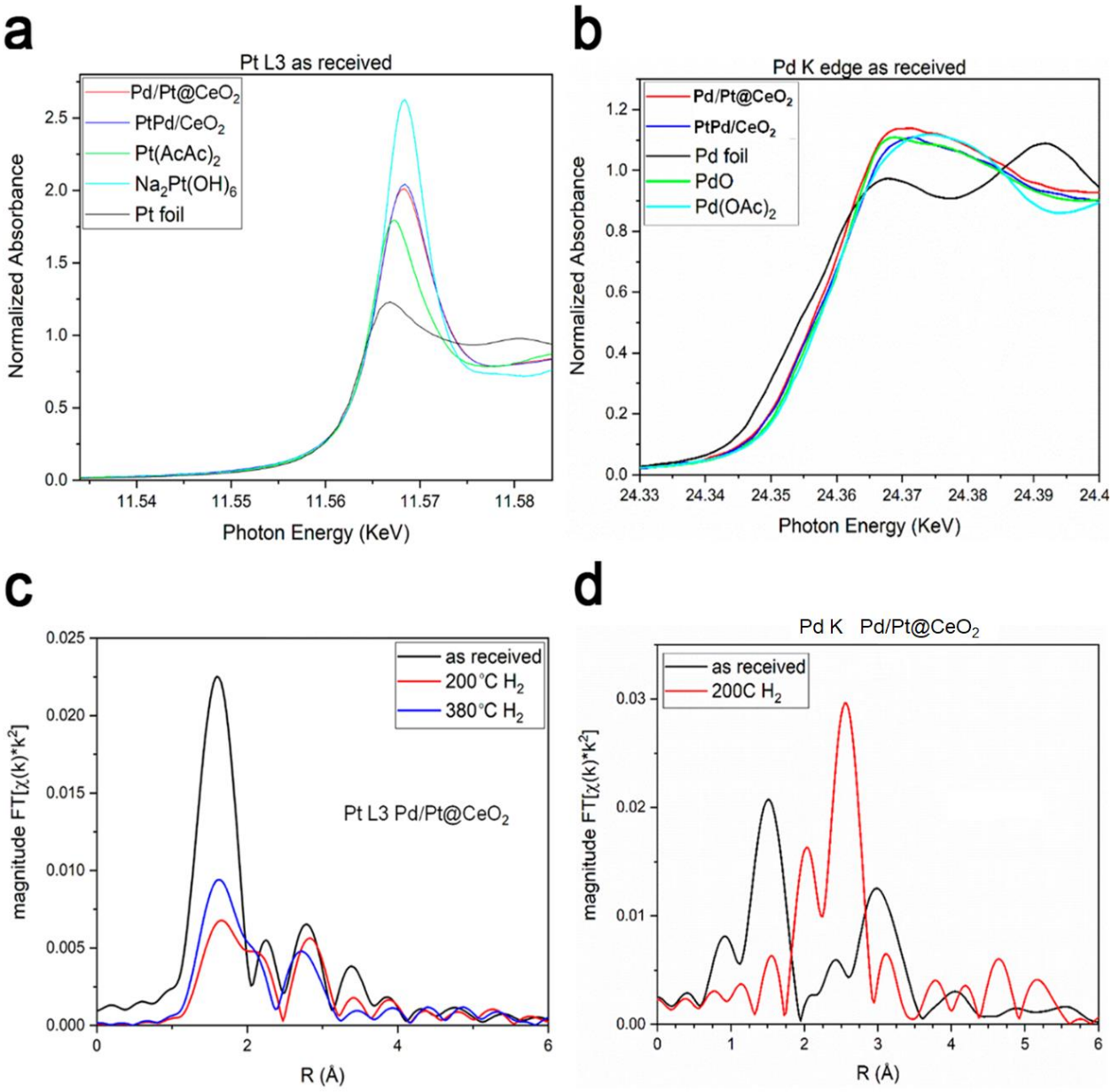

Figure 6.5 ***XAS spectra of Pd/Pt@CeO₂ and PtPd/CeO₂ samples****. **a,b,** XANES spectra of Pt and Pd edges of Pd/Pt@CeO₂. **c,d,** EXAFS spectra of the Pt L and Pd K edges of Pd/Pt@CeO₂ catalyst before and after in-situ reduction in H₂. The Pt and Pd standard samples were also measured.*

on the former is different from bulk PdO. The EXAFS data of the Pt L3 edge of the fresh Pd/Pt@CeO_2 is also similar to that of the fresh reference PtPd/CeO_2 catalyst, while the

spectra for the two samples are significantly different after a reduction treatment in H_2. After the reduction in H_2, ionic Pt species on the Pd/Pt@CeO_2 are still present (Fig. 6.5c), as compared to the complete disappearance of ionic Pt on the PtPd/CeO_2 catalyst

Table 6.1 XANES and EXAFS data for the samples.

EXAFS and XANES						
Sample	XANES Energy (keV)	Scatter	N	R, Å	$\Delta\sigma^2$ (x 10^3)	Eo, eV
References						
Pt Foil	11.5640	Pt-Pt	12	2.78	0	-0.2
$Na_2Pt(OH)_6$	11.5666	Pt-O	6	2.05	0	-0.3
$Pt(AcAc)_2$	11.5652	Pt-O	4	2.03	0	-0.3
Pt L_3 Edge						
2% Pt/CeO_2	11.5656	Pt-O	4.7	2.04	1.0	-0.4
PtPd/CeO_2	11.5656	Pt-O	4.8	2.04	0	-1.3
Pd/Pt@CeO_2	11.5653	Pt-O	4.9	2.04	0	-1.4
Pd K Edge						
PtPd/CeO_2	24.354	Pd-O	4.0	2.03	1.0	-1.2
Pd/Pt@CeO_2	24.355	Pd-O	4.0	2.05	1.0	-1.1
PdO	24.354	Pd-O	4.0	2.05	-	-
Pd foil	24.350	Pd-Pd	12	2.75	-	-

(Appendix III, Figure III.8), indicating that the ionic Pt on the Pd/Pt@CeO_2 is strongly trapped by the ceria support. This strong trapping is confirmed by CO-DRIFTS experiments that the reduced Pd/Pt@CeO_2 catalyst shows the higher intensity of the CO band on ionic Pt (Appendix III, Figure III.9).

Table 6.1 shows the first-shell coordination numbers for the Pd/Pt@CeO_2 catalyst and Pt, Pd references. Fitting the peak of Pt L3 of Pd/Pt@CeO_2 gives a coordination number of 4.9 at a bond distance of 2.04 angstroms. The catalyst has weak second shell scattering demonstrating that the Pt atoms are isolated as opposed to agglomerated in PtO clusters. Fitting the first shell of Pd K edge for Pd/Pt@CeO_2 gave a coordination number of 4 at a bond distance of 2.05 Å. An average Pd-O coordination number of 4 is consistent with Pd being present in the +2 oxidation state in the fresh catalysts. We used XPS to reveal differences in the Pd oxide on the Pd/Pt@CeO_2 compared to a reference PtPd/CeO_2 sample prepared by impregnation (Fig. 6.6). The Pt 4f spectrum of Pd/Pt@CeO_2 shows peaks at higher binding energy in comparison to that of the reference PtPd/CeO_2 (Fig. 6.6a), reflecting that the Pt species on Pd/Pt@CeO_2 is more ionic due to the prior trapping of Pt in ceria, which agrees well with the EXAFS and DRIFTS results. Likewise, the Pd 3d binding energy of Pd species on Pd/Pt@CeO_2 is lower than that of the reference PtPd/CeO_2 (Fig. 6.6b). It accounts for the presence of a different form of Pd oxide on the Pd/Pt@CeO_2 surface.

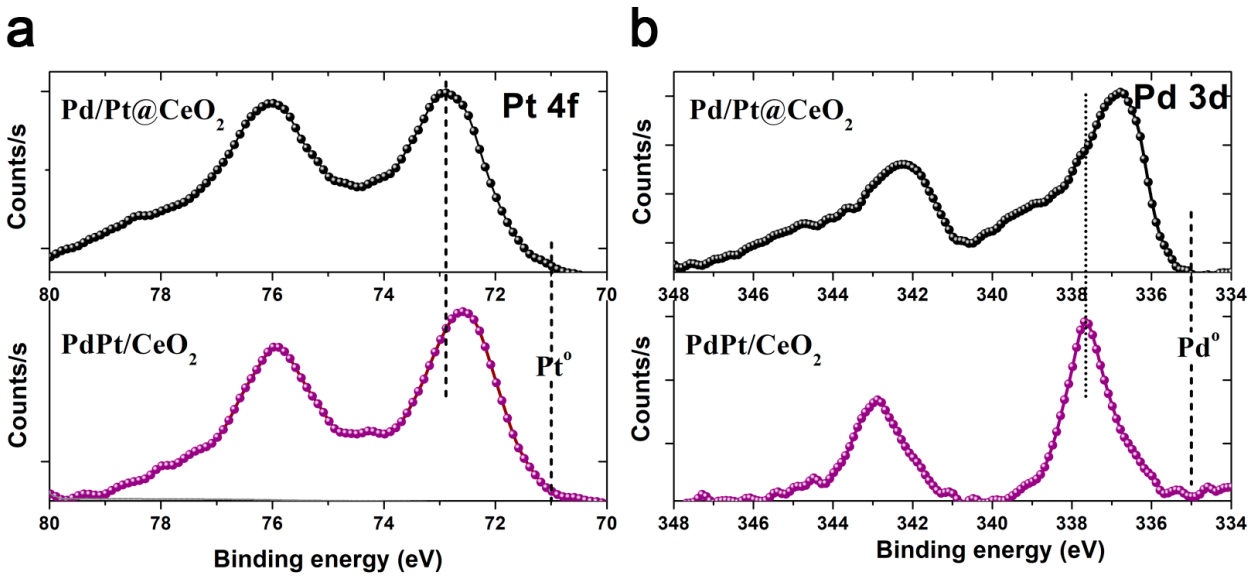

Figure 6.6 ***XPS spectra of Pd/Pt@CeO₂ and PtPd/CeO₂ catalysts. a,*** *Pt 4f XPS spectra of Pd/Pt@CeO₂ and the reference PtPd/CeO₂ catalysts.* ***b,*** *Pd 3d XPS spectra of Pd/Pt@CeO₂, and the reference PtPd/CeO₂ catalysts.*

Based on the above characterization results, we propose that the deposition of the Pd phase on atom trapped Pt@CeO_2 causes the formation of 2-D Pd oxide rafts which exhibit enhanced reactivity compared to the conventional Pt/CeO_2 and Pd/CeO_2 catalysts prepared via impregnation. The enhanced reactivity of 2-D Pd oxide rafts in methane oxidation is confirmed by DFT modeling (Fig. 6.7 c,d). A low activation barrier for the methane oxidation is seen on the 2-D Pd oxide rafts (in the model, a single layer Pd atoms bonded to O atoms of CeO_2 to form Pd oxide rafts), as compared to that on metal Pd and Pd oxide. Given the dissociation ability of water molecule on catalyst based on a DFT calculation, the exceptional water-tolerance of Pd/Pt@CeO_2 in steam methane oxidation (10%H_2O vapor) was explained (Fig. 6.7 a,b). Since the Pd oxide in Pd/Pt@CeO_2 is more metallic than that in other catalysts, we calculated the energy barriers of water molecule dissociation on PdO, metal Pd and 2D Pd rafts to illustrate the activation energy of water dissociation

on the catalysts prepared by different methods (Fig. 6.7a,b). The modeling result shows that water molecule is easily dissociated when locating on PdO sites, while it is thermodynamically unfavorable for the water molecule to dissociate on 2-D Pd oxide rafts (Fig. 6.7b). Thus, under steam conditions, the water molecule tends to occupy the PdO sites in Pd/CeO_2 catalyst prepared by impregnation, rather than the 2-D Pd oxide raft sites in the $Pd/Pt@CeO_2$ sample. Consequently, more active sites are available to activate the C-H band in methane oxidation for $Pd/Pt@CeO_2$, leading to higher reactivity in steam methane oxidation.

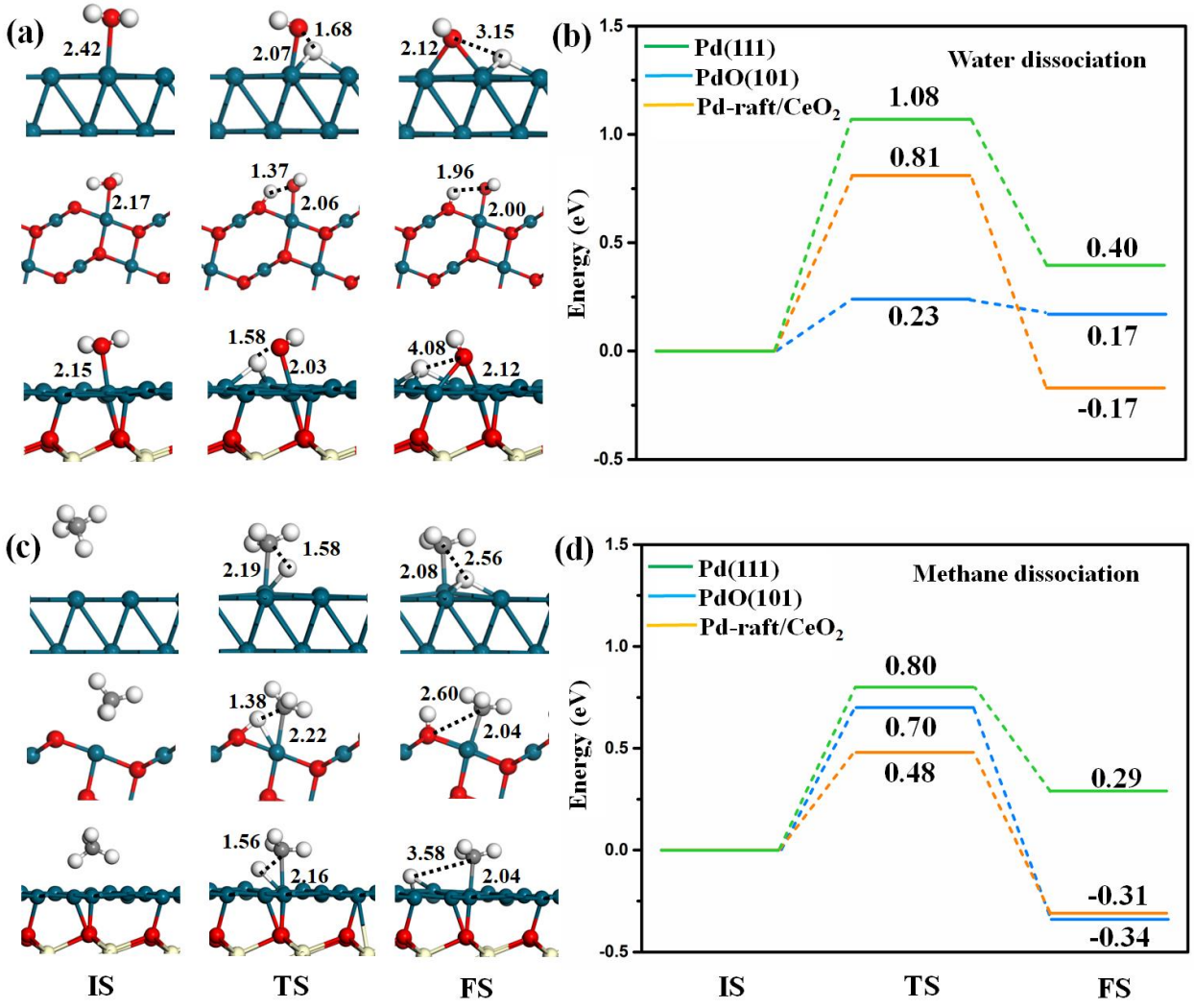

Figure 6.7. *DFT simulation for the energy barriers of water dissociation and methane oxidation over the metal Pd, PdO, and 2D Pd raft. a,b, Structure configuration, and the energy barriers of water dissociation over the metal Pd, PdO, and 2D Pd raft. c,d, Structure configuration, and the energy barriers of methane oxidation over the metal Pd, PdO, and 2D Pd raft.*

6.5 Conclusions

In this study, we used atom-trapped single atoms to modify and engineer the catalyst support to influence the nature of the deposited metal oxide. In the case of Pt deposited on atom-trapped Pt@CeO_2 (Pt/Pt@CeO_2), we found that 2-D Pt rafts were formed, the support formed prominent ceria (111) surface facets and the preferred orientation caused a higher surface Pt signal in LEIS. The 2-D Pt rafts showed higher reactivity in CO oxidation because of a weaker interaction between the Pt oxide and the engineered support. The catalyst with the strongest interaction Pt@CeO_2 had the lowest reactivity for CO oxidation. Using a similar atom trapping approach, we prepared a Pd/Pt@CeO_2 which showed much better reactivity than the conventional Pd/CeO_2 and Pt/CeO_2 catalysts containing the same moles of metal atoms in methane oxidation. Analogous to the case of Pt/Pt@CeO_2, aberration-corrected electron microscopy results showed that the Pd/Pt@CeO_2 catalyst presented PdO 2-D rafts with an average size of 0.8 nm as well as the presence of Pt single atoms. Further methane oxidation results under the addition of 4-10 v/v% steam show that the Pd/Pt@CeO_2 catalyst has improved water-tolerance in methane oxidation than a conventional Pd/CeO_2 catalyst, while both contain PdO phase. The superior water tolerance of the former catalyst is due to the presence of a different form of 2-D Pd oxide rafts on the engineered support via atom trapping. This work demonstrates that the approach of

atom trapping can be used to engineer catalyst support leading to improved catalytic performance of the deposited phase. We suggest this approach could be added to the tool kit of catalyst designers to develop improved catalysts where the behavior of the deposited phase can be modified by the trapped atoms in the support.

CHAPTER 7: CONCLUSIONS AND FUTURE WORK

Platinum-based catalysts are used to treat the exhaust emissions for diesel engines because of its outstanding oxidizing behavior, but they experience harsh conditions while in operations. USDRIVE Low-Temperature after treatment (LTAT) test protocol[2] recommends treating diesel oxidation catalysts at 800 ˚C under oxidizing conditions to make sure, they operate effectively throughout the lifetime of the car. Under these conditions, many papers in the literature documented that Pt-based catalysts deactivate readily and form a tremendously large Pt particle.[1,8] At this temperature under oxidizing conditions, Pt reacts with oxygen to form a volatile species PtO_2 which has a high vapor pressure.[3] The motivation for this work has instigated because of a desire to gain the fundamental insights into why and how Pt forms anomalously large particles and what is the mechanism responsible behind it? The goal of the first study in this dissertation was to investigate the anomalous growth of platinum particles during the accelerated aging of diesel oxidation catalysts and to propose a mechanism that is responsible for the formation of anomalously large Pt particles based on the experimental data we received. Based on our experimental shreds of evidence, we suggested that Pt particles grow due to vapor phase assisted catalyst sintering. The growth in Pt particle size causes a loss in effective surface area and catalytically active centers that result in catalyst deactivation. Model powder catalysts were used to get insights into the responsible mechanism for the anomalous growth of the Pt particle (chapter 3). In the first study of this dissertation, we observed a rapid loss of Pt from alumina ($La\text{-}Al_2O_3$) and spinel ($MgAl_2O_4$) supports when the catalyst was present in the form of a thin film. This is due to the inability of PtO_2 to bind strongly to $MgAl_2O_4$ and $La\text{-}Al_2O_3$. However, no Pt loss was reported via ICP-OES

when the bulk amount of catalysts aged in the ceramic crucible because the gas-phase PtO_2 condensed within the bed to form large Pt particles. The loss of Pt is attributed to the formation of volatile species PtO_2 via the reaction of Pt with oxygen at elevated temperatures. This leads to the growth of a few particles that continue to grow, fed by the high vapor-phase concentration of PtO_2. This work shows the importance of vapor-phase transport for the observed anomalous growth patterns.

To design the sinter resistance, durable and robust Pt catalyst, it is extremely important to mitigate the emission of PtO_2 and the formation of large Pt particles. The previous work[5] proved that adding Pd indeed lower the emission of Pt by capturing the volatile PtO_2 species when a Pt-Pd particle is heated. The emission of PtO_2 causes the formation of metallic core Pt-Pd and a separate PdO phase. This separate PdO phase has very low vapor pressure and traps PtO_2 and reduces to Pt-Pd bimetal and slows down the emission of Pt.[5] Similarly, in another separate study from the group showed that when the physical mixture of Pt/alumina and ceria was heated to 800 ˚C under oxidizing conditions, all the Pt migrated from alumina to ceria.[1] The experimental evidence showed that Pt volatilized to PtO_2 in an oxidative environment and got trapped into ceria in the form of single atoms. The second study of this dissertation was begun because of the desire to gain some fundamental understanding of atom trapping on ceria. Such as what is the upper limit of Pt metal loading in the form of single atoms as to ameliorate catalytically active center per unit area of support in order to make industrially relevant catalysts? What is the mechanism responsible for atom trapping? What are the sites responsible for atom trapping? Where does Pt atom locate, surface or subsurface or doped into the ceria? And What is the chemistry of Pt atoms with respect to ceria support?

The second study in this dissertation demonstrated that ceria is remarkably good support that allows trapping of ionic Pt keeping it atomically dispersed. In this dissertation, we demonstrated that high surface area ceria can support high metal loadings (~3wt%) in the form of single atoms which corresponds to 1atom/nm^2. The results of bulk elemental analysis combined with the BET surface area helps identify the upper limit for stabilizing atomically dispersed Pt to be 1 atom/nm^2. The under-coordinated Ce^{3+} cations at the ceria step edges react with PtO_2, sharing the oxygens provided by the Pt, to form strong covalent bonds that result in the thermally stable single atoms. The trapped single-atom Pt binds to the ceria (111) step edges strongly and prevents the formation of large Pt particles. The DFT computations show the stable site involves the binding of Pt to surface oxygen atoms at the ceria steps with an average distance of 2.04 Å which is confirmed by EXAFS measurements. The strong binding of the PtO_2 to step sites on CeO_2 (111) and the weak interaction with Pt oxide clusters leads to the exclusive formation of atomically dispersed Pt. The large Pt metallic particles show up when the sites responsible for atom trapping exceed the saturation. The combination of surface-sensitive spectroscopic techniques, LEIS, XPS, and DRIFTS, confirm that the Pt atoms are located on the surface of the ceria. The AC-STEM images are consistent with Pt and are bound to step edge sites on the ceria. This work shows that the single atom, ionic Pt, is not active for CO oxidation at low temperatures. Since the Pt is strongly bound to the support. In summary, using a high surface area commercial ceria and Pt precursor, we have demonstrated that high metal loading of platinum is possible in the form of single atoms that are thermally stable at elevated temperatures.

Reducible oxide supports such as cerium dioxide, titanium dioxide, and non-oxide supports such as carbon, MoS_2 are well-known supports for trapping the single atoms Pt. These supports have their pros and cons. For eg. Cerium is a rare earth's metal and its availability in the earth's crust is limited. Non-oxide supports such as carbon or MoS_2 has no or low thermal stability. The motivation of the third study in this dissertation was begun because of the desire to find the alternative for reducible oxide and non-oxide supports in trapping Pt atoms that is readily available, thermally stable, and industrially applicable. We found that spinel can stabilize Pt in the form of single atoms with the help of K additive. Density functional theory (DFT) was used to understand the role of potassium in the stabilization of single atoms Pt. DFT results suggest that single Pt atoms are embedded in stable $K_6O_X(OH)_Y$ clusters on the spinel surface. Such a scenario is consistent with the experimental data.

From our earlier study[60], we found that Pt binds weakly to the supports such as alumina and spinel. During the use, the catalyst experiences a harsh condition as a result anomalously large Pt particles are formed. On the contrary, in our other study,[16] we found that Pt atoms bind strongly to ceria (111) step edges making it less active for diesel oxidation catalysts. Therefore, it is extremely important to nucleate the Pt in catalyst support such a way that it can survive at high temperature and performs at a low temperature making it relevant to the industrial applications to overcome the energy crisis. The motivation for the fourth study in this dissertation is to control the nucleation of Pt through atom trapping. Here we demonstrated an approach that relies on the trapping of metal single atoms on the support surface in the thermally stable form to modify the nature of deposited metal oxide clusters. By anchoring Pt ions on the catalyst support, we can

modify the morphology of the deposited phase. We deposited Pt on the top on thermally stable Pt/ceria catalyst support to modify the nucleation and cause the formation of 2-D rafts of Pt instead of 3-D metal nanoparticles. The 2-D rafts of Pt on ceria has higher CO oxidation activity than that of Pt nanoparticles and Pt single atoms. When we deposited the palladium on the top of atom trapped ceria, the Pd changed its morphology to form a thin film of PdO. This thin film of PdO is highly active for methane oxidation reaction and is highly water tolerable.

Future work

In the first study of this dissertation, we documented that all the Pt escapes from alumina and spinel catalyst when the catalysts are spread in the form of thin-film and subjected to 800 ˚C in flowing air. Carrillo et al,[5] found that adding Pd helps to slow the emission of PtO_2 from the catalyst system. He studied the emission of PtO_2 in a model system but there has not been any study on the real catalyst powder. There are still open questions that need to be addressed and future work should involve a further study on the emission of PtO_2 on Pd containing catalysts powders to address the following questions.1) what should be the optimal atomic ratio of Pt to Pd for the extraordinary performance of the catalyst? 2) If we vary the atomic ratio of Pt to Pd, whether the emission of PtO_2 will be the same or different under certain experimental conditions? 3) What is the rate of emission of Pt from the bimetallic mixture of Pt and Pd? Future work should involve the implementation of a detailed experimental and theoretical model to help describe the thin catalyst powder studies for the emissions of PtO_2. It is always good to corroborate the experimental data with theoretical modeling and vice-versa. Mathematical modeling should be developed which predicts the emission of Pt and rate loss, and sintering with the addition of Pd. The

model should be validated using experimental data to make sure that the models correctly depict the process. The goal would be the use of EDX to quantify the loss of Pt from the thin film or thin bed system of the powder catalyst. Answering the above questions helps us to use the proper amount of each element and design the effective catalyst since both elements are an integral part of catalytic converters.

This dissertation has provided fundamental insights into the sites responsible for atom trapping on ceria and spinel. However, during the operating conditions, the single atoms catalyst experience harsh conditions, so Pt atoms become mobile and form a Pt nanoparticle. Future work should involve a further study to investigate the optimal temperature to disperse the Pt nanoparticle back to the single atoms for industrially relevant regenerable catalysts. The catalysts that contain Pt nanoparticles should be calcined carefully with increasing temperature under oxidizing conditions to find the optimal temperature that enables Pt nanoparticles redispersion to single atoms. This will not only allow Pt nanoparticles to redispersion but also burn off the deposited coke on the catalyst. This study can be done in the microscope resided in our facility. An additional thing to look at during this work would be 1) whether the Pt single atom goes to the same sites where it came from during the formation of a nanoparticle or not? 2) What microstructural changes occur during the redispersion of Pt? To address these questions *in-situ* atomic resolution microscope is needed.

In our study,[60] we found that ceria traps 1 atom/nm^2. This work has generated some fundamental interesting questions for the catalysis community, such as 1) why ceria traps only one atom/nm^2 2) Can we increase the trapping sites on ceria by incorporating other elements? 3) Does the pre-sintered ceria traps Pt atoms? 4) What happens to the ceria

trapping sites when bare ceria is subjected to elevated temperature? To address all the above questions experimentally, aberration corrected TEM is the utmost tool, and a DFT study is needed to support the experimental findings.

Appendix I: Supporting Data for Chapter 3

Table I.1. Shows the mathematical calculation for Pt loss in a deep boat and thin film at 800 ˚C.

	1wt% Pt 500 mg in a ceramic crucible	A thin layer of the sample in a silicon nitride wafer
Vapor pressure at 800˚C (atm)	1.6×10^{-08}	1.6×10^{-08}
Hours of aging	30	7
Moles of total gas during aging	8.036	1.875
The molecular weight of PtO_2	227	227
The upper limit of Pt vaporized during aging assuming saturated vapor (g)	2.92×10^{-05}	6.81×10^{-06}
Amount of Pt in the sample g	**[*]0.005**	**[$]$3.5\times10^{-07}$**
Percent of Pt in the sample lost if the gas was saturated in PtO_2	5.8%	>100%

*Amount of Pt in the sample placed in the ceramic crucible boat

The sample used was 500 mg

The Pt loading was 1 wt%

Amount of Pt in the sample (g) = 0.005

The vapor pressure of PtO_2 at 800˚C is calculated by using the following equation (C.B. Alcock, G.W. Hooper, Thermodynamics of the Gaseous Oxides of the Platinum-Group Metals, Proc. R. Soc. A Math. Phys. Eng. Sci. 254 (1960) 551–56).

$$log10Patm = \frac{-8585}{800 + 273.15} + 0.204$$

P=1.60×10^{-8} atm

$Moles\ of\ air\ during\ aging\ for\ 30\ hours = \frac{100\ sccm\times60\ min/hour\times30\ hours}{22.4\ L/mol\times1000\ ml/L}$=8.036 moles

$$Molecular\ weight\ of\ PtO_2 = 227\ \text{g/g mol}$$

$Weight\ of\ Pt\ lost\ assuming\ the\ air\ was\ saturated\ in\ PtO_2 = 8.036 \times 227\ (g/g\ mol) \times 1.60 \times 10^{-8}\ (mole\ fraction\ of\ Pt\ in\ air\ at\ saturation)$=$2.92\times10^{-5}$ g

$Total\ amount\ of\ Pt\ in\ the\ sample\ (g) = 0.5$ (gram of catalyst) × 0.01 (g Pt/ g catalyst)=0.005g

$Fraction\ of\ Pt\ lost\ if\ the\ air\ was\ saturated\ in\ PtO_2\ vapor = \frac{2.92\times10-5}{0.005}$=**0.0584**

The estimated loss of **5.84%** is below the detection limit of ICP-OES. Since we start with 1wt% Pt. The error bars for ICP-OES are about 10%.

[$]Estimation of the amount of Pt on the dispersed sample on a Silicon nitride wafer

Amount of Sample taken ~ 1mg

Wt: 1 wt% of Pt

Total # of drops that can be formed that contains the 1 mg of sample ~ 28 drops

Amount of Sample in 1 drop (mg) ~ 0.035 mg

Amount of Sample in 1 drop (g) ~ 0.035x10-3 g

Number of drops put on a wafer ~ 1 drop

Amount of Pt in 1 drop (grams of Pt) = 3.5×10^{-07} g

$Moles\ of\ air\ during\ aging\ for\ 7\ hours = \frac{100\ sccm\times60\ min/hour\times7\ hours}{22.4\ L/mol\times1000\ ml/L}$=1.875 moles

$$Molecular\ weight\ of\ PtO_2 = 227\ \text{g/g mol}$$

$Weight\ of\ Pt\ lost\ assuming\ the\ air\ was\ saturated\ in\ PtO_2 = 1.875 \times 227\ (g/g\ mol) \times 1.60 \times 10^{-8}\ (mole\ fraction\ of\ Pt\ in\ air\ at\ saturation)$=$6.81\times10^{-6}$ g

$Total\ amount\ of\ Pt\ in\ the\ sample\ (g) = 3.5 \times 10^{-5}$ (mg of catalyst) × 0.01 (g Pt/ g catalyst)=3.5×10^{-7}g

$Fraction\ of\ Pt\ lost\ if\ the\ air\ was\ saturated\ in\ PtO_2\ vapor = \frac{6.81\times10^{-6}}{3.5\times10^{-7}}$=19.45

This estimate shows that all of the Pt in the thin film can be lost after 7 hours of aging.

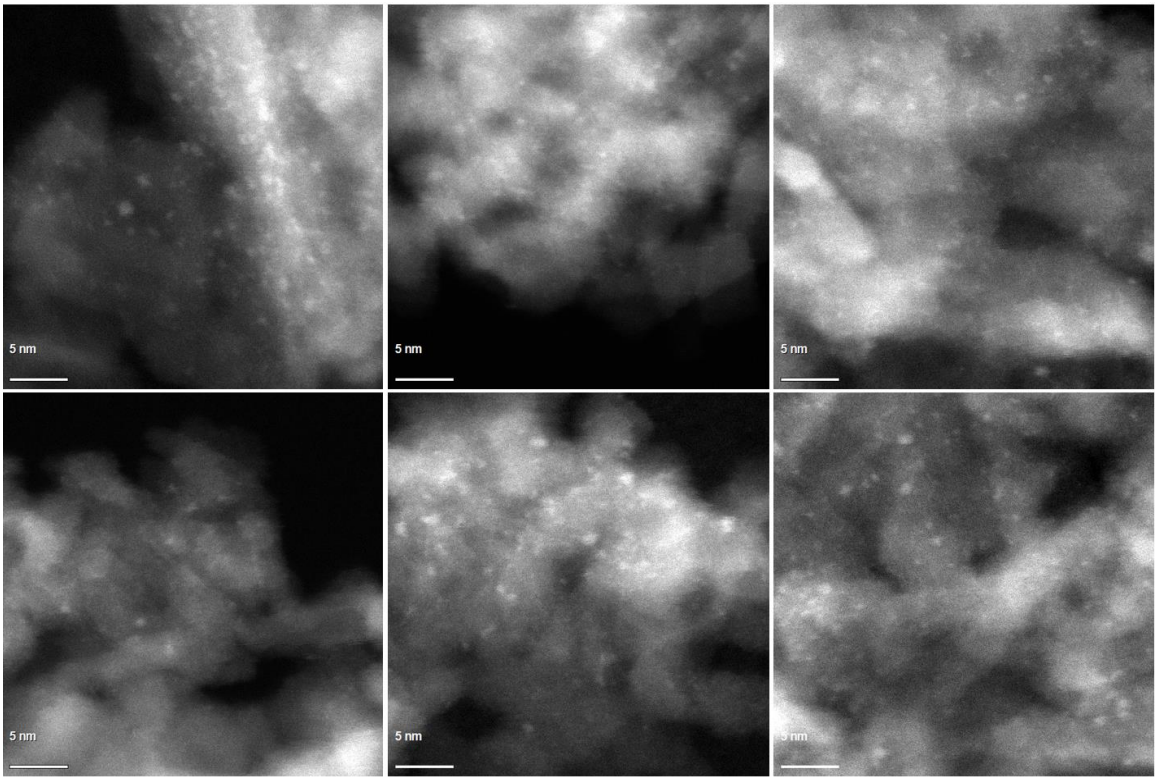

Figure I.1. *STEM images on initial (1wt%Pt/$LaAl_2O_3$ 550˚C/4h) catalyst.*

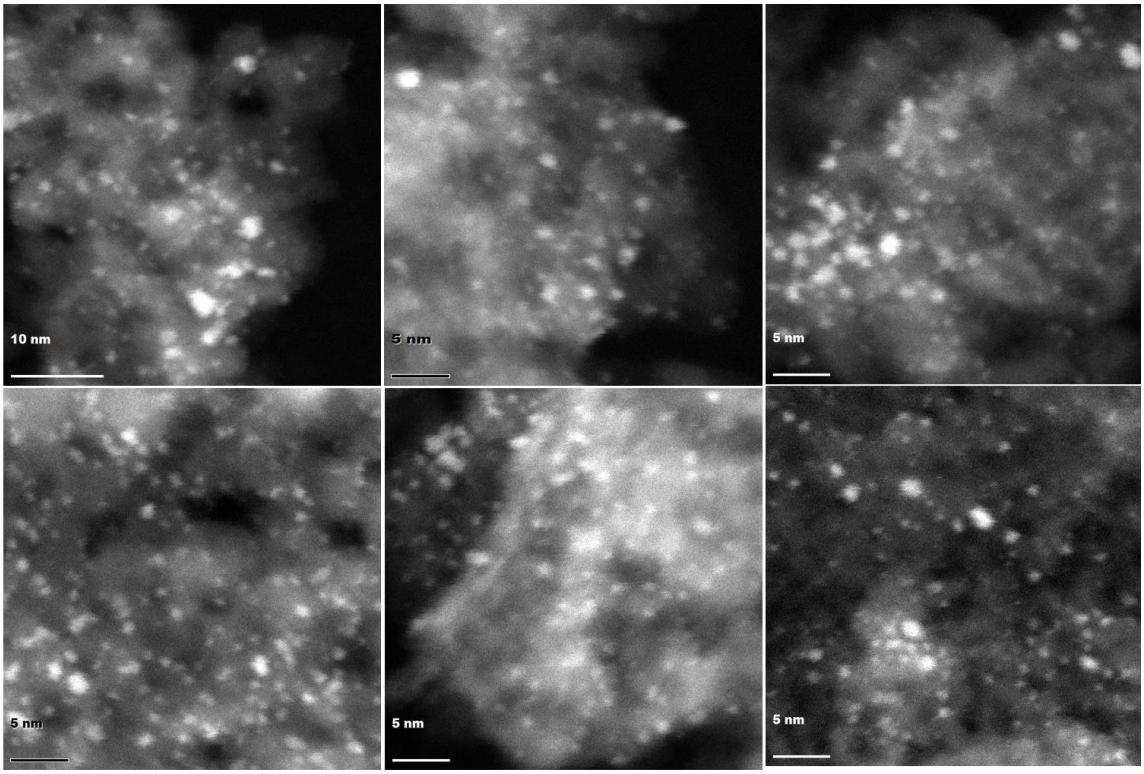

Figure I.2. *STEM images on initial (1wt%Pt/$MgAl_2O_4$ 500˚C/4h) catalyst.*

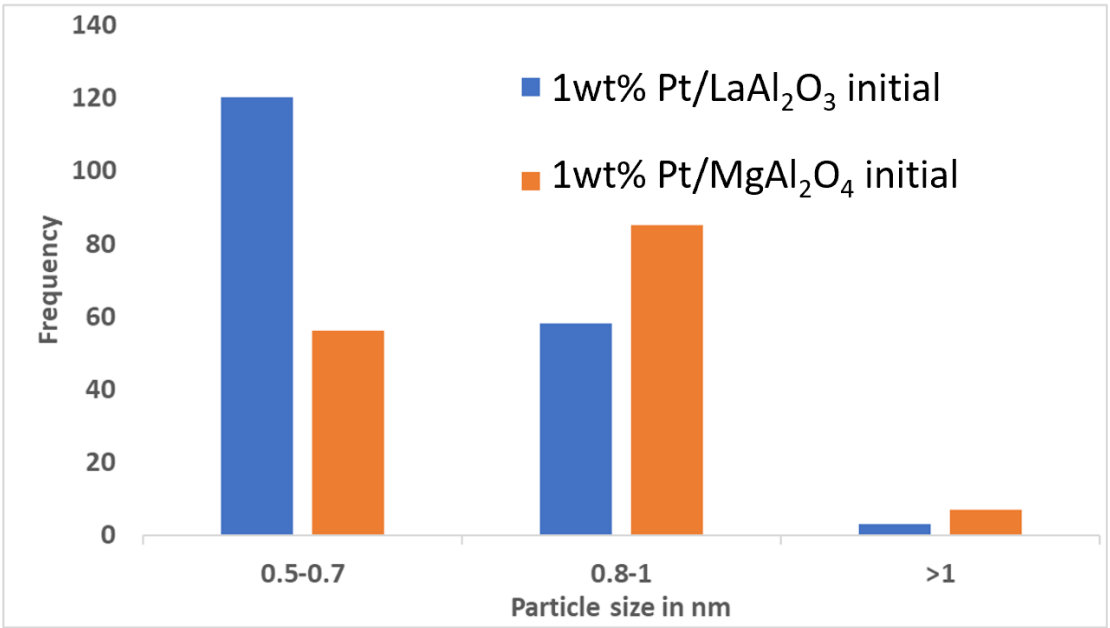

Figure I.3 *Particle size distribution via STEM on initial catalysts.*

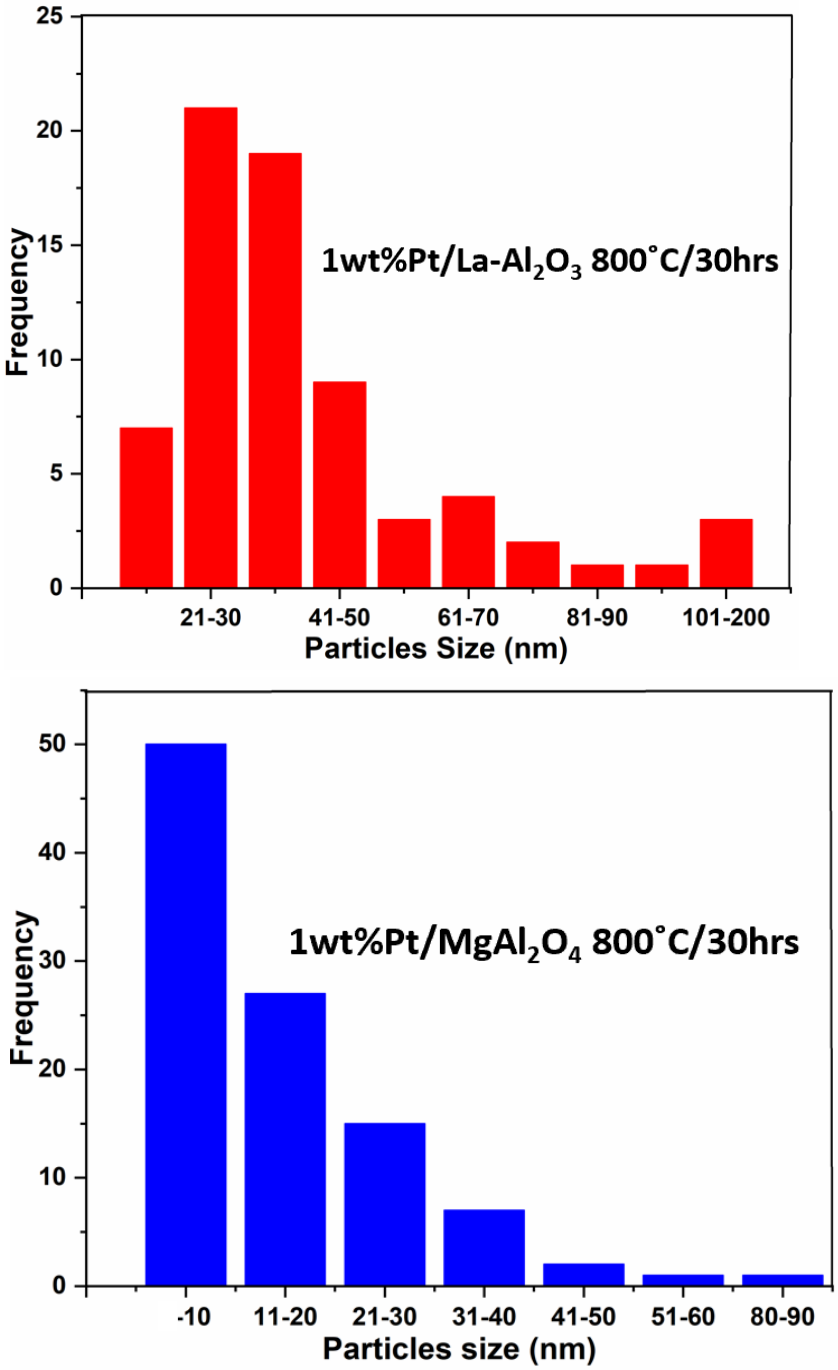

Figure I.4 *Particle size distribution via STEM on aged catalysts.*

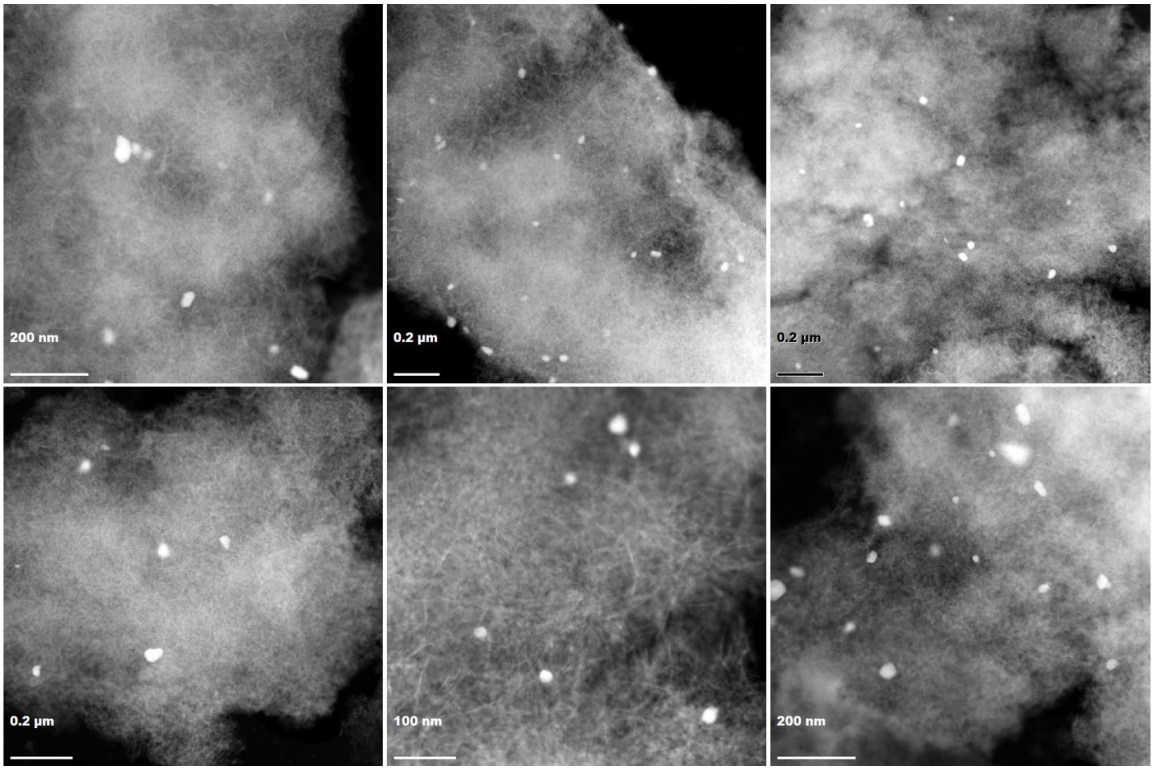

Figure I.5 *STEM images on aged (1wt%Pt/LaAl$_2$O$_3$ 800 ˚C/30h) catalyst.*

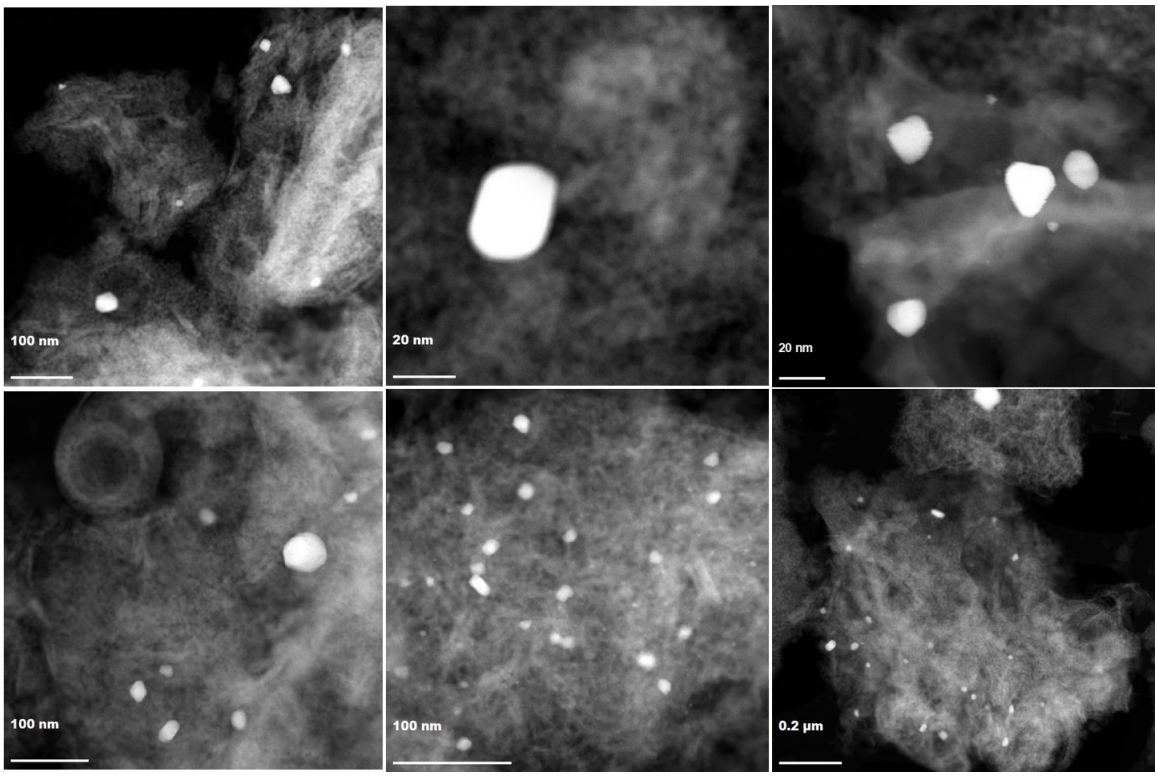

Figure I.6 *STEM images on aged (1wt%Pt/$MgAl_2O_4$ 800 ˚C/30h) catalyst.*

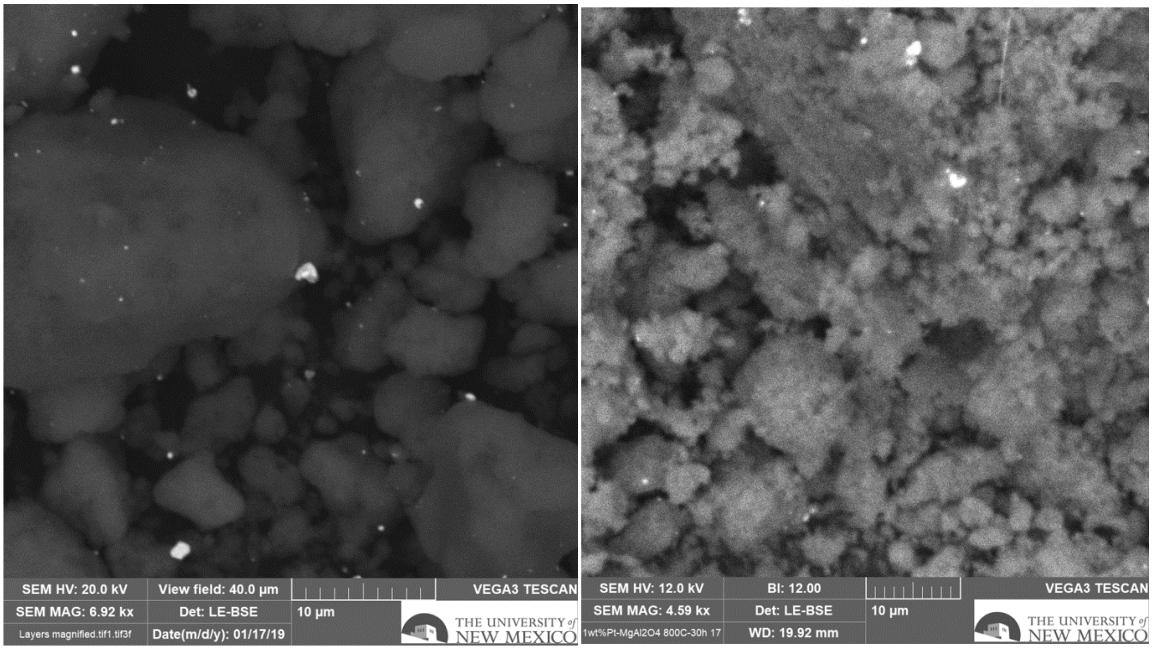

Figure I.7 *SEM images of 800 ˚C/30h aged Pt/$LaAl_2O_3$ and $MgAl_2O_4$ catalysts respectively.*

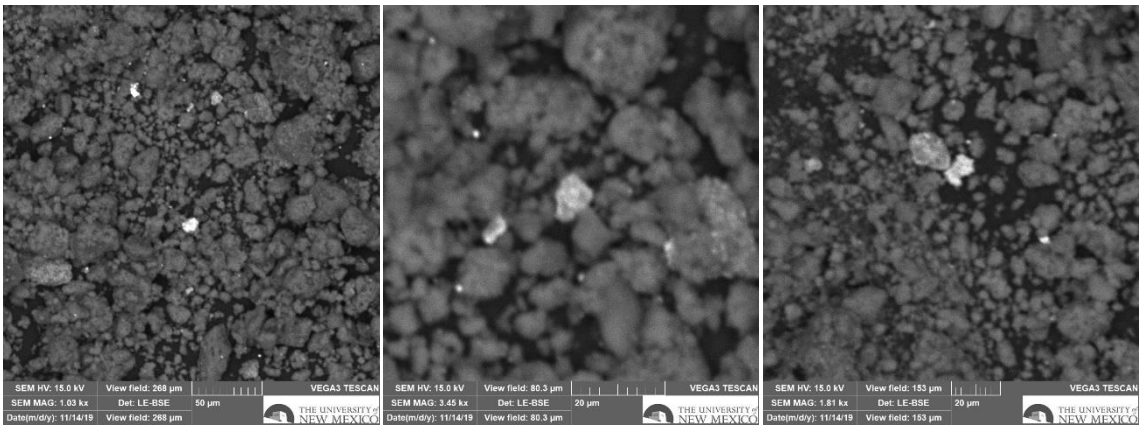

Figure I.8 *SEM images of 1wt%Pt/La-Al_2O_3 catalyst after aging at 800˚C for 4 hours in the presence of 10% steam.*

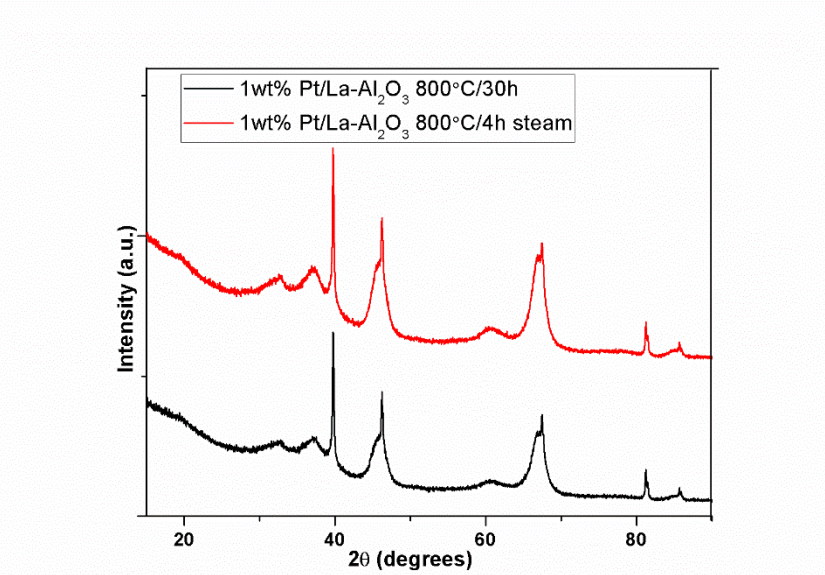

Figure I.9 *XRD pattern for 1wt% Pt/LaAl$_2$O$_3$ 800 ˚C with and without steam.*

Table I.2. Shows the comparison of 1wt%Pt/La-Al$_2$O$_3$ and 1wt%Pt/MgAl$_2$O$_4$ initial catalysts with literature.

Catalysts	TOF (S^{-1}) at 200˚C	#Reported in literature at 200˚C
1wt%Pt/La-Al$_2$O$_3$ initial	0.46	0.20-0.40 S^{-1}
1wt%Pt/MgAl$_2$O$_4$ initial	0.33	

#H. Wang, J. Dong, L.F. Allard, S. Lee, S. Oh, J. Wang, W. Li, Applied Catalysis B : Environmental Single-site Pt / La-Al 2O 3 stabilized by barium as an active and stable catalyst in purifying CO and C 3 H 6 emissions, 244 (2019) 327–339

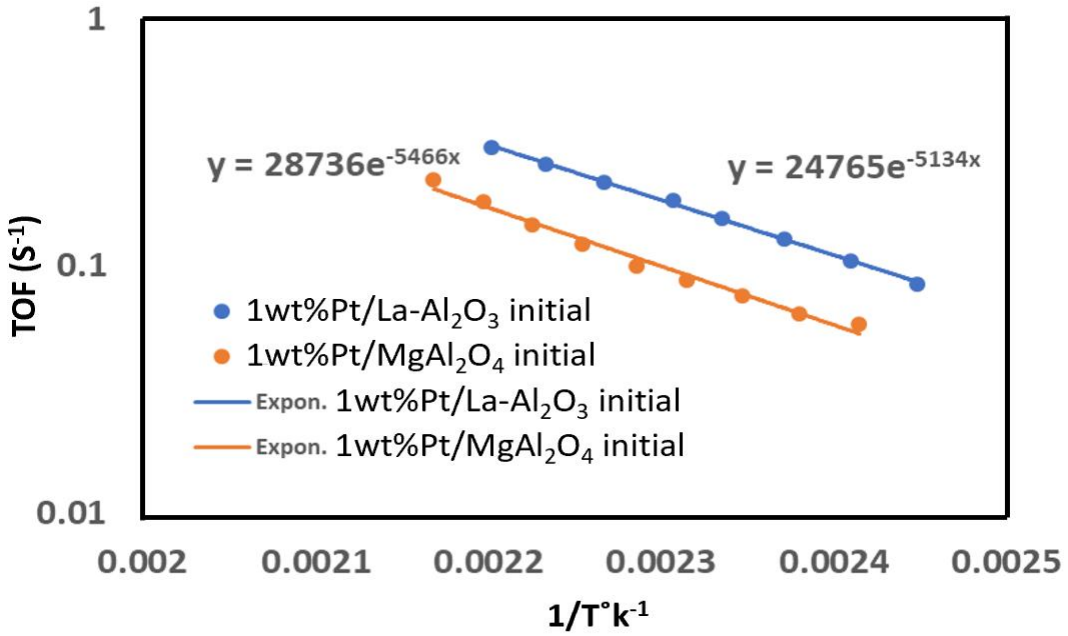

Figure I.10 *Arrhenius plot for the initial (1wt% Pt on La-Al_2O_3 and $MgAl_2O_4$) catalysts.*

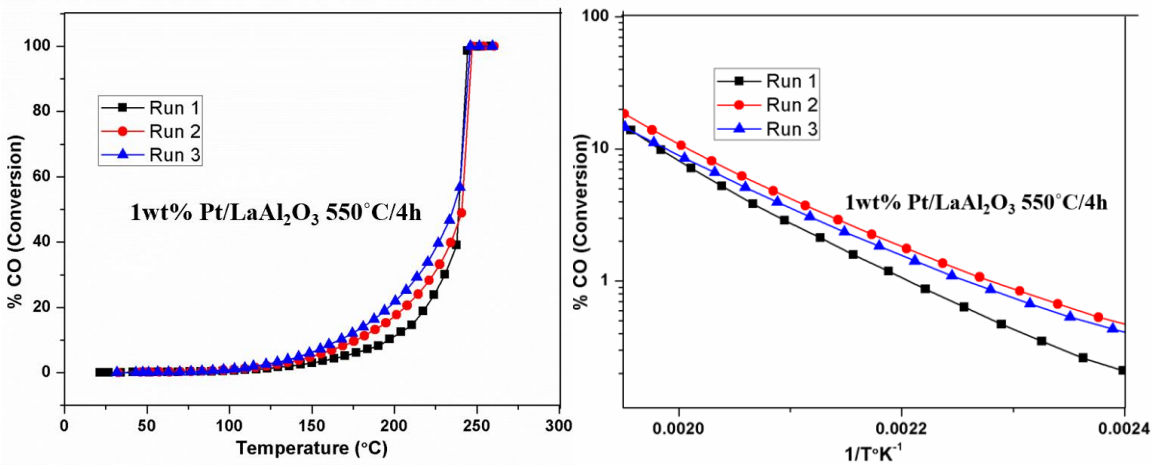

Figure I.11 *CO oxidation reactivity on initial (1wt% Pt/$LaAl_2O_3$ 550 ˚C/4h) catalyst shows multiple runs.*

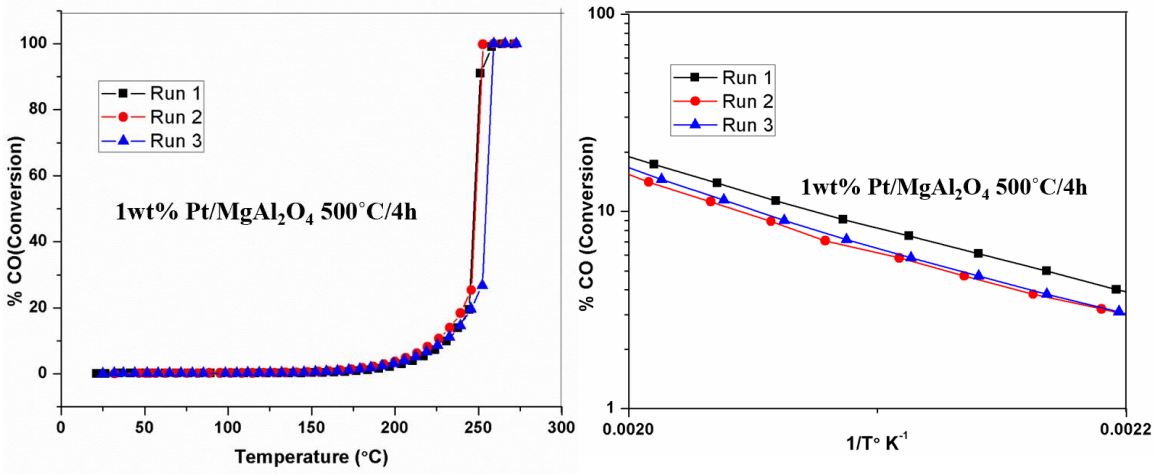

Figure I.12 *CO oxidation reactivity on initial (1wt% Pt/$MgAl_2O_4$ 500 ˚C/4h) catalyst shows multiple runs.*

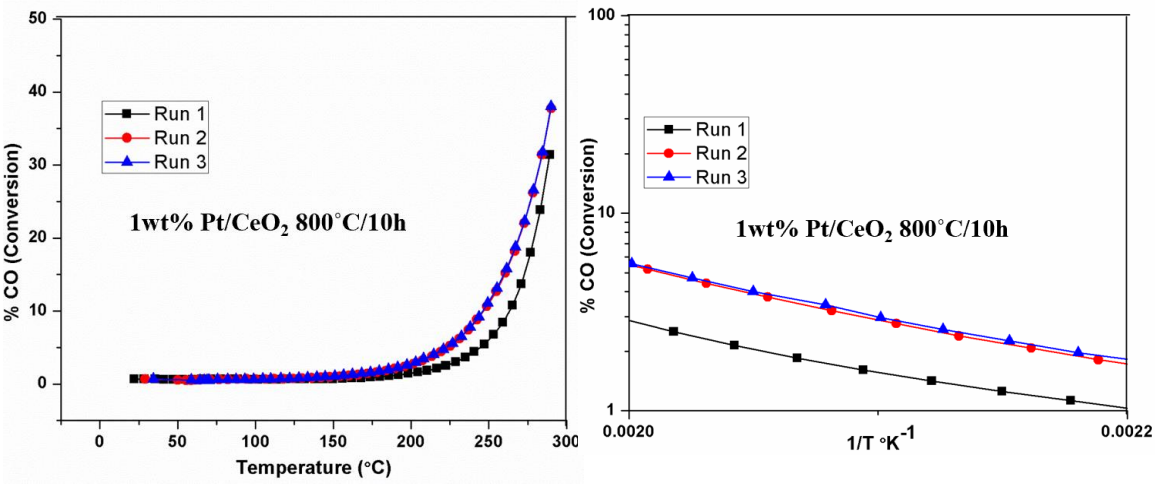

Figure I.13 *CO oxidation reactivity on initial (1wt% Pt/CeO_2 800 ˚C/10h) shows multiple runs.*

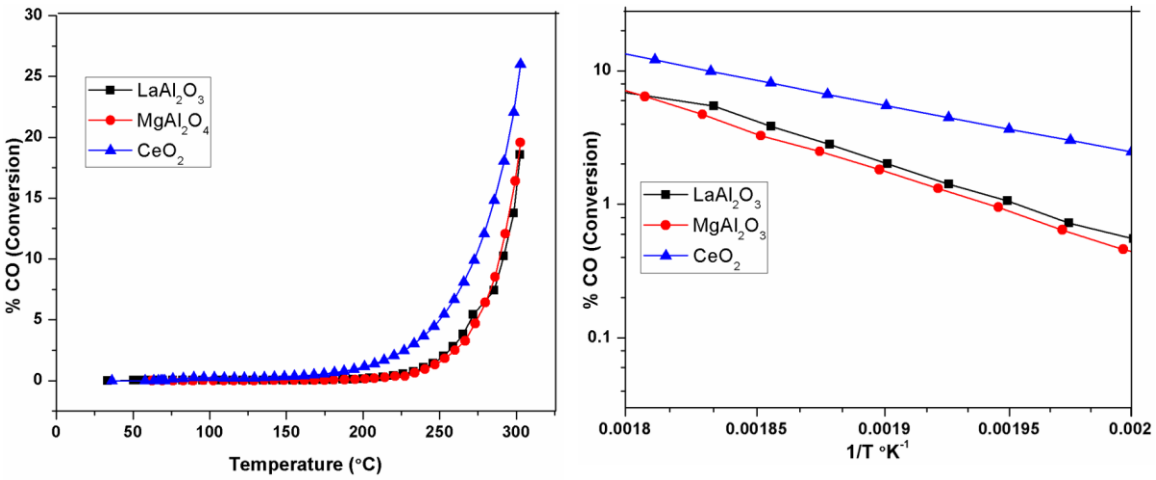

Figure I.14 *CO oxidation reactivity on catalyst supports as received.*

Appendix II: Supporting Data for Chapter 4

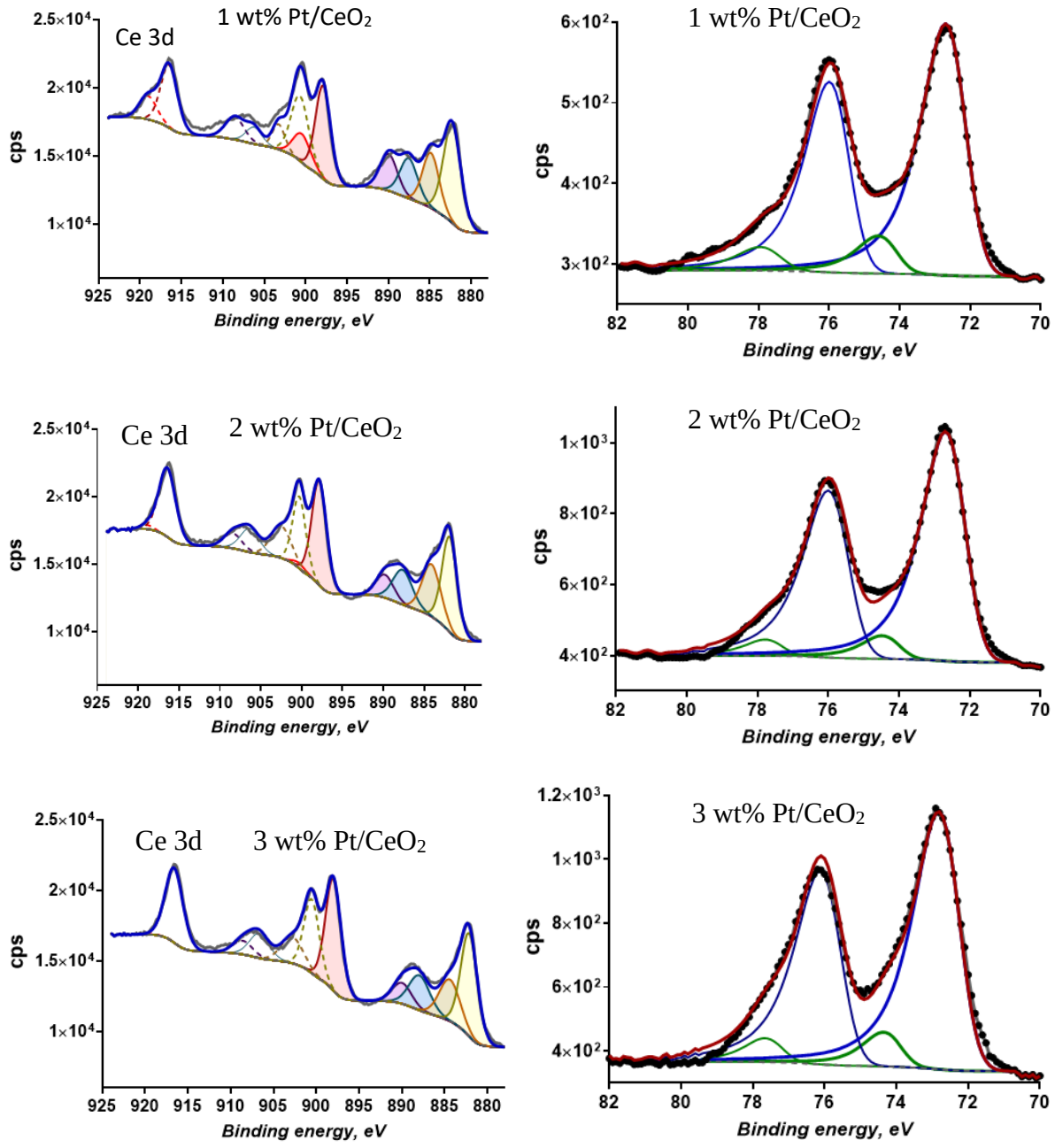

Figure II.1 *XPS analysis of the 1, 2, and 3 wt%. Pt/CeO₂ sample showing the Ce 3d region and the Pt 4f region shows that the Pt is in the Pt(II) oxidation state with a very small contribution from Pt(IV).*

Table II.1. Analysis of Ce and Pt peaks in the XPS spectrum of the air-treated catalysts containing 1, 2, and 3 wt% Pt.

	Binding Energy (eV) CeO_2						Pt (II)	Pt (IV)	Surface concentration & Pt/Ce ratio				
Samples	882.4	884.4	888.4	890.8	898.3	900.4	72.8	74.5	C 1S%	O 1s%	Ce 3d%	Pt 4f%	Pt/Ce
1 wt%	29.3	15.6	12.1	10.8	23.6	8.6	87.8	12.2	32.8	46.6	20.1	0.4	0.022
2 wt%	26.3	19.1	13.6	8.4	27.7	4.8	91.9	8.1	36.2	45.0	18.2	0.7	0.037
3 wt%	32.1	14.9	12.9	8.2	31.8	0.1	94.9	5.1	36.9	45.5	16.5	1.1	0.063

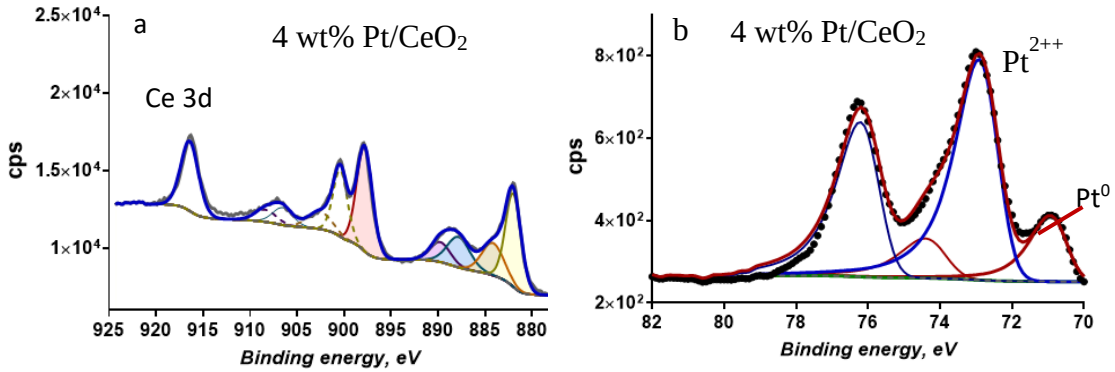

Figure II.2 *XPS analysis of the 4 wt% and Pt/CeO_2 sample showing the (a) Ce 3d region and (b) the Pt 4f region shows that the Pt is in the Pt(II) oxidation state with a 20% contribution from Pt(0).*

Table II.2. Analysis of Ce and Pt peaks in the XPS spectrum of the air-treated catalysts containing 4 wt% Pt. The sample now contains a well-defined peak of metallic Pt, consistent with the XRD and SEM results showing the presence of large Pt particles in the sample.

	Binding Energy (eV) CeO_2					Pt (0)	Pt (II)	Surface concentration & Pt/Ce ratio				
Sample	882.4	884.4	888.4	890.8	898.3	70.6	72.8	C 1s%	O 1s%	Ce 3d%	Pt 4f%	Pt/Ce
*4 wt%	30.7	14.6	14.0	7.3	33.3	20.6	79.4	46.5	38.6	14.1	0.89	0.066

*This sample contains metallic Pt in the form of large particles and atomically dispersed Pt

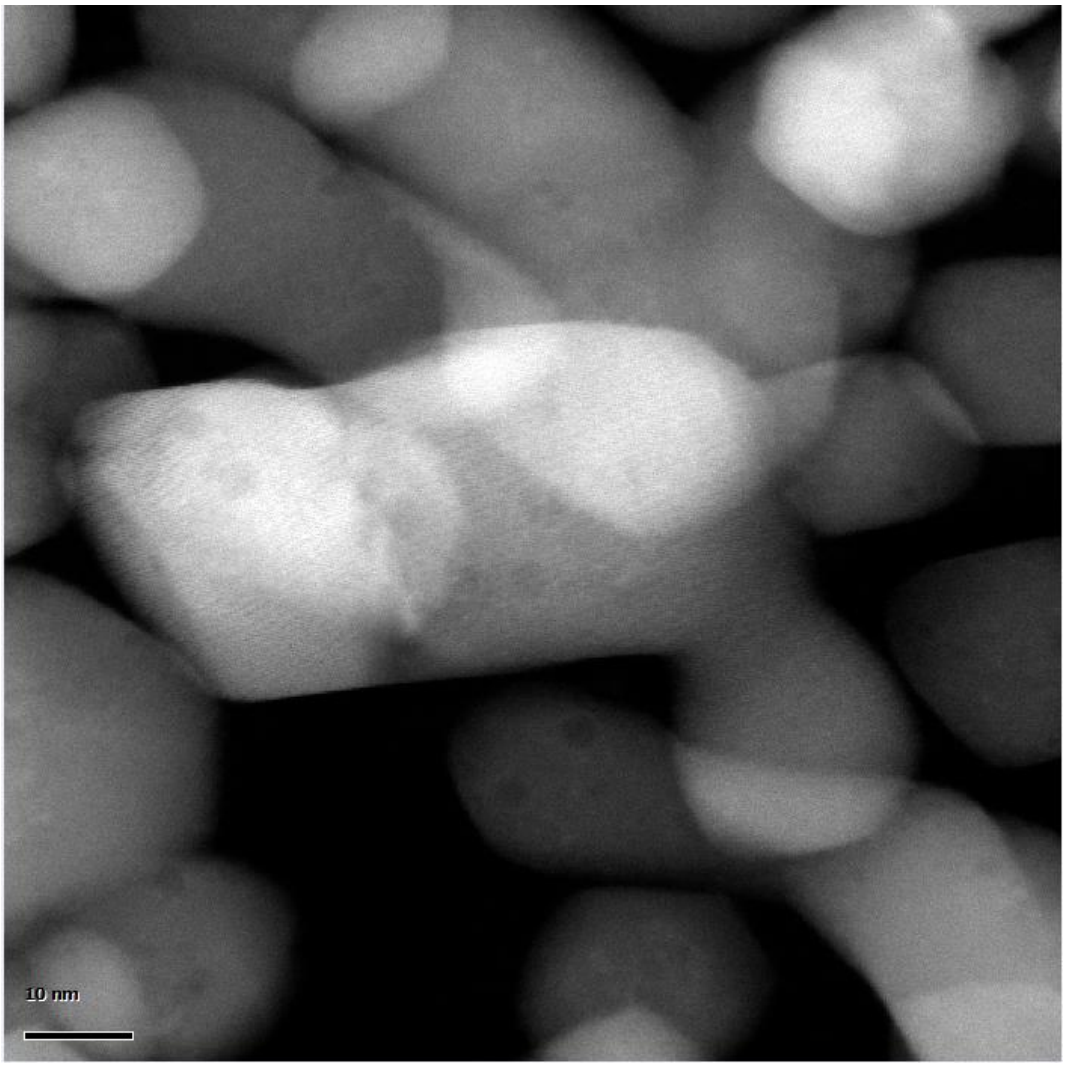

Figure II.3 *HAADF-STEM image of the 4 wt% Pt/CeO_2 sample, showing a typical region which does not contain Pt particles. The ceria (111) lattice fringes of 0.31 nm confirm that the STEM resolution is adequate to image clusters of this size. However, no clusters were seen via STEM HAADF images using this JEOL 2010F microscope. EDS analysis of such regions (as shown in Figure S4b) reveals that Pt is present, though not visible, with an average concentration of 3.2 wt% Pt. The atomically dispersed Pt can only be imaged via Aberration Corrected STEM imaging as shown in Figure 2 in the main text.*

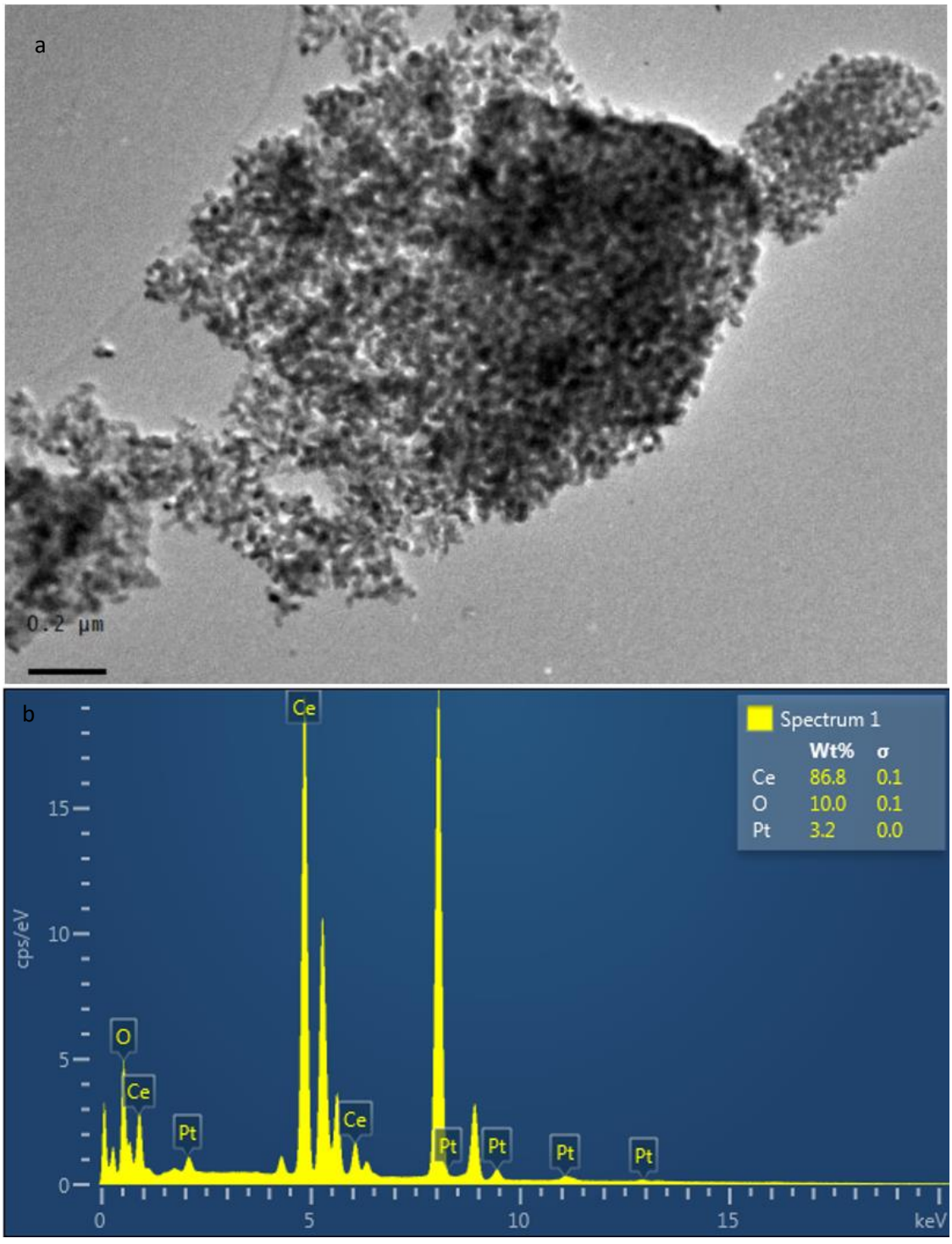

Figure II.4. *(a) Low magnification TEM image of the sample obtained in the JEOL 2010F microscope. EDS analysis (b) was done in regions where no Pt particles were seen in TEM images.*

Table II.3. Results of XRD whole pattern fitting using the program JADE from MDI Quantitative, Size and Strain Analysis

Phase ID	Wt%	(esd)	Vol%	(esd)	RIR	Density	Crystallite size (Å)	Strain
Cerianite (Ce) CeO_2	99.2	(0.3)	99.7	(0.5)	15.28	7.2251	81	0.0
Platinum (Pt)	0.8	(0.1)	0.3	(0.0)	25.52	21.5107	697	0.0

XRF (wt%): CeO_2=99.2%

Density of Specimen= 7.2653 (g/cm^3), Absorption (μ) of specimen= 2092.1(1/cm)

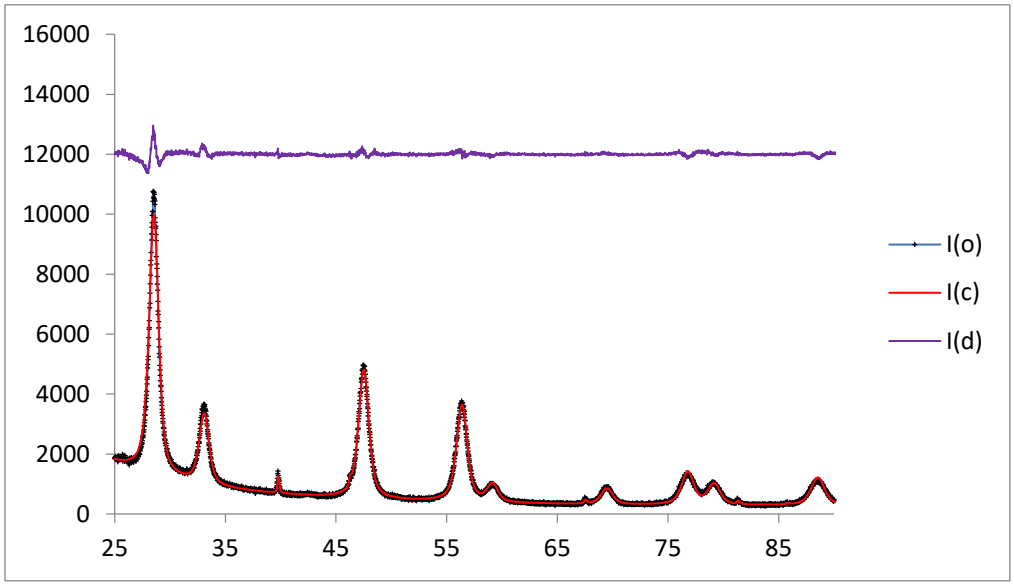

Figure II.5. *XRD pattern, indicating how the peak fitting was done to determine the wt% of crystalline Pt which was detected via XRD, I(o)=data from XRD, I(c)=data calculated by Jade, I(d)= I(o)-I(c).*

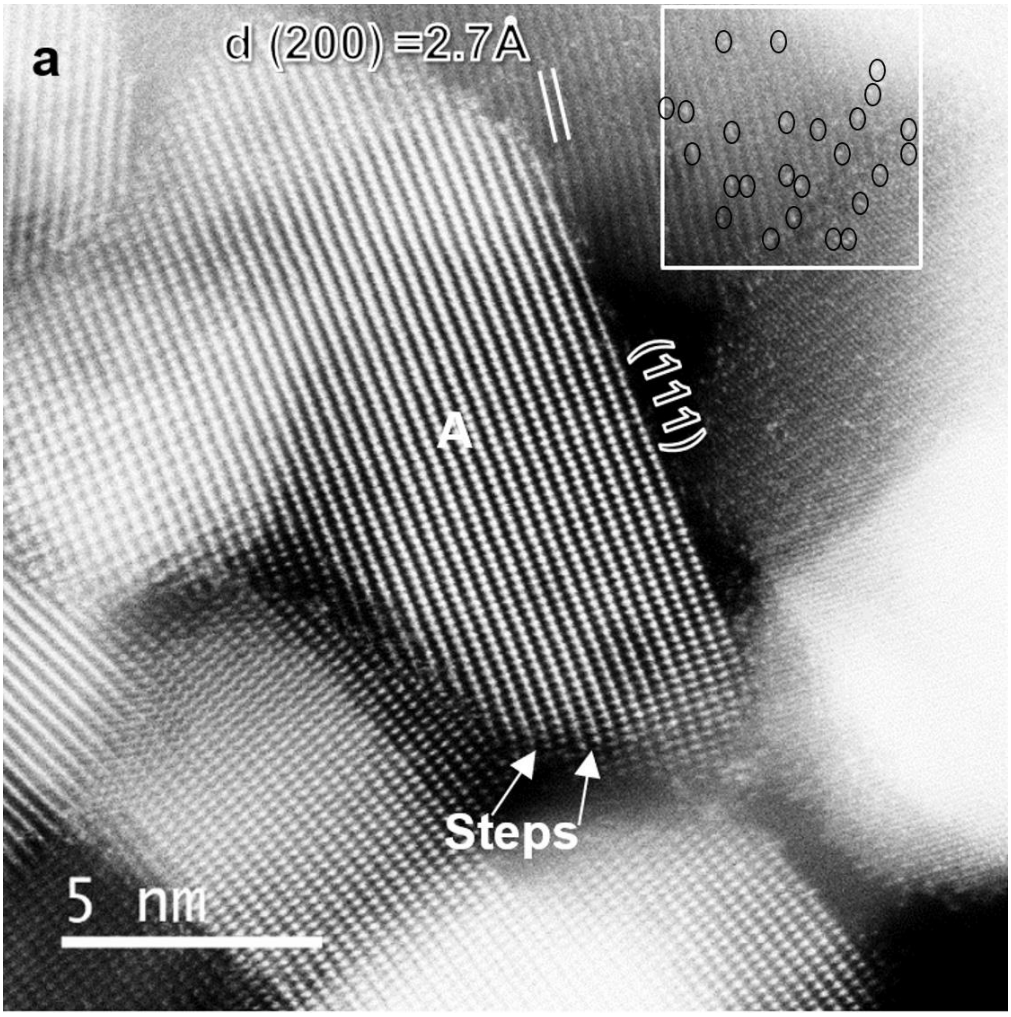

Figure II.6. *Quantification of the surface concentration of Pt atoms in the image shown in Figure 4.3c. The boxed region is 5 nm square and contains 25 atoms of Pt, which corresponds to 1 atom of Pt/nm^2 which is consistent with the results of LEIS (Table 4.2).*

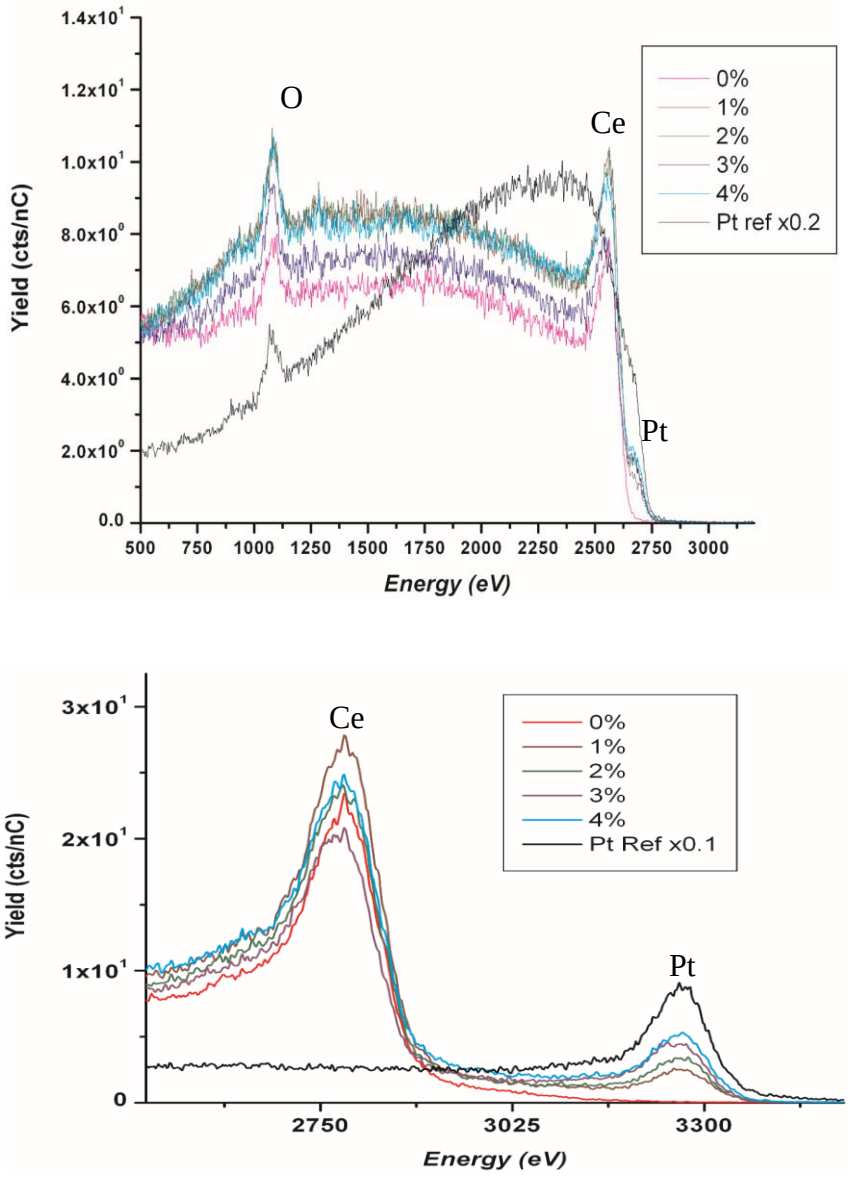

Figure II.7. *(a) 3 keV $^{4}He^{+}$ LEIS spectra for the samples and sputter cleaned Pt reference (scaled down), all after O atom treatment. The spectrum shows an overlap between the Pt and Ce peaks, making quantification difficult and (b) 5 keV $^{20}Ne^{+}$ LEIS spectra for the samples after O atom treatment, compared to a sputter cleaned Pt foil scaled down). With 5 keV $^{20}Ne^{+}$ as a primary ion, the resolution at higher mass improves and the Pt can be quantified without any overlap.*

Table II.3. Estimation of surface concentration of the Pt reference foil via LEIS

	Molecular Mass (g/mol)	Density (ρ) (g/cm^3)	Volume (nm^3/mol)	Area (nm^2/mol)	PtO_2 atom/nm^2
PtO_2	227.08	10.2	37.0E-02	11.1E-01	9.01
Pt	195.08	21.5	1.51E-02	6.10E-02	16.04

Volume (nm^3/mol)= $\{(Mass/\rho)*10^{21}/6.023*10^{23}\}=1.660*10^{-3}*M/\rho$

Area (nm^2/mol) = $(Volume/mol)^{2/3}$

Table II.4. Calculation of the surface concentration of Pt by LEIS

Nominal Loading (wt%) Pt	Spt (cst/nc)	Pt atoms/nm^2 by LEIS
1	167	0.37
2	244	0.54
3	350	0.77
4	386	0.85
Pt Oxidized	6820	9.01

*Formula used to calculate the number of atoms per square nanometer by LEIS:

Pt atoms/nm^2 = Spt*9.01/(Rsup*6820)

Rsup=Roughness factor of the support=0.6

This roughness factor of 0.6 was determined for alumina and this value has also been successfully used for ceria and zirconia supports.

Appendix III: Supporting Data for Chapter 6

Materials and Methods

Diffuse reflectance infrared Fourier transform spectroscopy (DRIFTS) measurements were performed on an IR spectrometer Tensor 27 from Bruker, coupled with a Praying Mantis Diffuse Reflection accessory from Harrick. A thermostat GSD 320 T quadrupole mass spectrometer from Pfeiffer Vacuum with a Secondary Electron Multiplier was connected to monitor the outlet flow composition. The spectra and backgrounds taken had a resolution of 4 cm^{-1} and 128 scans were averaged for each spectrum and background. The detailed DRIFTS experimental procedures can be found in our previous work. Briefly, the catalyst was pretreated at 300 °C for 0.5 h under 10% O_2/He (40 sccm) and purged with helium for 0.5 h (40 sccm) at the same temperature. The temperature was then decreased to 125 °C and a background spectrum was taken. 1%CO and 10% O_2 balanced with He was introduced into the cell at a flow rate of 40 sccm for 30 min. Afterward, the flow of CO was discontinued and O_2 or He was kept flowing for 10 min while the spectra were recorded.

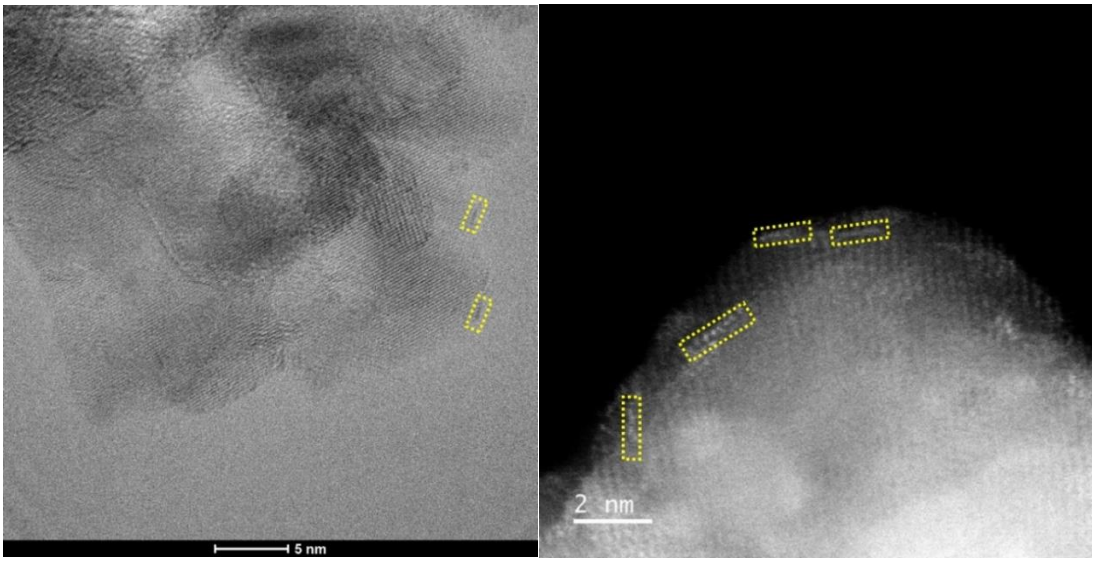

Figure III.1 *AC-TEM and STEM images of 2 wt.%Pt+1wt.%Pt@CeO_2 catalyst (2Pt/1Pt@CeO_2 calcined at 500 °C) showing the formation of Pt 2-D rafts labeled by boxes. a, AC-TEM image of the 2 wt.%Pt+1wt.%Pt@CeO_2 catalyst (2Pt/1Pt@CeO_2 calcined at 500 °C) showing the presence of Pt 2-D rafts. b, AC-STEM image of 2 wt.%Pt+1wt.%Pt@CeO_2 catalyst showing the presence of Pt 2-D rafts.*

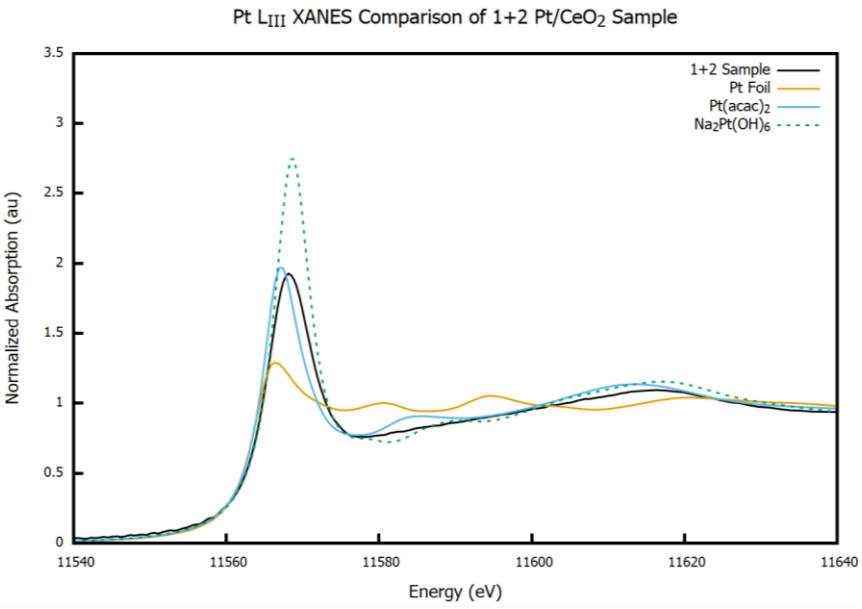

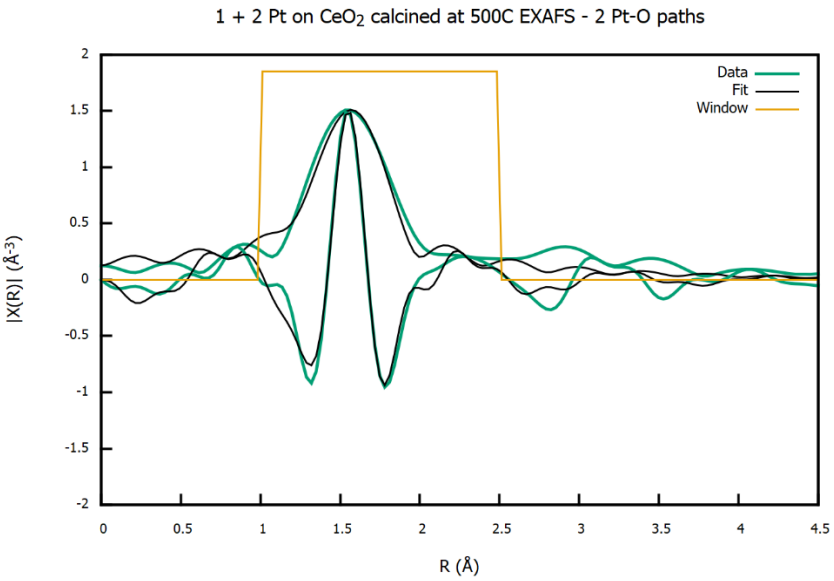

Figure III.2 *XANES and EXAFS data for the 2 wt.%Pt+1wt.%Pt@CeO_2 catalyst (2Pt/1Pt@CeO_2 calcined at 500 ^oC).*

Table III.1 XANES and EXAFS data for the 2 wt.%Pt + 1wt.%Pt@CeO_2 (2Pt/1Pt@CeO_2 calcined at 500 ^oC)

EXAFS and XANES						
Sample	XANES Energy (keV)	Scatter	N	R, Å	$\Delta\sigma^2$ (x 10^3)	Eo, eV
References						
Pt Foil	11.5640	Pt-Pt	12	2.78	0	-0.2
$Na_2Pt(OH)_6$	11.5666	Pt-O	6	2.05	0	-0.3
$Pt(AcAc)_2$	11.5652	Pt-O	4	2.03	0	-0.3
Pt L_3 Edge						
2 wt.%Pt + 1wt.%Pt@CeO_2	11.5656	Pt-O	4.8	1.98	0.003	-

Table III.2. Surface Concentration of Pt Determined by LEIS

	Molecular (g/mol)	Mass	Density (ρ) (g/cm^3)	Volume (nm^3/mol)	Area (nm^2/mol)	PtO_2 atom/nm^2
PtO_2	227.08		10.2	37.0E-02	11.1E-01	9.01
Pt	195.08		21.5	1.51E-02	6.10E-02	16.04
Sample			Spt (cst/nc)		Pt atoms/nm^2 by LEIS	
Pt oxidized			2858		9.01	
1wt.%Pt/CeO_2			104		0.55	
2 wt.%Pt+1wt.%Pt/CeO_2			419		2.2	

Volume (nm^3 /mol) = {(Mass/ ρ) * 10^{21}/6.023 * 10^{23}}

=1.660 * 10^{-3} * M/ρ

Area (nm^2/mol) = (Volume/mol)$^{2/3}$

*Formula used to calculate the number of atoms per square nanometer by LEIS:

Pt atoms/nm^2 = Spt*9.01/(Rsup*2858)

Rsup=Roughness factor of the support=0.6

This roughness factor of 0.6 was determined for alumina and this value has also been successfully used for ceria and zirconia supports.

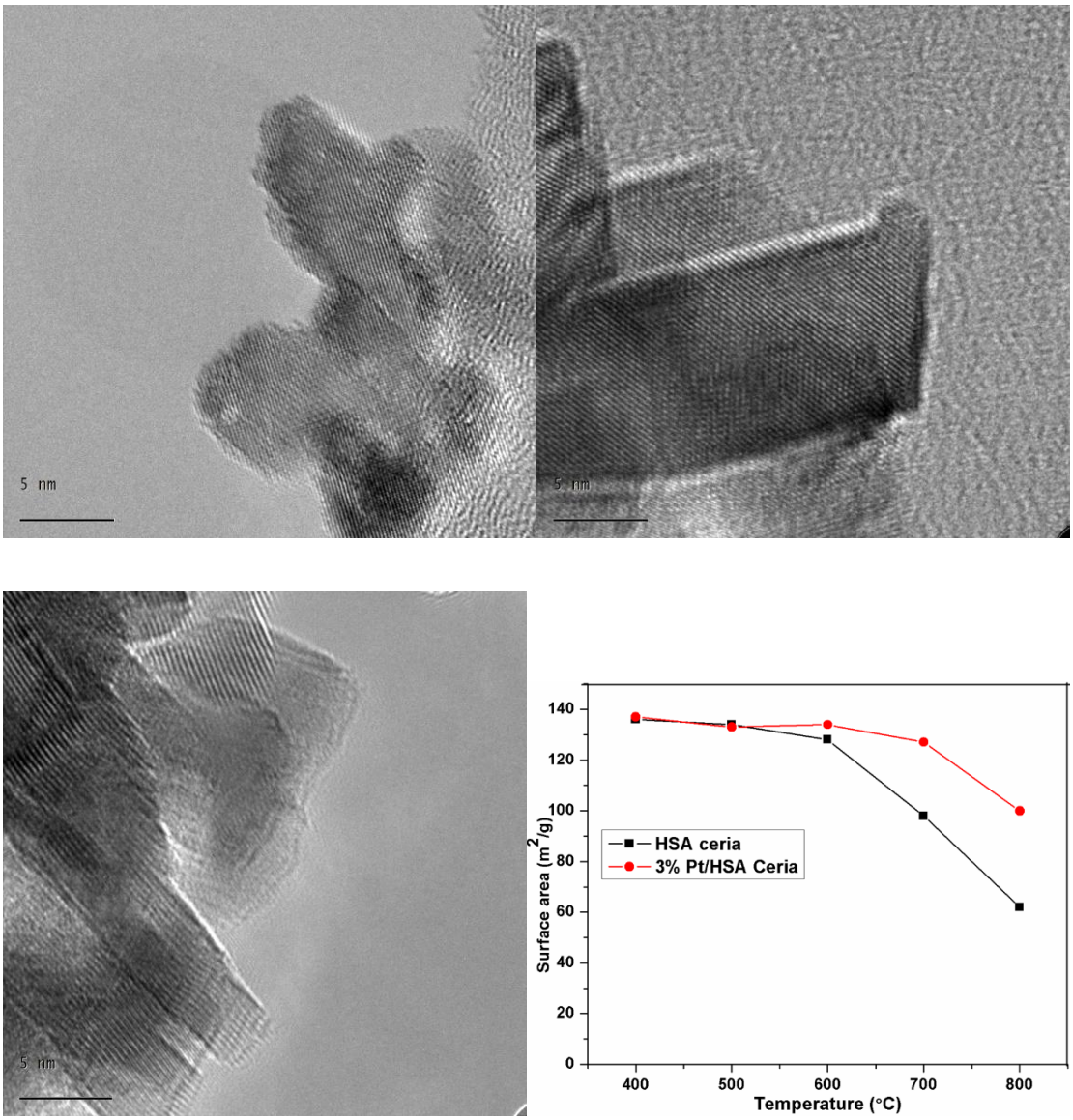

Figure III.3 ***HRTEM images of ceria and surface area of ceria and Pt/CeO₂. a,*** *HRTEM image of as-received ceria showing surface roughness.* ***b,c,*** *HRTEM image of ceria went to 800 ˚C treatment shows highly faceted planes.* ***d,*** *Surface areas of ceria and Pt/CeO₂ as a function of aging temperature.*

Figure III.4 is XRD patterns and SEM images of 2wt% Pt deposited on atom trapped 1wt% Pt@CeO_2 (2Pt/1Pt@CeO_2). No Pt (111) peak is observed in XRD for 500˚C treated catalyst showing in Appendix III Figure III.4a. The SEM images of 2Pt/1Pt@CeO_2

calcined at 600 ^{o}C suggest that Pt grows in 2D fashion encircled with a yellow dotted line (Supplementary Figure 4b and 4c). When this catalyst is subjected to high-temperature treatment (> 600 ^{o}C), Pt grows in one direction to form a rod as shown in Supplementary Figure 4d. This is consistent with Fig. 1 because Pt grows in ceria (111) epitaxially in the form of a 2D structure. The 800˚C treatment of 2wt% Pt on 1wt% Pt atom trapped on ceria shows in XRD the preferred orientation of Pt (111) peak and the absence of Pt (200) peak. This suggests that Pt grows epitaxially on ceria (111) and that leads to the formation of the preferred orientation of Pt.

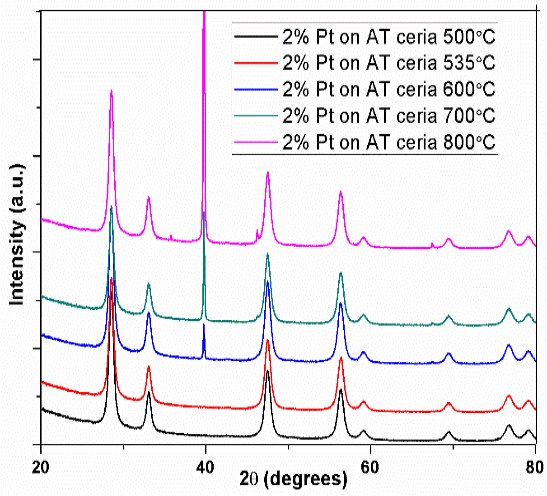

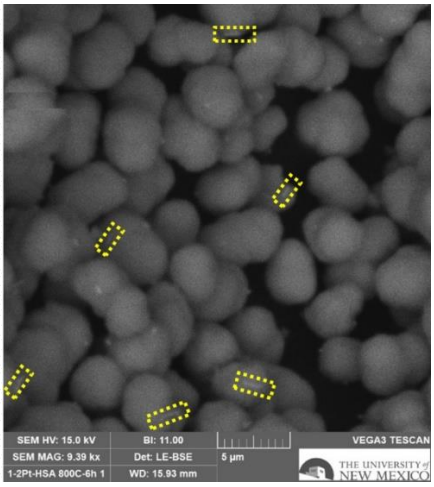

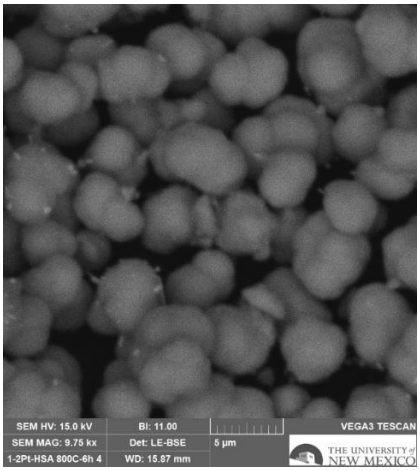

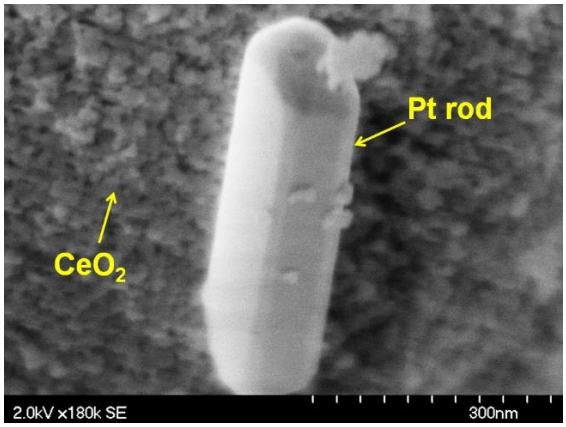

Figure III.4 *XRD patterns and TEM images of 2 wt.%Pt+1 wt.%Pt/CeO_2 catalyst (2Pt/1Pt@CeO_2) with different calcination temperatures. a, The XRD patterns of the 2wt%Pt+1wt%Pt/ceria catalyst calcined at different temperatures (500-800 °C) showing the preferred orientation of Pt (111) on 2Pt/1Pt@CeO_2 after the calcination is higher than 600 °C. b,c, SEM images of 2wt%Pt+1wt%Pt/ceria calcined at 600 °C showing the formation of Pt nanofibers (indicated by dotted rectangles). d, SEM image of 2Pt/1Pt@CeO_2 calcined at 800 °C showing the formation of the orientated Pt rod.*

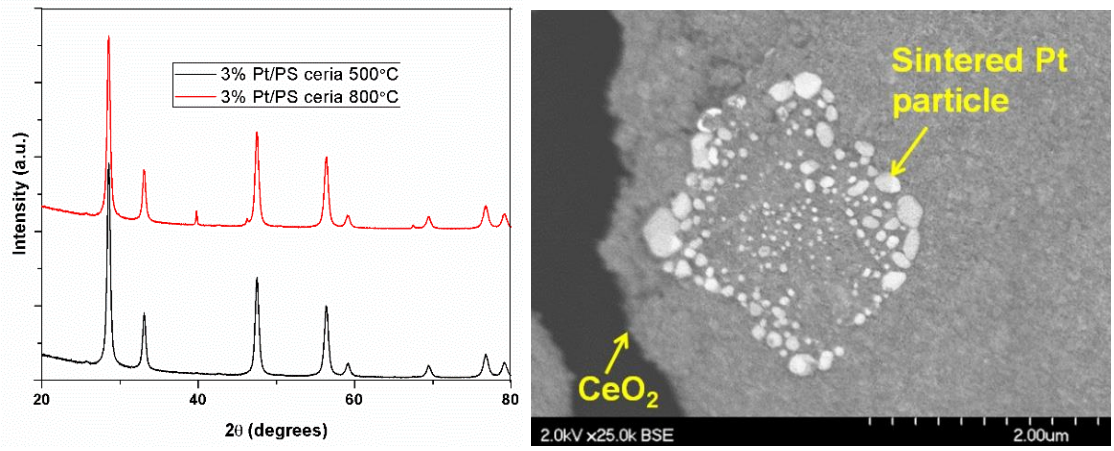

Figure III.5 ***Large Pt particles with randomly orientation form on pre-sintered ceria. a,*** *XRD pattern of 3 wt% Pt on pre-sintered ceria calcined at different temperatures.* ***b,*** *SEM image of a 3 wt% Pt on pre-sintered ceria showing the formation of randomly oriented Pt particles indicating that pre-sintered ceria does not trap Pt atoms.*

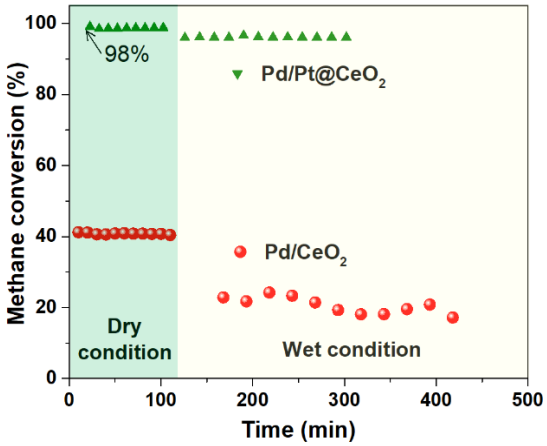

Figure III.6 *Methane oxidation reactivity measurements for Pd/Pt@CeO₂ and Pd/CeO₂ before and after reduction in wet and dry conditions. The effect of water vapor on the reactivity of Pd/Pt@CeO₂ and Pd/CeO₂ catalysts in methane oxidation at 380 °C was performed in a separate reactor (2% CH₄, 5% O₂ and He as balance).*

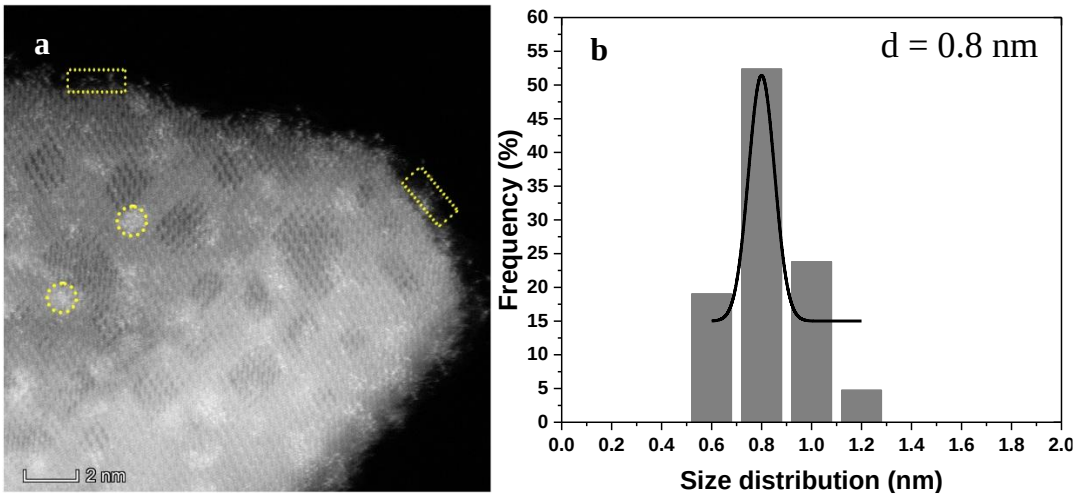

Figure III.7 ***STEM image of the as-synthesized Pd/Pt@CeO₂ catalyst prepared by depositing Pd on atom trapping Pt@CeO₂. a,*** *AC-STEM image of Pd/Pt@CeO₂ catalyst showing the formation of Pd oxide rafts.* ***b,*** *the Size distribution of Pd oxide on Pd/Pt@CeO₂ catalyst*

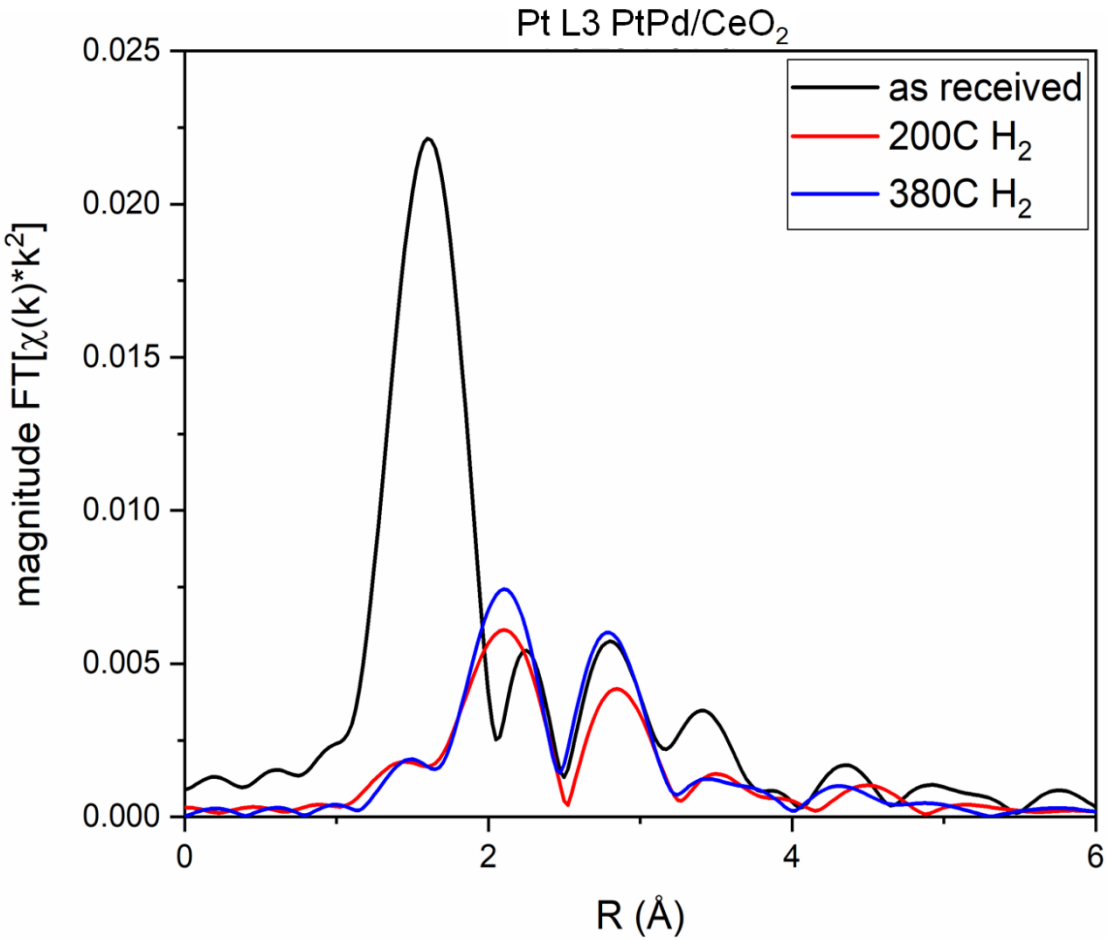

Figure III.8 *EXAFS spectra of the Pt L-edge of PtPd/CeO_2 catalyst before and after in-situ reduction in H_2. It shows that the ionic Pt species in PtPd/CeO_2 catalyst was completely reduced after H_2 treatments.*

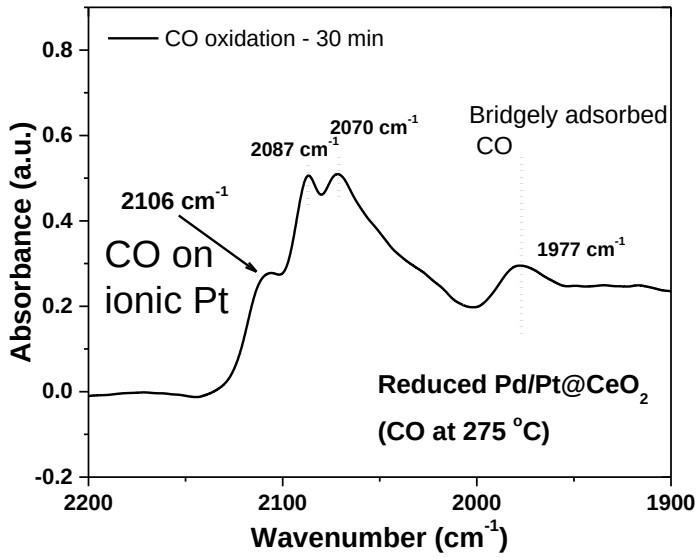

Figure III.9 *CO-DRIFTS spectra of Pd/Pt@CeO_2 catalyst after reduction in CO at 275 °C showing the stronger CO absorption on ionic Pt. The peak at 2106 cm^{-1} is assigned to the CO adsorbed on single Pt sites. The bands at 2087 cm^{-1} and 2070 cm^{-1} are assigned to the CO adsorbed on Pd nanoclusters.*

8.0 REFERENCES

1. Jones, J.; Xiong, H.; DeLaRiva, A.T.; Peterson, E.J.; Pham, H.; Challa, S.R.; Qi, G.; Oh, S.; Wiebenga, M.H.; Hernández, X.I.P.; Wang, Y.; Datye, A.K. Thermally stable single-atom platinum-on-ceria catalysts via atom trapping. *Science*. **353**, 150–154 (2016).

2. USDRIVE, Aftertreatment protocols for catalyst test characterization and performance: evaluation low-temperature oxidation catalyst test protocol 2015, (2015) https://cleers.org/wp-content/uploads/2015_LTAT-Oxidation-Catalyst-Characterization-protocol.pdf.

3. Alcock, C.B.; Hooper, G.W. Thermodynamics of the gaseous oxide of the platinum-group metals. *Proc. R. Soc. A Math. Phys. Eng. Sci.* **254**, 551–561 (1959).

4. Harris, P.J.F.; Boyes, E.D.; Cairns, J.A. The sintering of an alumina-supported platinum catalyst studied by transmission electron microscopy. *J. Catal.* **82**, 127–146 (1983).

5. Carrillo, C.; DeLaRiva, A.; Xiong, H.; Peterson, E.J.; Spilde, M.N.; Kunwar, D.; Goeke, R.S.; Wiebenga, M.; Oh, S.H.; Qi, G.; Challa, S.R.; Datye, A.K. Regenerative trapping: How Pd improves the durability of Pt diesel oxidation catalysts. *Appl. Catal. B Environ.* **218**, 581–590 (2017).

6. Nagai, Y.; Hirabayashi, T.; Dohmae, K.; Takagi, N.; Minami, T.; Shinjoh, H.; Matsumoto, S. Sintering inhibition mechanism of platinum supported on ceria-based oxide and Pt-oxide-support interaction. *J. Catal.* **242**, 103–109 (2006).

7. Hansen, T. W.; Delariva, A. T.; Challa, S. R.; Datye, A. K. Sintering of nanoparticles: particle migration or Ostwald ripening? *Acc. Chem. Res.* **46**, 1720–1730 (2014).

8. Graham, G.W.; Jen, H.W.; Ezekoye, O.; Kudla, R.J.; Chun, W.; Pan, X.Q.; McCabe, R.W. Effect of alloy composition on dispersion stability and catalytic activity for NO oxidation over alumina-supported Pt-Pd catalysts. *Catal. Letters* **116**, 1–8 (2007).

9. Wynblatt, P. Particle Growth in model supported metal catalysis-II. Comparison of experiment with theory. *Acta Metall.* **24**, 1175–1182 (1976).

10. Xiong, H.; Peterson, E.; Qi, G.; Datye, A.K. Trapping mobile Pt species by PdO in diesel oxidation catalysts: Smaller is better. *Catal. Today* **272**, 80–86 (2016).

11. Mamontov, E.; Egami, T.; Brezny, R.; Koranne, M.; Tyagi, S. Lattice defects and oxygen storage capacity of nanocrystalline ceria and ceria-zirconia. *J. Phys. Chem. B* **104**, 11110–11116 (2000).

12. Li, W.Z.; Kovarik, L.; Mei, D.; Liu, J.; Wang, Y.; Peden, C.H.F. Stable platinum nanoparticles on specific $MgAl_2O_4$ spinel facets at high temperatures in oxidizing atmospheres. *Nat. Commun.* **4**, 1–8 (2013).

13. Wang, H.; Dong, J.; Allard, L.F.; Lee, S.; Oh, S.; Wang, J.; Li, W. Single-site Pt / La-Al_2O_3 stabilized by barium as an active and stable catalyst in purifying CO and C_3H_6 emissions. *Appl. Catal. B Environ.* **244**, 327–339 (2019).

14. Porsgaard, A.X.S.; Merte, L.R. Ono, L.K.; Behafarid, F.; Matos, J.; Helveg, S.; Salmeron, M.; Cuenya, B.R.; Besenbacher, F. Stability of platinum nanoparticles photoelectron spectroscopy study.*ACS Nano.* **6,** 10743–10749 (2012).

15. Fryburg, G.C.; Petrus, H.M. Kinetics of the oxidation of platinum. *J. Electro. Chem. Soc.* 496–503 (1961)

16. Kunwar, D.; Zhou, S.; De La Riva, A.; Peterson, E.; Xiong, H.; Pereira Hernandez, X.I.; Purdy, S.C.; Veen, R. T.; Brongersma, H.H.; Miller, J.T.; Hashiguchi, H.; Kovarik, L.; Lin, S.; Guo, H.; Wang, Y.; Datye, A. Stabilizing high metal loadings of thermally stable platinum single atoms on an industrial catalyst support. *ACS Catal.* 9, 3978−3990 (2019).

17. Dvořák, F.; Camellone, M.F.; Tovt, A.; Tran, N.; Negreiros, F.R.; Vorokhta, M.; Skála, T.; Matolínová, I.; Mysliveček, J.; Matolín, V.; Fabris, S. Creating single-atom Pt-ceria catalysts by surface step decoration. *Nat. Commun.* **7**, 1–8 (2016).

18. Leistner, K.; Gonzalez, C.; Kumar, A.; Kamasamudram, K.; Olsson, L.

Volatilisation and subsequent deposition of platinum oxides from diesel oxidation catalysts. *Appl. Catal. B Environ.* **241**, 338–350 (2019).

19. Pereira-Hernández, X.I.; DeLaRiva, A.; Muravev, V.; Kunwar, D.; Xiong, H.; Sudduth, B.; Engelhard, M.; Kovarik, L.; Hensen, E.J.M.; Wang, Y.; Datye, A.K. Tuning Pt-CeO_2 interactions by high-temperature vapor-phase synthesis for improved reducibility of lattice oxygen. *Nat. Commun.* **10**, 1358 (2019).
20. Plessow, P.N.; Abild-Pedersen, F. Sintering of Pt nanoparticles via volatile PtO_2: Simulation and comparison with experiments. *ACS Catal.* **6**, 7098–7108 (2016).
21. Wang, X.; Bokhoven, J.A.V.; Palagin, D. Ostwald ripening versus single-atom trapping: Towards understanding platinum particle sintering. *Phys. Chem. Chem. Phys.* **19**, 30513–30519 (2017).
22. Simonsen, S.B.; Chorkendorff, I.; Dahl, S.; Skoglundh, M. Direct observations of oxygen-induced platinum nanoparticle ripening studied by in-situ TEM. *J. Am. Chem. Soc.* 7968–7975 (2010).
23. Benavidez, A.D.; Kovarik, L.; Genc, A.; Agrawal, N.; Larsson, E.M.; Hansen, T.W.; Karim, A.M.; Datye, A.K. Environmental transmission electron microscopy study of the origins of anomalous particle size distributions in supported metal catalysts. *ACS Catal.* **2**, 2349–2356 (2012).
24. Wynblatt, P.; Gjostein, N.A. Particle growth in model supported metal catalysis-I. Theory. *Acta Metall.* 1165–1174 (1976).
25. Gänzler, A.; Casapu, M.; Maurer, F.; Störmer, H.; Gerthsen, D.; Ferré, G.; Vernoux, P.; Bornmann, B.; Frahm, R.; Murzin, V.; Nachtegaal, M.; Votsmeier, M.; Grunwaldt, J.-D. Tuning the Pt/CeO_2-Interface by In Situ Variation of the Pt Particle

Size. *ACS Catal.* **8**, 4800–4811 (2018).

26. Yang, X. F.; Wang, A.; Qiao, B.; Li, J.; Liu, J.; Zhang, T. Single-atom catalysts: A new frontier in heterogeneous catalysis. *Acc. Chem. Res.* **46**, 1740–1748 (2013).

27. Qiao, B.; Wang, A.; Yang, X.; Allard, L. F.; Jiang, Z.; Cui, Y.; Liu, J.; Li, J.; Zhang, T. Single-atom catalysis of CO oxidation using Pt1/FeOx. *Nat. Chem.* **3**, 634–641 (2011).

28. DeRita, L.; Dai, S.; Lopez-Zepeda, K.; Pham, N.; Graham, G. W.; Pan, X.; Christopher, P. Catalyst architecture for stable single-atom dispersion enables site-specific spectroscopic and reactivity measurements of CO adsorbed to Pt atoms, oxidized Pt clusters, and metallic Pt clusters on TiO_2. *J. Am. Chem. Soc.* **139**, 14150–14165 (2017).

29. Lin, J.; Wang, A.; Qiao, B.; Liu, X.; Yang, X.; Wang, X.; Liang, J.; Li, J.; Liu, J.; Zhang, T. Remarkable performance of Ir1/FeOx single-atom catalyst in water gas shift reaction. *J. Am. Chem. Soc.* **135**, 15314–15317 (2013).

30. Duarte, R. B.; Krumeich, F.; Van Bokhoven, J. A. Structure, activity, and stability of atomically dispersed Rh in methane steam reforming. *ACS Catal.* **4**, 1279–1286 (2014).

31. Han, C. W.; Iddir, H.; Uzun, A.; Curtiss, L. A.; Browning, N. D.; Gates, B. C.; Ortalan, V Migration of single iridium atoms and tri-iridium clusters on MgO surfaces: Aberration-corrected STEM imaging and Ab initio calculations. *J. Phys. Chem. Lett.* **6**, 4675–4679 (2015).

32. Liu, J. Catalysis by supported single metal atoms. *ACS Catal.* **7**, 34–59 (2017).

33. Liu, L.; Corma, A. Metal catalysts for heterogeneous catalysis: From single atoms

to nanoclusters and nanoparticles. *Chem. Rev.* **118**, 4981–5079 (2018).

34. Li, Z.; Wang, D.; Wu, Y.; Li, Y. Recent advances in the precise control of isolated single-site catalysts by chemical methods. *Natl. Sci. Rev.* 1–37 (2018).

35. Li, H.; Wang, L.; Dai, Y.; Pu, Z.; Lao, Z.; Chen, Y.; Wang, M.; Zheng, X.; Zhu, Y.; Zhang, W.; Si, R.; Ma, C.; Zeng, J. Synergetic interaction between platinum monomers in CO_2 hydrogenation. *Nat. Nanotechnol.* **13**, 411-417 (2018).

36. Wu, X.; Zhang, H.; Dong, J.; Qiu, M.; Kong, J.; Zhang, Y.; Li, Y.; Xu, G.; Zhang, J.; Ye, J. Surface step decoration of isolated atom as electron pumping : Atomic-level insights into visible-light hydrogen evolution. *Nano Energy* **45**, 109–117 (2018).

37. Xiong, H.; Lin, S.; Goetze, J.; Pletcher, P.; Guo, H.; Kovarik, L.; Artyushkova, K.; Weckhuysen, B. M.; Datye, A. K. Thermally stable and regenerable platinum–tin clusters for propane dehydrogenation prepared by atom trapping on ceria. *Angew. Chemie - Int. Ed.* **56**, 8986–8991 (2017).

38. Datye, A.; Wang, Y. Atom trapping: a novel approach to generate thermally stable and regenerable single-atom catalysts. *Natl. Sci. Rev.* **5**, (2018).

39. Bruix, A.; Lykhach, Y.; Matolínová, I.; Neitzel, A.; Skála, T.; Tsud, N.; Vorokhta, M.; Stetsovych, V.; Ševčíková, K.; Mysliveček, J.; Fiala, R.; Václavu, M.; Prince, K. C.; Bruyère, S.; Potin, V.; Illas, F.; Matolín, V.; Libuda, J.; Neyman, K. M. Maximum noble-metal efficiency in catalytic materials: Atomically dispersed surface platinum. *Angew. Chemie - Int. Ed.* **53**, 10525–10530 (2014).

40. Paier, J.; Penschke, C.; Sauer, J. Oxygen defects and surface chemistry of ceria: Quantum chemical studies compared to experiment. *Chem. Rev.* **113**, 3949–3985

(2013).

41. Santhanam, N.; Conforti, T. A.; Spieker, W.; Regalbuto, J. R. Nature of metal catalyst precursors adsorbed onto oxide supports. *Catal. Today* **21**, 141–156 (1994).

42. Farmer, J. A.; Campbell, C. T. Ceria maintains smaller metal catalyst particles by strong metal-support bonding. *Science* **329**, 933–936 (2010).

43. Brongersma, H. Low-energy ion scattering in characterization of materials. *J. Wiley Sons* 2024–2044 (2012).

44. Ressler, T. WinXAS: a program for X-ray absorption spectroscopy data analysis under MS-Windows. *J. Synchrotron Radiation* **5**, 118–122 (1998).

45. Kresse, G.; Furthmüller, J. Efficient iterative schemes for ab initio total energy calculations using a plane-wave basis Set. *Phys. Rev. B - Condens. Matter Mater. Phys.* **54**, 11169–11186 (1996).

46. Kresse, G.; Furthmüller, J. Efficiency of ab-initio total energy calculations for metals and semiconductors using a plane-wave basis Set. *Comput. Mater. Sci.* **6**, 15–50 (1996).

47. Perdew, J. P.; Chevary, J. A.; Vosko, S. H.; Jackson, K. A.; Pederson, M. R.; Singh, D. J.; Fiolhais, C. Atoms, molecules, solids, and surfaces: Applications of the generalized gradient approximation for exchange and correlation. *Phys. Rev. B* **46**, 6671–6687 (1992).

48. Blöchl, P. E. Projector Augmented-wave method. *Phys. Rev. B* **50**, 17953–17979 (1994).

49. McFarland, E. W.; Metiu, H. Catalysis by doped oxides. *Chem. Rev.* **113**, 4391–4427 (2013).

50. Branda, M. M.; Hernández, N. C.; Sanz, J. F.; Illas, F. Density functional theory study of the interaction of Cu, Ag, and Au atoms with the regular CeO_2 (111) Surface. *J. Phys. Chem. C* **114**, 1934–1941 (2010).

51. Gerward, L.; Staun Olsen, J.; Petit, L.; Vaitheeswaran, G.; Kanchana, V.; Svane, A. Bulk modulus of CeO_2 and PrO_2- An experimental and theoretical study. *J. Alloys Compd.* **400**, 56–61 (2005).

52. Liu, J. C.; Wang, Y. G.; Li, J. Toward rational design of oxide-supported single-atom catalysts: Atomic dispersion of gold on ceria. *J. Am. Chem. Soc.* **139**, 6190–6199 (2017).

53. Avakyan, L. A.; Kolpacheva, N. A.; Paramonova, E. V.; Singh, J.; Hartfelder, U.; van Bokhoven, J. A.; Bugaev, L. A. Evolution of the atomic structure of ceria-supported platinum nanocatalysts: Formation of single layer platinum oxide and Pt–O–Ce and Pt–Ce linkages. *J. Phys. Chem. C* **120**, 28057–28066 (2016).

54. Thang, H. V.; Pacchioni, G.; DeRita, L.; Christopher, P. Nature of stable single atom Pt catalysts dispersed on anatase TiO_2. *J. Catal.* **367**, 104–114 (2018).

55. Kale, M. J.; Christopher, P. Utilizing quantitative in-situ FTIR spectroscopy to identify well-coordinated Pt atoms as the active site for CO oxidation on Al_2O_3 -supported Pt. *ACS Catal*. **6**, 5599-5609 (2016).

56. Aleksandrov, H. A.; Neyman, K. M.; Hadjiivanov, K. I.; Vayssilov, G. N. Can the state of platinum species be unambiguously determined by the stretching frequency of an adsorbed CO probe molecule ? *Phys. Chem. Chem. Phys.* **18**, 22108–22121 (2016).

57. Nie, L.; Mei, D.; Xiong, H.; Peng, B.; Ren, Z.; Hernandez, X. I. P.; DeLaRiva, A.;

Wang, M.; Engelhard, M. H.; Kovarik, L.; Datye, A. K.; Wang, Y. Activation of surface lattice oxygen in single-atom Pt/CeO_2 for low-temperature CO oxidation. *Science.* **358**, 1419–1423 (2017).

58. James, T. E.; Hemmingson, S. L.; Campbell, C. T. Energy of supported metal catalysts: from single atoms to large metal nanoparticles. *ACS Catal.* **5**, 5673–5678 (2015).

59. Sattler, J. J. H. B.; Ruiz-Martinez, J.; Santillan-Jimenez, E.; Weckhuysen, B. M. Catalytic dehydrogenation of light alkanes on metals and metal oxides. *Chem. Rev.* **114**, 10613–10653 (2014).

60. Kunwar, D.; Carrillo, C.; Xiong, H.; Peterson, P.; DeLaRiva, A.; Ghosh, A.; Qi, G.; Yang, M.; Weibenga, M.; Oh, S.; Li, W.; Datye, A.K. Investigating anomalous growth of platinum particles during accelerated aging of diesel oxidation catalysts. *Appl. Catal. B Environ.* **266**, 118598 (2020).

61. Liu, X.; Zhou, K.; Wang, L.; Wang, B.; Li, Y. Oxygen vacancy clusters promoting reducibility and activity of ceria nanorods. *J. Am. Chem. Soc.***131,** 3140–3141 (2009).

62. Aneggi, E.; Llorca, J.; Boaro, M.; Trovarelli, A. Surface-structure sensitivity of CO oxidation over polycrystalline ceria powders. *J.Catal*. **234**, 88–95 (2005).

63. Zhang, Z.; Zhu, Y.; Asakura, H.; Zhang, B.; Zhang, J.; Zhou, M.; Han, Y.; Tanaka, T.; Wang, A.; Zhang, T.; Yan, N. Thermally stable single atom $Pt/m\text{-}Al_2O_3$ for selective hydrogenation and CO oxidation. *Nat. Commun.* **8**, 16100 (2017).

64. Li, W.; Kovarik, L.; Mei, D.; Engelhard, M. H.; Gao, F.; Liu, J.; Wang, Y.; Peden, C. H. F. A General mechanism for stabilizing the small sizes of precious metal

nanoparticles on oxide supports. *Chem. Mater*. **26,** 5475-5481 (2014).

65. Luo, J.; Gao, F.; Karim, A.M.; Xu, P.; Browning, N. D.; Peden, C. H. F. Advantages of MgAlOx over γ - Al_2O_3 as a support material for potassium-based high-temperature lean NOx traps. *ACS Catal.* **5**, 4680−4689 (2015).

66. Kohn, W.; Sham, L.J. Self-consistent equations including exchange and correlation effects. *Phys. Rev.* **140**, A1133–A1138 (1965).

67. Perdew, J. P.; Burke, K.; Ernzerhof, M. Generalized gradient approximation made aimple. *Phys. Rev. Lett.* **77**, 3865–3868 (1996).

68. Köstlmeier, S.; Elsässer, C.; Meyer, B.; Finnis, M. W. Density functional study of interactions at the metal−ceramic interfaces Al/$MgAl_2O_4$ and Ag/$MgAl_2O_4$. *Phys. Status solidi A* **166**, 417−428 (1998).

69. Rasmussen, M.K.; Meinander, K.; Besenbacher, F.; Lauritsen, J. V. Noncontact atomic force microscopy imaging of atomic structure and cation defects of the polar $MgAl_2O_4$ (100) surface: Experiments and first-principles simulations. *Phys. Rev. B* **84**, (2011).

70. Liu, L.; Sun, Y.; Cheng, Z.; Zhu, J.; Yu, R. Subsurface reconstruction and saturation of surface bonds. *Sci. Bull.* **63**, 1570–1575 (2018).

71. Sickafus, K. E.; Wills, J. M.; Grimes, M. W. Structure of Spinel. *J. Am. Ceram. Soc.* **82**, 3279–3292 (1999).

72. Fang, C. M.; Parker, S. C.; de With G. Atomistic simulation of the surface energy of spinel $MgAl_2O_4$. *J. Am. Ceram. Soc.* **83**, 2082–2084 (2000).

73. Van der Laag, N.J.; Fang, C. M.; de With, G.; de Wijs.; G.A.; Brongersma, H. H. Geometry of {001} surfaces of spinel ($MgAl_2O_4$): First-principles simulations and

experimental measurements. *J. Am. Ceram. Soc.* **88**, 1544–1548 (2005).

74. Rasmussen, M.K.; Foster, A.S.; Hinnemann, B.; Canova, F.F.; Helveg, S.; Meinander, K.; Martin, N.M.; Knudsen, J.; Vlad, A.; Lundgren, E.; Stierle, A.; Besenbacher, F.; Lauritsen, J. V. Stable cation inversion at the $MgAl_2O_4$(100) surface. *Phys. Rev. Lett.* **107**, 036102 (2011).

75. Zhou, C.; Wu, J.; Kumar, T. J. D.; Balakrishnan, N.; Forrey, R. C.; Cheng, H. Growth pathway of Pt clusters on α-Al_2O_3 (0001) surface. *J. Phys. Chem. C* **111**, 13786–13793 (2007).

76. Munnik, P.; Jongh, P. E. De.; de Jong, K. P. Recent developments in the synthesis of supported catalysts. *Chem. Rev.* **115**, 6687-6718 (2015).

77. Wong, A.; Liu, Q.; Griffin, S.; Nicholls, A.; Regalbuto, J. R. Synthesis of ultrasmall, homogeneously alloyed, bimetallic nanoparticles on silica supports. *Science* **358,** 1427–1430 (2017).

78. Bradley, S. A.; Sinkler, W.; Voyles, P. M.; Allard, L. F. Behavior of Pt atoms on oxide supports during reduction treatments at elevated temperatures, characterized by aberration corrected stem imaging. *Catal. Lett.* **142,** 176–182 (2012).

79. Kwak, J. H.; Hu, J.; Mei, D.; Yi, C; Kim, D. H. Coordinatively unsaturated Al^{3+} centers as binding sites for active catalyst phases of platinum on g-Al_2O_3. *Science.* **325**, 1670–1673 (2009).

80. Bo, Z.; Sol, A.; Alexander, A.; Neil, S.; Christian, C.; Omar, F.; Justin, N. General synthesis and stabilization of small Pt nanoparticles on TiO_2 partially masked by SiO_2. *Appl. Catal. A*, **551**, 122–128 (2018).

81. Yao, S.; Zhang, X.; Zhou, W.; Gao, R.; Xu, W.; Ye, Y.; Lin, L. Atomic-layered Au

clusters on a -MoC as catalysts for the low-temperature water-gas shift reaction. *Science*. **393**, 389–393 (2017).

82. Chen, A.; Yu, X.; Miao, S.; Li, Y.; Kuld, S.; Sehested, J.; Liu, J.; Aoki, T.; Hong, S.; Camellone, M. F.; Fabris, S.; Ning, J.; Jin, C.; Yang, C.; Nefedov, A.; Wöll, C.; Wang, Y.; Shen, W. Structure of the catalytically active copper–ceria interfacial perimeter. *Nat. Catal.* **2**, 334–341 (2019).

83. Lu, J.; Elam, J. W.; Stair, P. C. Synthesis and stabilization of supported metal catalysts by atomic layer deposition. *Acc. Chem. Res.* **46**, 1806–1815 (2013).

84. Petrov, A. W.; Ferri, D.; Krumeich, F.; Nachtegaal, M.; Bokhoven J. A. van.; Kröcher, O. Stable complete methane oxidation over palladium based zeolite catalysts. *Nat. Commun.* 1-8, (2018)

85. Descormea, C.; Gclin, P.; Lccuyerb, C.; Primet, M. Palladium-exchanged Mm-type zeolites in the catalytic reduction of nitrogen monoxide by methane Influence of the Si /Al ratio on the activity and the hydrothermal stability. *Appl. Catal. B Environ.* **13**, 185–195 (1997).

86. Huang, W.; Goodman, E. D.; Losch, P.; Cargnello, M. Deconvoluting transient water effects on the activity of Pd methane combustion catalysts. *Ind. Eng. Chem. Res.* **57,** 10261-10268 (2018).

87. Zhang, F.; Hakanoglu, C.; Jr, J. A. H.; Weaver, J. F. Surface science inhibition of methane adsorption on PdO (101) by water and molecular oxygen. *Surf. Sci.* **617**, 249–255 (2013).

88. Xiong, H.; Wiebenga, M. H.; Carrillo, C.; Gaudet, J. R.; Pham, H.; Kunwar, D.; Oh. S. H.; Qi, G.; Kim, C. H.; Datye, A. K. Design considerations for low-temperature

hydrocarbon oxidation reactions on Pd based catalysts. *Appl. Catal. B Environ.* **236**, 436–444 (2018).

89. Lott, P.; Dolcet, P.; Casapu, M.; Grunwaldt, J.; Deutschmann, O. The effect of prereduction on the performance of Pd/Al_2O_3 and Pd/CeO_2 catalysts during methane oxidation. *Ind. Eng. Chem. Res.* **58**, 12561-12570 (2019).

90. Hellman, A.; Resta, A.; Martin, N. M.; Gustafson, J.; Trinchero, A.; Carlsson, P. A.; Balmes, O.; Felci, R.; van Rijn, R.; Frenken, J. W. M.; Andersen, J. N.; Lundgren, E.; Grönbeck, H. The active phase of palladium during methane oxidation. *J. Phys. Chem. Lett.* **3**, 678−682 (2012).

91. Martin, N. M.; Bossche, M, V. den.; Hellman, A.; Grönbeck, H.; Hakanoglu, C.; Gustafson, J.; Blomberg, S.; Johansson, N.; Liu, Z.; Axnanda, S.; Weaver, J. F.; Lundgren, E. Intrinsic ligand effect governing the catalytic activity of Pd oxide thin films. *ACS Catal.* **4**, 3330–3334 (2014).

92. Duan, H.; You, R.; Xu, S.; Li, Z.; Qian, K.; Cao, T.; Haung, W.; Bao, X. Pentacoordinated Al^{3+} stabilized active Pd structures on Al_2O_3 coated palladium catalysts for methane combustion. *Angew. Chemie Int. Ed.* **58**, 12043–12048 (2019).

93. Johns, T. R.; Gaudet, J. R.; Peterson, E. J.; Miller, J. T.; Stach, E. A.; Kim, C. H.; Balogh, M. P.; Datye, A. K. Microstructure of bimetallic Pt-Pd catalysts under oxidizing conditions. *ChemCatChem* **5**, 2636–2645 (2013).

94. Yashnik, S. A.; Chesalov, Y. A.; Ishchenko, A. V.; Kaichev, V. V.; Ismagilov, Z. R. Effect of Pt addition on sulfur dioxide and water vapor tolerance of Pd-Mn-hexaaluminate catalysts for high-temperature oxidation of methane. *"Applied Catal. B, Environ.* **204**, 89–106 (2017).

95. Wei, S.; Li, A.; Liu, J. C.; Chen, W.; Gong, Yue.; Zhang, Q.; Cheong, W. C.; Wang, Y.; Zheng, L.; Xiao, H.; Chen, C.; Wang, D.; Peng, Q.; Gu, L.; Han, X.; Li, J.; Li, Y. Direct observation of noble metal nanoparticles transforming to thermally stable single atoms. *Nat. Nanotechnol.* **13**, 856–861 (2018).

96. Goodman, E. D.; Johnston-Peck, A. C.; Dietze, E. M.; Wrasman, C. J.; Hoffman, A. S.; Pedersen, F. A.; Bare, S. R.; Plessow, P. N.; Cargnello, M. Catalyst deactivation via decomposition into single atoms and the role of metal loading. *Nat. Catal.* **2**, 748–755 (2019).

97. Wang, H.; Liu, J. X.; Allard, L. F.; Lee, S.; Liu, J.; Li, H.; Wang, J.; Wang, J.; Oh, S. H.; Li, W.; Stephanopoulos, M. F.; Shen, M.; Goldsmith, B. R.; Yang, M. Surpassing the single-atom catalytic activity limit through paired Pt-O-Pt ensemble built from isolated Pt1 atoms. *Nat. Commun.* 1–12 (2019).

98. Xiong, H.; Lester, K.; Ressler, T.; Schlögl, R.; Allard, L. F.; Datye, A. K. Metastable Pd ↔ PdO Structures During High Temperature Methane Oxidation. *Catal. Lett.* **147**, 1095–1103 (2017).